EUROPEAN ORGANIZATION FOR NUCLEAR RESEARCH (CERN)

FERMILAB-PUB-13-626-CMS

CERN-PH-EP/2013-168
2013/12/17

CMS-SMP-13-003

Measurement of the differential and double-differential Drell–Yan cross sections in proton-proton collisions at $\sqrt{s} = 7\,\text{TeV}$

The CMS Collaboration*

Abstract

Measurements of the differential and double-differential Drell–Yan cross sections are presented using an integrated luminosity of 4.5 (4.8) fb^{-1} in the dimuon (dielectron) channel of proton-proton collision data recorded with the CMS detector at the LHC at $\sqrt{s} = 7\,\text{TeV}$. The measured inclusive cross section in the Z-peak region (60–120 GeV) is $\sigma(\ell\ell) = 986.4 \pm 0.6\,(\text{stat.}) \pm 5.9\,(\text{exp. syst.}) \pm 21.7\,(\text{th. syst.}) \pm 21.7\,(\text{lum.})\,\text{pb}$ for the combination of the dimuon and dielectron channels. Differential cross sections $\text{d}\sigma/\text{d}m$ for the dimuon, dielectron, and combined channels are measured in the mass range 15 to 1500 GeV and corrected to the full phase space. Results are also presented for the measurement of the double-differential cross section $\text{d}^2\sigma/\text{d}m\,\text{d}|y|$ in the dimuon channel over the mass range 20 to 1500 GeV and absolute dimuon rapidity from 0 to 2.4. These measurements are compared to the predictions of perturbative QCD calculations at next-to-leading and next-to-next-to-leading orders using various sets of parton distribution functions.

Published in the Journal of High Energy Physics as doi:10.1007/JHEP12(2013)030.

*See Appendix A for the list of collaboration members

Contents

1 Introduction

The Drell–Yan (DY) lepton pair production in hadron-hadron collisions is described in the standard model by s-channel γ^*/Z exchange. Theoretical calculations of the differential cross section $\mathrm{d}\sigma/\mathrm{d}m$ and the double-differential cross section $\mathrm{d}^2\sigma/\mathrm{d}m\,\mathrm{d}|y|$, where m is the dilepton invariant mass and $|y|$ is the absolute value of the dilepton rapidity, are well established up to next-to-next-to-leading order (NNLO) in quantum chromodynamics (QCD) [1–4]. The rapidity distributions of the gauge bosons γ^*/Z are sensitive to the parton content of the proton, and the very high energy of the Large Hadron Collider (LHC) allows the parton distribution functions (PDFs) to be probed in a wide region of Bjorken x and Q^2: $0.0003 < x < 0.5$ and $500 < Q^2 < 90000\,\mathrm{GeV}^2$ in the double-differential cross section measurement. The differential cross section $\mathrm{d}\sigma/\mathrm{d}m$ is measured in an even higher Q^2 region up to $1.2 \times 10^6\,\mathrm{GeV}^2$. The large center of mass energy at the LHC allows a substantial extension of the range of Bjorken x and Q^2 covered compared to previous experiments [5–10].

The rapidity y and the invariant mass m of the dilepton system produced in proton-proton collisions are related at leading order (LO) to the momentum fraction x_+ (x_-) carried by the parton in the forward-going (backward-going) proton as described by the formula $x_\pm = (m/\sqrt{s})e^{\pm y}$, where the forward direction is defined as the positive z direction of the CMS detector coordinate system. Therefore, the rapidity and mass distributions are sensitive to the PDFs of the interacting partons. Since the y distribution is symmetric around zero in proton-proton collisions, we consider only the differential cross section in $|y|$ in order to reduce the statistical errors. The measurements of the double-differential cross section $\mathrm{d}^2\sigma/\mathrm{d}m\,\mathrm{d}|y|$ in DY production are particularly important since they provide quantitative tests of perturbative QCD and help to constrain the quark and antiquark flavor content of the proton. Precise experimental measurements of these cross sections also allow comparisons to different PDF sets and the underlying theoretical models and calculations [11]. In addition, measuring DY lepton-pair production is important for other LHC physics analyses because it is a major source of background for various interesting processes, such as $\mathrm{t\bar{t}}$ and diboson production, as well as for searches for new physics beyond the standard model, such as the production of high-mass dilepton resonances.

The existing PDFs are derived from fixed-target and collider measurements of deep inelastic scattering (DIS), neutrino-nucleon scattering, inclusive jet production, and vector boson production from H1 and ZEUS [5], SLAC [6], FNAL E665, E772, E866 [7, 8], and the CDF and D0 [9, 10] experiments. These experiments covered the following ranges of dilepton invariant mass and Bjorken scale parameter x: $m \leq 20\,\mathrm{GeV}$ and $x > 0.01$. Previous DY measurements from the fixed-target experiments contributed substantially to the understanding of the quark and antiquark distributions in the proton. Collider vector boson production data contribute to constraining the d/u ratio at high x and the valence quark distributions. These data are also important in reducing the theoretical uncertainties in the determination of the W-boson mass at hadron colliders [12]. The current status of the PDFs and the importance of the LHC measurements are reviewed in Ref. [13, 14], and the DY differential cross section has been measured by CMS, LHCb, and ATLAS [15–17].

This paper presents measurements of the DY differential cross section $\mathrm{d}\sigma/\mathrm{d}m$ in the dimuon and dielectron channels in the mass range $15 < m < 1500\,\mathrm{GeV}$ and the double-differential cross section $\mathrm{d}^2\sigma/\mathrm{d}m\,\mathrm{d}|y|$ in the dimuon channel for the mass range $20 < m < 1500\,\mathrm{GeV}$. These measurements are performed with the Compact Muon Solenoid (CMS) detector at the LHC using proton-proton collision data at $\sqrt{s} = 7\,\mathrm{TeV}$. The differential cross section measurements are normalized to the Z-peak region (60–120 GeV). This normalization cancels out the effect

of multiple interactions per bunch crossing (pileup) on the reconstruction, and the uncertainty in the integrated luminosity, acceptance, and efficiency evaluation. The measurements in this paper are corrected for the effects of resolution, which cause event migration between bins in mass and rapidity. The observed dilepton invariant mass is also corrected for final-state photon radiation (FSR). This effect is most pronounced below the Z peak. The differential cross sections are measured separately for both lepton flavors within the detector acceptance and are extrapolated to the full phase space. The consistency of the muon and electron channels enables them to be combined and compared with the NNLO QCD predictions calculated with FEWZ [18] using the CT10 PDF set. The $\mathrm{d}^2\sigma/\mathrm{d}m\,\mathrm{d}|y|$ measurement is compared to the FEWZ next-to-leading-order (NLO) prediction calculated with CT10 PDFs and the NNLO theoretical predictions as computed with FEWZ using the CT10, NNPDF2.1, MSTW2008, HERAPDF15, JR09, ABKM09, and CT10W PDFs [19–25].

2 CMS detector

A right-handed coordinate system is used in CMS, with the origin at the nominal collision point, the x axis pointing to the center of the LHC ring, the y axis pointing up (perpendicular to the LHC plane), and the z axis along the counterclockwise-beam direction. The azimuthal angle ϕ is the angle relative to the positive x axis measured in the x-y plane. The central feature of the CMS detector is a superconducting solenoid providing an axial magnetic field of 3.8 T and enclosing an all-silicon inner tracker, a crystal electromagnetic calorimeter (ECAL), and a brass/scintillator hadron calorimeter. The tracker is composed of a pixel detector and a silicon strip tracker, which are used to measure charged-particle trajectories covering the full azimuthal angle and pseudorapidity interval $|\eta| < 2.5$. The pseudorapidity η is defined as $\eta = -\ln[\tan(\theta/2)]$, where $\cos\theta = p_z/p$. Muons are detected in the pseudorapidity range $|\eta| < 2.4$ with four stations of muon chambers. These muon stations are installed outside the solenoid and sandwiched between steel layers, which serve both as hadron absorbers and as a return yoke for the magnetic field flux. They are made using three technologies: drift tubes (DT), cathode strip chambers (CSC), and resistive-plate chambers. The muons associated with the tracks measured in the silicon tracker have a transverse momentum (p_T) resolution of about 1–6% in the muon p_T range relevant for the analysis presented in this paper. Electrons are detected using the energy deposition in the ECAL, which consists of nearly 76 000 lead tungstate crystals that are distributed in the barrel region ($|\eta| < 1.479$) and two endcap regions ($1.479 < |\eta| < 3$). The ECAL has an ultimate energy resolution better than 0.5% for unconverted photons with transverse energies (E_T) above 100 GeV. The electron energy resolution is better than 3% for the range of energies relevant for the measurement reported in this paper. A detailed description of the CMS detector can be found elsewhere [26]. The CMS experiment uses a two-level trigger system. The level-1 (L1) trigger, composed of custom processing hardware, selects events of interest using information from the calorimeters and muon detectors [27]. The high-level trigger (HLT) is software-based and further decreases the event collection rate by using the full event information, including that from the tracker [28].

3 Data and Monte Carlo samples

The measurements reported in this paper are based on pp collision data recorded in 2011 with the CMS detector at the LHC at $\sqrt{s} = 7$ TeV, corresponding to integrated luminosities of $4.5\,\mathrm{fb}^{-1}$ (dimuon channel) and $4.8\,\mathrm{fb}^{-1}$ (dielectron channel).

Monte Carlo (MC) samples are used in the analysis for determining efficiencies, acceptances,

and backgrounds from processes that result in two leptons, and for the determination of systematic uncertainties. Methods based on control samples in data are used to determine efficiency correction factors and backgrounds. The MC samples are produced with a variety of generators, as discussed below. The samples are processed with the full CMS detector simulation software based on GEANT4 [29], which includes trigger simulation and the full chain of CMS event reconstruction.

The DY signal samples are generated with the NLO generator POWHEG [30] interfaced with the PYTHIA v6.4.24 [31] parton shower generator (a combination referred to as POWHEG). Both $\mathrm{t\bar{t}}$ and single-top-quark samples are produced with the POWHEG generator, and the τ-lepton decays are simulated with the TAUOLA package [32]. The $\mathrm{t\bar{t}}$ sample is rescaled to the NLO cross section of 157 pb. Diboson samples (WW/WZ/ZZ) and QCD multijet background events are produced with PYTHIA. An inclusive single-W-boson sample (W+jets) is produced using POWHEG. The proton structure is defined using the CT10 [19] parton distribution functions. All samples are generated using the PYTHIA Z2 tune [33] to model the underlying event. Pileup effects are taken into account in the MC samples, which are generated with the inclusion of multiple proton-proton interactions that have timing and multiplicity distributions similar to those observed in data (average of 9 interactions per bunch crossing).

The POWHEG MC sample is based on NLO calculations and a correction is added to take NNLO effects into account. The NNLO effects alter the cross section as a function of the dilepton kinematic variables and are important in the low-mass region and in normalizing the cross section. The dilepton correction is determined from the ratio between the double-differential cross sections (binned in rapidity y and transverse momentum p_{T}) calculated at NNLO with FEWZ [18] and at NLO with POWHEG. The effect of the correction factors on the acceptance is up to 40% in the low-mass region and is almost negligible in the high-mass region. This correction factor ω is applied on an event-by-event basis. For a given mass range it is defined in bins of dilepton rapidity y and dilepton transverse momentum p_{T}:

$$\omega(p_{\mathrm{T}}, y) = \frac{(\mathrm{d}^2\sigma/\mathrm{d}p_{\mathrm{T}}\,\mathrm{d}y)_{\mathrm{FEWZ}}}{(\mathrm{d}^2\sigma/\mathrm{d}p_{\mathrm{T}}\,\mathrm{d}y)_{\mathrm{POWHEG}}}. \quad (1)$$

The POWHEG MC events are then reweighted using ω as defined in Eq. (1). The reweighted POWHEG simulation is referred to as NNLO and is used for all the simulation-based estimations (acceptance, efficiency, FSR corrections) for both the dimuon and dielectron analyses. The differences between the NNLO reweighted POWHEG simulations and the FEWZ predictions, caused by unavoidable binning/statistics constraints, are used to extract modeling uncertainties. These modeling uncertainties are shown in the last column of Tables 1 and 2.

4 Cross section measurements

This analysis measures the DY dimuon and dielectron invariant mass spectra, $\mathrm{d}\sigma/\mathrm{d}m$, in the range 15 to 1500 GeV, and then corrects them for detector geometrical acceptance and kinematic requirements to obtain the spectra corresponding to the full phase space. The double-differential cross section $\mathrm{d}^2\sigma/\mathrm{d}m\,\mathrm{d}|y|$ is measured in the dimuon channel within the detector acceptance in the range of absolute dimuon rapidity from 0 to 2.4 and dimuon invariant mass from 20 to 1500 GeV. A $\mathrm{d}^2\sigma/\mathrm{d}m\,\mathrm{d}|y|$ analysis of the electron channel has not been performed.

The measured cross sections are calculated using the following formula:

$$\sigma = \frac{N_{\mathrm{u}}}{A \cdot \epsilon \cdot \rho \cdot L_{\mathrm{int}}}, \tag{2}$$

where N_{u} denotes the background-subtracted yield obtained using a matrix inversion unfolding technique to correct for the effects of the migration of events in mass due to the detector resolution. The acceptance A and the efficiency ϵ are both estimated from MC simulation, while ρ, the correction (scale) factor accounting for the differences in the efficiency between data and simulation, is extracted using a technique described in Section 4.4. Complete details of all corrections, background estimations, and the effects of the detector resolution and FSR are contained in later sections of this paper. The cross sections for these measurements are normalized to the Z-peak region ($60 < m < 120\,\mathrm{GeV}$) and thus the integrated luminosity L_{int} is only used for the Z-boson production cross section discussed in Section 5. The differential $\mathrm{d}\sigma/\mathrm{d}m$ cross section measurements are performed over a mass range from 15 to 1500 GeV in 40 variable-width mass bins chosen to provide reasonable statistical precision in each bin.

The double-differential cross section measurement is performed in dimuon rapidity space by choosing a bin size of 0.1–0.2 to reduce migration among the rapidity bins. The mass bins for the measurement of the double-differential cross section, $\mathrm{d}^2\sigma/\mathrm{d}m\,\mathrm{d}|y|$, are determined on the basis of optimization of physics background subtraction, and also the number of events per bin. The low-mass region (20–60 GeV), where QCD processes contribute the most and the FSR effects are significant, is divided into three bins. The Z-peak region (60–120 GeV) is a single bin, because in this region the DY production is dominated by Z-boson exchange, and this binning is convenient for both normalization and comparison with other measurements. The high-mass region (120–1500 GeV) is mapped onto two bins based on the number of events available. The binning is also chosen to make the systematic uncertainties comparable to the statistical uncertainties away from the Z-peak region. Six invariant mass bins are used, with bin edges 20, 30, 45, 60, 120, 200, and 1500 GeV. For each mass bin, 24 bins of width 0.1 in $|y|$ are defined, except for the highest mass bin, where only 12 absolute dimuon rapidity bins of width 0.2 are used.

4.1 Event selection

The experimental signature of DY production is two isolated and oppositely charged leptons originating from the same primary vertex. The analysis presented in this paper is based on the dilepton data samples selected by a variety of inclusive double-lepton triggers.

4.1.1 Muon selection

The first step in the muon selection is the trigger. The muon trigger thresholds depend on the instantaneous luminosity, and, since the instantaneous luminosity increased during 2011 data taking period, the trigger thresholds also increased. In the L1 trigger and HLT processing the data from the multiple detection layers of the CSC and DT muon chambers are analyzed to provide an estimate of the muon momentum. For data taken in the earlier part of the 2011 run, the trigger selects dimuon events where each muon has a transverse momentum of at least 6 GeV. For the subsequent running periods, the trigger selects events where one muon has $p_{\mathrm{T}} > 13\,\mathrm{GeV}$ and the other muon has $p_{\mathrm{T}} > 8\,\mathrm{GeV}$. The HLT then matches these candidate muon tracks to hits in the silicon tracker to form HLT muon candidates. In the offline analysis, data from the CSC and DT muon chambers are matched and fitted to data from the silicon tracker to form global muon candidates.

The muons are required to pass the standard CMS muon identification and quality control

criteria, which are based on the number of hits found in the tracker, the response of the muon chambers, and a set of matching criteria between the muon track parameters as measured by the CMS tracker and those measured in the muon chambers [34]. Both muons are required to match the HLT trigger objects. Cosmic-ray muons that traverse the CMS detector close to the interaction point can appear as back-to-back dimuons; these are removed by requiring both muons to have an impact parameter in the transverse plane of less than 2 mm with respect to the center of the interaction region. Further, the opening angle between the two muons is required to differ from π by more than 5 mrad. In order to reject muons from pion and kaon decays, a common vertex for the two muons is required. An event is rejected if the dimuon vertex probability is smaller than 2%. More details on muon reconstruction and identification can be found in Ref. [34].

To suppress the background contributions due to muons originating from heavy-quark decays and nonprompt muons from hadron decays, both muons are required to be isolated from other particles. The muon isolation criterion is based on the sum of the transverse momenta of the particles reconstructed with the CMS particle-flow algorithm [35] within a cone of size $\Delta R = 0.3$ centered on the muon direction, where $\Delta R = \sqrt{(\Delta\eta)^2 + (\Delta\phi)^2}$; photons and the muon candidate itself are excluded from the sum. The ratio of the summed transverse momenta to the transverse momentum of the muon candidate is required to be less than 0.2.

Each muon is required to be within the acceptance of the muon subsystem ($|\eta| < 2.4$). The leading muon in the event is required to have a transverse momentum $p_{\mathrm{T}} > 14\,\mathrm{GeV}$ and the trailing muon $p_{\mathrm{T}} > 9\,\mathrm{GeV}$, which allows us to operate on the plateau region of the trigger efficiency. Events are selected for further analysis if they contain opposite-charge muon pairs meeting the above requirements. If more than one dimuon candidate passes these selections, the pair with the highest χ^2 probability for a kinematic fit to the dimuon vertex is selected. No attempt has been made in this analysis to use the radiated photons detected in the ECAL to correct the muon energies for possible FSR. (Section 4.6 contains a discussion of FSR effects.)

4.1.2 Electron selection

Dielectron events are selected when triggered by two electrons with minimum E_{T} requirements of 17 GeV for one of the electrons and 8 GeV for the other. The triggers are the lowest threshold double-electron triggers in the 2011 data and allow one to probe the lowest possible dielectron mass. The selection of events at the trigger level, based on the isolation and the quality of an electron candidate, made it possible for the thresholds to remain unchanged throughout the full period of 2011 data taking in spite of the rapidly increasing luminosity.

The dielectron candidates are selected online by requiring two clusters in the ECAL, each with a transverse energy E_{T} exceeding a threshold value. The offline reconstruction of the electrons starts by building superclusters [36] in the ECAL in order to collect the energy radiated by bremsstrahlung in the tracker material. A specialized tracking algorithm is used to accommodate changes of the curvature caused by the bremsstrahlung. The superclusters are then matched to the electron tracks. The electron candidates are required to have a minimum E_{T} of 10 GeV after correction for the ECAL energy scale. In order to avoid the inhomogeneous response at the interfaces between the ECAL barrel and endcaps, the electrons are further required to be detected within the pseudorapidity ranges $|\eta| < 1.44$ or $1.57 < |\eta| < 2.5$.

The reconstruction of an electron is based on the CMS particle-flow algorithm [35]. The electrons are identified by means of shower shape variables while the electron isolation criterion is based on a variable that combines tracker and calorimeter information. For isolation, the transverse momenta of the particles within a cone of $\Delta R < 0.3$ are summed, excluding the

electron candidate itself. The ratio of the summed transverse momenta to the transverse momentum of the electron candidate is required to be less than 0.15 for all the electrons, except for those with $E_T < 20\,\text{GeV}$ in the endcaps, where the requirement is tightened to be less than 0.10. The isolation criteria are optimized to maximize the rejection of misidentified electrons from QCD multijet production and the nonisolated electrons from the semileptonic decays of heavy quarks. The electron candidates are required to be consistent with particles originating from the primary vertex in the event. Electrons originating from photon conversions are suppressed by requiring that there be no missing tracker hits before the first hit on the reconstructed track matched to the electron, and also by rejecting a candidate if it forms a pair with a nearby track that is consistent with a conversion. Additional details on electron reconstruction and identification can be found in Ref. [36].

Both electrons are selected with the impact parameter requirements $|d_{xy}| < 0.02\,\text{cm}$ and $|d_z| < 0.1\,\text{cm}$ with respect to the primary vertex. The leading electron candidate in an event is required to have a transverse momentum of $p_T > 20\,\text{GeV}$, while the trailing electron candidate must have $p_T > 10\,\text{GeV}$. As with muons, electrons are required to match HLT trigger objects, but no charge requirement is imposed on the electron pairs to avoid efficiency loss due to nonnegligible charge misidentification.

4.2 Background estimation

There are several physical and instrumental backgrounds that contribute to the sample of dilepton candidates. The main backgrounds in the region of high invariant masses (above the Z peak) are due to $\mathrm{t\bar{t}}$ and diboson production followed by leptonic decays, while the DY production of $\tau^+\tau^-$ pairs is the dominant source of background in the region just below the Z peak. At low values of the dimuon invariant mass (up to 40 GeV), most of the background events are due to QCD events with multiple jets (QCD multijet). The situation is slightly different for electrons in the final state. At low values of dielectron invariant mass most of the background events are from $\tau^+\tau^-$ and $\mathrm{t\bar{t}}$ processes, whereas the contribution from the QCD multijet process is small due to the stricter selection for electrons compared to muons.

A combination of techniques is used to determine contributions from various background processes. Wherever feasible, the background rates are estimated from data, reducing the uncertainties related to simulation of these sources. The remaining contributions are evaluated using simulation. The background estimation is performed by following the same methods for both the $\mathrm{d}\sigma/\mathrm{d}m$ and $\mathrm{d}^2\sigma/\mathrm{d}m\,\mathrm{d}|y|$ measurements.

4.2.1 Dimuon background estimation

In the dimuon channel, the QCD multijet background is evaluated using control data samples. This method makes use of the muon isolation and the sign of the charge as two independent discriminating variables to identify a signal region and three background regions in the two-dimensional space defined by the muon charge sign and the isolation. The background estimation is then based on the ratio between the number of signal and background events in the above regions [37].

The $\mathrm{t\bar{t}}$ background, which is the dominant process at high masses, is estimated from data using a sample of events with $\mathrm{e}\mu$ pairs. The estimated number of $\mu^+\mu^-$ events can be expressed as a function of observed $\mathrm{e}^\pm\mu^\mp$ events based on acceptance and efficiencies determined from simulation. The electron and muon candidates in the $\mathrm{e}\mu$ sample are required to satisfy the DY $\to \mathrm{e}^+\mathrm{e}^-$ and DY $\to \mu^+\mu^-$ selection criteria, respectively. The electron candidates are required to have $E_T > 20\,\text{GeV}$, the muon candidates $p_T > 15\,\text{GeV}$, and both candidates are

required to be within the range $|\eta| < 2.4$. They are further required to pass the lepton quality criteria. The number of expected $\mu^+\mu^-$ events is calculated bin by bin as a function of the dilepton mass. Deviations from the MC simulation are used for assessing the systematic uncertainties. All other backgrounds are estimated using MC simulation, although an estimation of all non-QCD multijet backgrounds has been performed with the eμ method of data analysis as a cross-check.

The expected shapes and relative dimuon yields from data and MC events in bins of invariant mass can be seen in Fig. 1. As shown in the figure, the QCD multijet process is the dominant background in the low-mass region, contributing up to about 10% in the dimuon rapidity distribution. In the high-mass regions, $t\bar{t}$ and single-top-quark (tW) production processes are dominant and collectively contribute up to about 20%. The expected shapes and relative dimuon yields from data and MC events in bins of dimuon rapidity, per invariant mass bin, can be seen in Fig. 2.

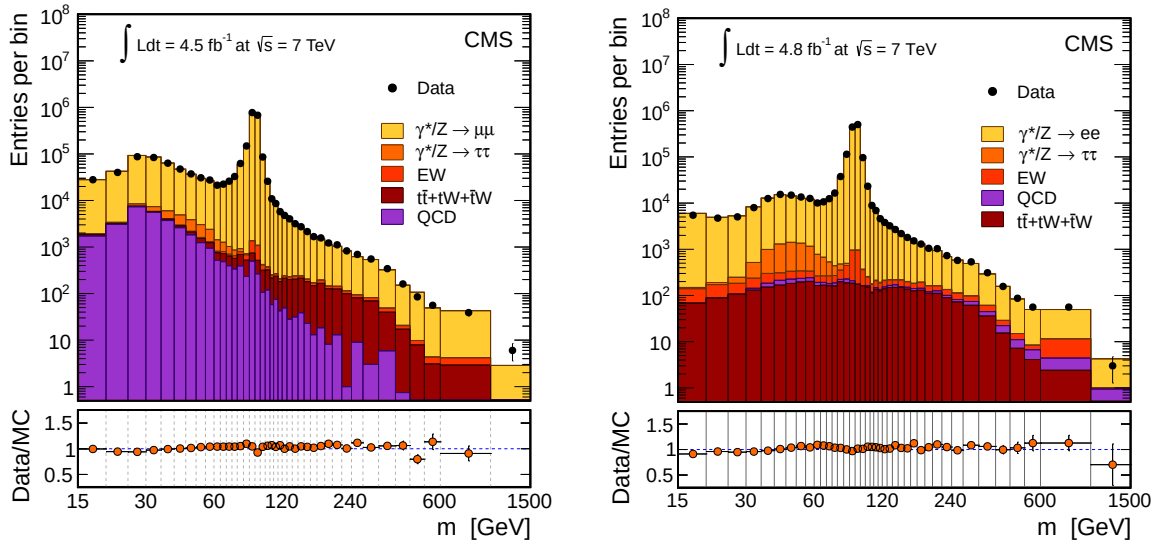

Figure 1: The observed dimuon (left) and dielectron (right) invariant mass spectra for data and MC events and the corresponding ratios of observed to expected yields. The QCD multijet and $t\bar{t}$ background yields in the muon channel and the QCD multijet contribution in the electron channel are predicted using control samples in data. The EW histogram indicates the diboson and W+jets production. The NNLO reweighted POWHEG MC signal sample is used. No other corrections are applied. Error bars are statistical only.

4.2.2 Dielectron background estimation

In the dielectron channel, the background processes do contain genuine leptons in most cases. The background can be divided into two categories: (1) both electrons are genuine, and (2) one or both electrons are due to misidentification.

The genuine electron background is estimated from data using the eμ method described above. The dominant electroweak (EW) background from low invariant mass up to the Z peak is DY $\to \tau^+\tau^-$. Above the Z peak the background contributions from $t\bar{t}$ and diboson production become significant, with relatively smaller contributions from the tW process. All of these processes produce $e^\pm\mu^\mp$ final states at twice the rate of e^+e^- or $\mu^+\mu^-$. Consequently, the backgrounds from these modes can be measured from a sample of $e^\pm\mu^\mp$ after accounting for the differences in the acceptance and efficiency. The contributions from DY $\to \tau\tau$, $t\bar{t}$, tW, and the

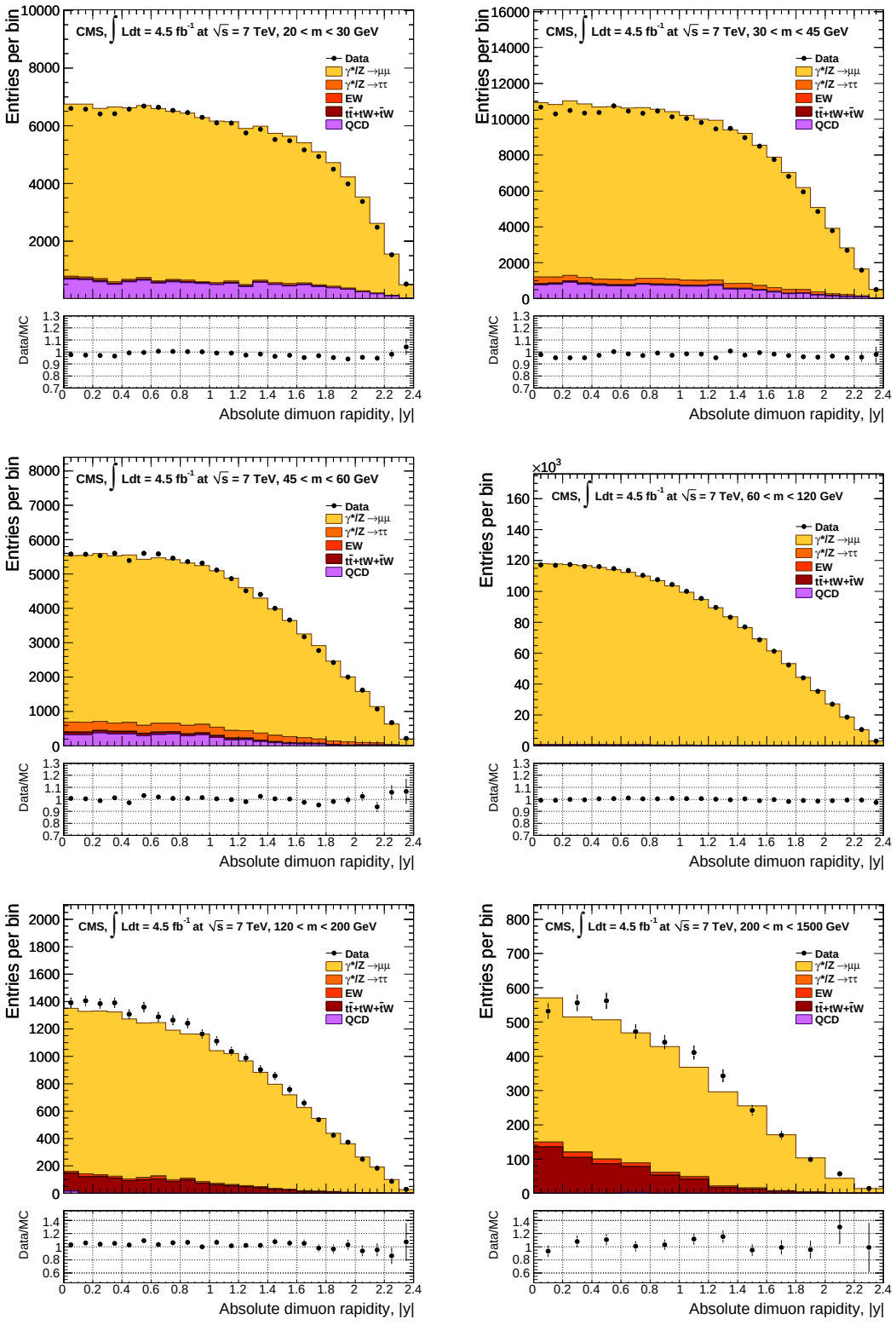

Figure 2: The observed dimuon rapidity spectra per invariant mass bin for data and MC events. There are six mass bins between 20 and 1500 GeV, from left to right and from top to bottom. The NNLO reweighted POWHEG MC signal sample is used. The EW histogram indicates the diboson and W+jets production. The normalization factors are determined using the number of events in data in the Z-peak region, and they are applied to all of the mass bins. Error bars are statistical only.

dibosons to the e^+e^- spectrum are estimated from $e\mu$ data. The simulation accurately describes the sample of $e\mu$ events, both in terms of the number of events as well as the shape of the invariant-mass spectrum.

In addition to the genuine e^+e^- events from EW processes, there are events in which jets are falsely identified as electrons. These are either QCD multijet events where two jets pass the electron selection criteria or W+jets events where the W boson decays to an electron and a neutrino, and a jet is misidentified as an electron. The probability for a jet to pass the requirements of the electromagnetic trigger and to be falsely reconstructed as an electron is determined from a sample of events collected with the trigger requirement for a single electromagnetic cluster in the event. To ensure that this sample is dominated by jets, the events are required to have a missing transverse energy $\not\!\!E_T < 10\,\text{GeV}$, and events with more than one particle identified as an electron are rejected. The jet misidentification probability is measured as a function of jet E_T and absolute pseudorapidity $|\eta|$.

The number of e^+e^- background events is then determined from a different sample, the sample of events collected with the double-electron trigger in which at least one electron candidate fails the full electron selection of the analysis. The events from this sample are assigned weights based on the expected misidentification probability for the failing electron candidates, and the sum of the weights yields the prediction for the background from this source. Since events in this double-electron trigger sample with at least one electron failing the full selection contain a small fraction of genuine DY events, the contribution of the latter is subtracted using simulation.

The expected shapes and the relative yields of dielectron events from data and simulation in bins of invariant mass are shown in Fig. 1 in the same format as the dimuon channel. The genuine electron background is largest in high-mass regions, where it reaches up to 15–20% of the observed yields due to $t\bar{t}$ events. At the lowest masses, the genuine electron background level, which is dominated by the DY $\to \tau^+\tau^-$ contribution, becomes significant at $\sim$50 GeV, where it ranges up to 10%. In other mass ranges the genuine electron background is typically a few percent and, in particular, it is very small (less than 0.5%) in the Z-peak region. The background associated with falsely identified electrons is relatively small in the full mass range.

4.3 Resolution and scale corrections

Lepton energy and momentum measurements can directly affect the reconstructed dilepton invariant mass and are, therefore, important in obtaining a correct differential cross section.

The momentum resolution of muons with $p_T < 200\,\text{GeV}$ comes primarily from the measurements in the silicon tracker. A residual misalignment remains in the tracker that is not fully reproduced by the simulation. This misalignment leads to a bias in the reconstructed muon momenta which is removed using a momentum scale correction.

The corrections to muon momenta are extracted separately for positively and negatively charged muons using the average of the $1/p_T$ spectra of muons and the dimuon mass from Z boson decays in bins of muon charge, the polar angle θ, and the azimuthal angle ϕ. The same procedure is followed for both data and MC samples. The correction to $1/p_T$ has two components: an additive component that removes the bias originating from tracker misalignment, and a multiplicative component that corrects for residual mismodeling of the magnetic field. For a 40 GeV muon, the additive correction varies from 0.4% at small $|\eta|$ to 9% at large $|\eta|$. The multiplicative correction is typically much smaller (about 1.0002).

The average reconstructed Z-boson mass is found to be independent of muon ϕ. The position

of the Z-boson mass peak in the corrected distribution is different from the expected Z-boson mass [38] by only $(0.10 \pm 0.01)\%$ in data and $(0.00 \pm 0.01)\%$ in simulation. The small remaining shift in data is corrected by an additional overall scale correction. A detailed description of the correction for the muon momentum is given in Ref. [39].

The electron energy is derived primarily from the measurements of the energy deposited by the electrons in the ECAL. The energy of these deposits is subject to a set of corrections following the standard CMS procedures [36]. In addition, energy scale corrections are obtained from the analysis of the $Z \to e^+e^-$ peak according to the procedure described in Ref. [37]. These energy scale corrections, which go beyond the standard CMS electron reconstruction, range from 0% to 2% depending on the pseudorapidity of the electron.

4.3.1 Unfolding

The effects of detector resolution that cause migration of events among the analysis bins are corrected through an unfolding procedure [40]. This procedure maps the true lepton distribution onto the measured one, while taking into account migration of events into and out of the mass and rapidity range of this measurement. The unfolding procedure used for the differential and double-differential cross section calculations is described below.

The unfolding of the detector resolution effects is performed prior to corrections for FSR. The response matrix T_{ik} for the unfolding, which gives the fraction of events from bin k of the true distribution that ends up reconstructed in bin i, is calculated from simulation:

$$N_i^{\text{obs}} = \sum_k T_{ik} N_k^{\text{true}}. \tag{3}$$

In the case of the measurement of $\mathrm{d}\sigma/\mathrm{d}m$, the matrix is nearly diagonal with a few significant off-diagonal elements located adjacent to the main diagonal. The effect of regularization on the unfolding is tested using simulation and found to be negligible. Therefore, both the dimuon and dielectron response matrices are inverted without regularization.

For the double-differential cross section measurement, a specific procedure has been developed in order to take into account the effect of migration in bins of dilepton rapidity. Within the framework of the unfolding method for the double-differential cross section measurement, a two-dimensional yield distribution (matrix) in bins of dilepton invariant mass and rapidity is transformed into a one-dimensional distribution by mapping onto a one-dimensional vector. This procedure amounts to a simple index transformation without any loss of information. Once the one-dimensional distribution is obtained, the unfolding procedure follows closely the standard technique for the differential $\mathrm{d}\sigma/\mathrm{d}m$ measurement described in [15]. The unfolding response matrix T_{ik} is calculated from simulation corresponding to the one-dimensional yield vector in Eq. (3). The structure of the response matrix is quite different from the corresponding matrix derived using the yields binned in invariant mass only. The matrix consists primarily of three diagonal-dominated blocks. There are two types of off-diagonal elements in this response matrix. The elements adjacent to the diagonals originate from migration between rapidity bins within the same mass bin. Two additional sets of diagonal dominated blocks originate as a result of migration between adjacent mass bins. The response matrix is inverted and used to unfold the one-dimensional spectrum:

$$N_k^{\text{u}} = N_k^{\text{true}} = \sum_i (T^{-1})_{ki} N_i^{\text{obs}}. \tag{4}$$

Finally, the unfolded distribution is mapped back into the two-dimensional invariant mass-rapidity distribution by performing an index transformation.

A set of tests was performed to validate this unfolding procedure. A closure test, performed using simulation, confirmed the validity of the procedure. The robustness of the method with respect to statistical fluctuations in the matrix elements was checked with a test on an ensemble of MC pseudo-experiments, described in Section 4.7.

The effects of the unfolding correction in the differential cross section measurement are approximately 30% (dimuon) and 60% (dielectron) due to the detector resolution in the Z-peak region, where the invariant mass spectrum changes steeply. In other regions they are less significant, on the order of 5% (dimuon) and 10% (dielectron). The effect in the double-differential cross section measurement is less pronounced since both the invariant mass and rapidity bin sizes are wider than the respective detector resolutions, but it reaches 5% in the high-rapidity region, $|y| > 2.0$.

4.4 Efficiency

The event efficiency ε is defined as the probability for an event within the acceptance to pass the reconstruction procedure and the selection process. The event efficiency is obtained from simulation and is corrected by an efficiency scale factor ρ, which is a ratio of efficiencies and takes into account differences between data and simulation. The determination of the event efficiency is based on the signal MC samples described in Section 3. It is calculated as the ratio of the number of events that pass full reconstruction and selection to the number of events that are found within the acceptance at the generator level.

The event efficiency is significantly affected by the pileup in the event. The average pileup depends on the data taking conditions and typically increased throughout the data taking in 2011. The pileup affects primarily the electron isolation efficiency (up to 5%) whereas the effect on the muon isolation efficiency is less than 1%. The procedures outlined below are used to extract the efficiency corrections for both the $\mathrm{d}\sigma/\mathrm{d}m$ and the $\mathrm{d}^2\sigma/\mathrm{d}m\,\mathrm{d}|y|$ measurements from data.

4.4.1 Dimuon efficiency

The scale factor ρ accounts for the differences in both the single-muon and the dimuon selections. The single-muon properties (including the trigger) are determined using $\mathrm{Z} \to \mu^+\mu^-$ events in data and simulation, where one muon, the tag, satisfies the tight selection requirements, and the selection criteria are applied to the other muon as a probe (tag-and-probe method [37]). An event sample with a single-muon trigger (the tag) is used to evaluate this scale factor. The dimuon selection scale factor is based on the dimuon vertex efficiency as measured in data and simulation after the rest of the selection is applied.

The total event selection efficiency in the dimuon channel is factorized in the following way:

$$\varepsilon = \varepsilon(\mu_1) \cdot \varepsilon(\mu_2) \cdot \varepsilon(\text{dimuon}) \cdot \varepsilon(\text{event, trig}), \tag{5}$$

where

- $\varepsilon(\mu)$ is the single muon efficiency;
- $\varepsilon(\text{dimuon})$ is the efficiency that the two muon tracks of the selected dimuon event come from a common vertex and satisfy the angular requirement between them;

- $\varepsilon(\text{event, trig})$ is the efficiency of triggering an event in both L1 and HLT. It includes the efficiency of matching an identified muon to a trigger object.

The single-muon efficiency is factorized into the following three factors:

$$\varepsilon(\mu) = \varepsilon(\text{track}) \cdot \varepsilon(\text{reco+id}) \cdot \varepsilon(\text{iso}), \tag{6}$$

where

- $\varepsilon(\text{track})$ is the offline track reconstruction efficiency, i.e., the efficiency that a muon track is identified in the tracker;
- $\varepsilon(\text{reco+id})$ is the muon reconstruction and identification efficiency, i.e., the efficiency that the reconstructed track passes all the offline muon quality requirements;
- $\varepsilon(\text{iso})$ is the muon isolation efficiency, i.e., the efficiency of an identified muon to pass the isolation requirement.

The double-muon trigger has asymmetric p_{T} selections for the two legs and, therefore, the efficiency for a muon to trigger the high-p_{T} leg (leg 1) is different from the efficiency for a muon to trigger the low-p_{T} leg (leg 2). We define single-leg efficiencies where $\varepsilon(\mu, \text{trig1})$ is the efficiency of a muon selected offline to be matched to one leg of the double-muon trigger, and $\varepsilon(\mu, \text{trig2})$ is the efficiency of a muon selected offline to be matched to the other leg of the double-muon trigger. The efficiency factor $\varepsilon(\mu, \text{trig1})$ corresponds to a muon matched to the leg of the double-muon trigger that has the higher p_{T} threshold. The double-muon trigger efficiency can then be factorized with single-muon trigger efficiencies in the following way, which takes into account the different efficiencies for the two legs:

$$\begin{aligned} \varepsilon(\text{event, trig}) &= 1 - P(\text{one leg, failed}) - P(\text{two legs, failed}) \\ &= \varepsilon(\mu_1, \text{trig1}) \cdot \varepsilon(\mu_2, \text{trig2}) + \varepsilon(\mu_1, \text{trig2}) \cdot \varepsilon(\mu_2, \text{trig1}) \\ &\quad - \varepsilon(\mu_1, \text{trig1}) \cdot \varepsilon(\mu_2, \text{trig1}), \end{aligned} \tag{7}$$

where

- $P(\text{one leg, failed})$ is the probability that exactly one muon fails to trigger a leg, i.e., $\varepsilon(\mu_1, \text{trig1}) \cdot (1 - \varepsilon(\mu_2, \text{trig2})) + \varepsilon(\mu_2, \text{trig1}) \cdot (1 - \varepsilon(\mu_1, \text{trig2}))$;
- $P(\text{two legs, failed})$ is the probability that both muons fail to trigger a leg, i.e., $(1 - \varepsilon(\mu_1, \text{trig1})) \cdot (1 - \varepsilon(\mu_2, \text{trig1}))$.

For these measurements the combinatorial background of tag-probe pairs not coming from the Z-boson signal are subtracted using a simultaneous maximum-likelihood fit to the invariant mass spectra for passing and failing probes with identical signal and background shapes.

Finally, the efficiency scale factor ρ is measured to be 1.00–1.02 in most of the phase space, although it rises to 1.10 at high dimuon rapidity.

4.4.2 Dielectron efficiency

The factorization of the event efficiency for the electron and the dielectron channel analysis is similar to that of the muon analysis. The total event selection efficiency is given by

$$\varepsilon = \varepsilon(\mathrm{e}_1) \cdot \varepsilon(\mathrm{e}_2) \cdot \varepsilon(\text{event, trig}), \tag{8}$$

where the two $\varepsilon(\mathrm{e})$ factors are the single-electron efficiencies for the two electrons in the candidate and $\varepsilon(\text{event, trig})$ is the efficiency of triggering on the event. There is no factor $\varepsilon(\text{dielectron})$ analogous to the one in Eq. (5) because there is no requirement in the selection for dielectron candidates that depends on parameters of both electrons at the same time except for the requirement to originate from the common vertex. This factor, however, is absorbed into the single-electron efficiency by requiring for each electron a small impact parameter with respect to the primary vertex of the event.

The single-electron efficiency is factorized as

$$\varepsilon(\mathrm{e}) = \varepsilon(\text{reco}) \cdot \varepsilon(\text{id+iso}), \tag{9}$$

where

- the efficiency to detect a supercluster (SC) is known to be very close to 100% [41];
- $\varepsilon(\text{reco})$ is the offline electron reconstruction efficiency, i.e., the probability that, given a SC is found, an electron is reconstructed and passes the offline selection;
- $\varepsilon(\text{id+iso})$ is the efficiency to pass the selection criteria specific to this measurement, including identification, isolation, and conversion rejection, given that the electron candidate has already passed the previous stage of the offline selection.

The efficiency for an event to pass the trigger is computed in the following way:

$$\varepsilon(\text{event, trig}) = \varepsilon(\mathrm{e}_1, (\text{trig1.OR.trig2})) \cdot \varepsilon(\mathrm{e}_2, (\text{trig1.OR.trig2})), \tag{10}$$

where $\varepsilon(\mathrm{e}_i, (\text{trig1.OR.trig2}))$ is the efficiency for each electron to match either one of the two trigger legs. This factorization is simpler than that of muons given by Eq. (7) because for the dielectron trigger, unlike the case for the dimuon trigger, it is measured that $\varepsilon(\mathrm{e}, \text{trig1}) \approx \varepsilon(\mathrm{e}, \text{trig2}) \approx \varepsilon(\mathrm{e}, (\text{trig1.OR.trig2}))$ so Eq. (7) simplifies to Eq. (10).

For the electron channel, the efficiencies for electron reconstruction and selection and the trigger efficiencies are obtained from $\mathrm{Z} \to \mathrm{e}^+\mathrm{e}^-$ data and MC samples following the same tag-and-probe method described above for the muons.

The efficiency scale factor ρ is measured to be in the range of 0.98–1.02, with the values above 1.00 for dielectron masses $m < 40\,\text{GeV}$ and nearly constant at 0.98 above 45 GeV.

4.5 Acceptance

The geometrical and kinematic acceptance A is defined as the fraction of simulated signal events with both leptons falling within the detector fiducial volume. The detector fiducial volume is defined by the nominal p_T and η requirements for an analysis using the simulated leptons after the FSR simulation. It is determined from simulation using the NNLO reweighted POWHEG MC sample.

The signal event selection efficiency ϵ for a given mass bin is the fraction of events inside the acceptance that pass the full selection. This definition uses the same generator-level quantities after the FSR correction in both the numerator and denominator (as in the acceptance definition). The following equation holds:

$$A \times \epsilon \equiv \frac{N^A}{N^{\text{gen}}} \cdot \frac{N^\epsilon}{N^A} = \frac{N^\epsilon}{N^{\text{gen}}}, \tag{11}$$

where N^{gen} is the number of generated signal events in a given invariant mass bin, N^{A} is the number of events inside the geometrical and kinematic acceptance, and N^{ϵ} is the number of events passing the analysis selection. The efficiency is estimated using the NNLO reweighted POWHEG simulation.

The acceptance calculation depends on higher-order QCD corrections and the choice of PDFs. The use of an NNLO signal MC is essential, especially in the low-mass region where the difference between the NLO and NNLO predictions is sizable.

Figure 3 shows the acceptance, the event efficiency, and $A \times \epsilon$ as functions of the dilepton invariant mass.

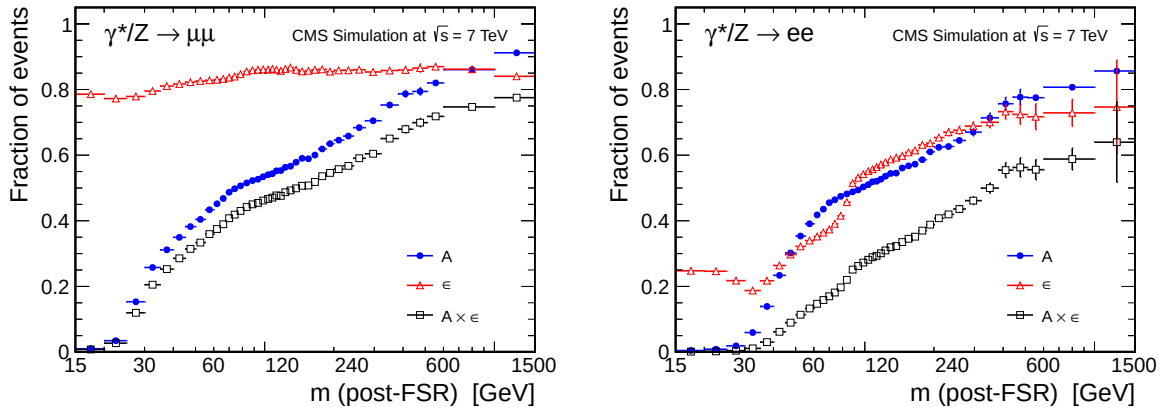

Figure 3: The DY acceptance, efficiency, and their product per invariant mass bin in the dimuon channel (left) and the dielectron channel (right), where m(post-FSR) means dimuon invariant mass after the FSR.

4.6 Final-state QED radiation effects

Leptons can radiate photons in a process referred to as FSR. This FSR effect changes the observed invariant mass, which is computed from the four-momenta of the two leptons. When FSR photons with sizable energy are emitted, the observed mass can be substantially lower than the original DY mass. The effect is most pronounced just below the Z peak, where the 'radiative' events in the Z peak are shifted lower in mass and become a significant contribution to that mass region.

The correction for FSR is performed separately from the correction for detector resolution. It aims to transform a post-FSR track (i.e., after radiation and thus closer to the actual measurement) into a pre-FSR track before any radiation that is more representative of the original track. The FSR correction procedure is performed in three steps:

1. A bin-by-bin correction for the events in which pre-FSR leptons fail the acceptance requirements, while post-FSR leptons pass. At the analysis level we deal with only post-FSR events and this correction, based on MC simulations, scales back the sample to contain only events that pass the acceptance requirements in both pre- and post-FSR. The correction is applied before the FSR unfolding, and is somewhat similar to a background correction.

2. An unfolding procedure is used for the events in which both pre- and post-FSR leptons pass the acceptance requirements, for which we can construct a response matrix similar to that of Eq. (4).

3. A bin-by-bin correction is used for the events in which pre-FSR leptons pass the acceptance requirements, but post-FSR leptons fail those requirements. These events do not enter the response matrix, but they need to be taken into account. This correction is applied after the FSR unfolding, and is similar to an efficiency correction.

The correction for the events from step 1 is quite small, reaching its maximum of 1% right below the Z peak.

The unfolding procedure for the events from step 2 follows the unfolding procedure for the resolution. The response matrix is derived from the NNLO reweighted POWHEG MC sample, using pre- and post-FSR yields.

The bin-by-bin correction for the events from step 3 is significant at low mass, reaching a maximum of 20% in the lowest mass bin and decreasing to negligible levels in the Z-peak region.

The same method is applied in the double-differential cross section measurement. The structure of the response matrix is quite different from the corresponding matrix derived using the yields binned in invariant mass only. The matrix consists of a set of diagonal-dominated blocks, which originate from migration between mass bins in the pre- and post-FSR distributions.

The effect of the FSR unfolding correction in the differential cross section measurement is significant in the mass region 50–80 GeV, below the Z peak. In this region, the magnitude of the effect is of the order of 30–50% (40–60%) for the dimuon (dielectron) channel. In other regions, the effect is of the order of 10–15% in both channels. In the double-differential cross section measurement, the effect of FSR unfolding is small, typically a few percent, due to a larger mass bin size.

4.7 Systematic uncertainties

In this section, we discuss the evaluation of the systematic uncertainties, which are shown in Tables 1–5 for both the differential and the double-differential cross section measurements. The methods used to evaluate the uncertainties are described in Ref. [15].

The estimated uncertainty in the center-of-mass energy is 0.65% or 46 GeV at 7 TeV [42]. This would result in an additional uncertainty in the absolute differential cross section of 0.3% in the low-mass region, 0.6% in the Z-peak region and 1.0% in the high-mass region on the average. We do not explicitly include these uncertainties in the systematic uncertainties.

4.7.1 Dimuon systematic uncertainties

The main uncertainty in the dimuon signal comes from the efficiency scale factor ρ that reflects systematic deviations that vary up to 2% between the data and the simulation. As discussed in Section 4.4, single-muon efficiencies of several types are measured with the tag-and-probe procedure and are combined into event efficiency scale factors. The tag-and-probe procedure yields the efficiency of each type and an associated statistical uncertainty. A variety of possible systematic biases in the tag-and-probe procedure has been investigated, such as dependence on binning in single-muon p_{T} and η, dependence on the assumed shape of signal and background in the fit model, and others. Appropriate systematic uncertainties in the single-muon efficiency scale factors have been assigned. The effect of the combined statistical and systematic uncertainties in the event scale factors ρ on the final result constitutes the final systematic uncertainty from this source. This uncertainty is evaluated by recomputing the final result multiple times using an ensemble of the single-muon efficiency maps where the entries are modified randomly within ± 1 standard deviation of the combined statistical and systematic

uncertainties in the map bins. The uncertainties estimated by this method are available in Tables 1–5. The contribution from the dimuon vertex selection is small because its efficiency scale factor is consistent with being constant; the statistical fluctuations are treated as systematic.

The uncertainty in the muon momentum scale arises from the efficiency estimation, the background subtraction, the detector resolution effect, the modeling of the Z-boson p_{T} spectrum, and the modeling of the FSR. To assign a systematic uncertainty corresponding to the muon momentum scale correction in the measurement, the correction is shifted by one standard deviation of its total uncertainty and the deviation of the differential cross section from the central value is assigned as the systematic uncertainty. This uncertainty is used to estimate the systematic uncertainty of the detector resolution by the unfolding method.

We assign a systematic uncertainty in the unfolding of detector resolution effects from two sources: (1) up to 1.5% uncertainty from the momentum scale correction, which is determined as a difference between the central and shifted values of the unfolded distribution; and (2) up to 0.5% uncertainty in the momentum scale correction estimation method. We assign an additional systematic uncertainty to the unfolding procedure, which also consists of two sources: (1) up to 1% uncertainty due to the systematic difference between data and simulation (which must be taken into account because the response matrix is fully determined from simulation), and (2) up to 1% uncertainty in the unfolding method. To estimate the uncertainty due to the systematic difference between data and simulation, a bias in unfolding is simulated by using the migration matrix from simulation in bins of the true and measured masses, generating ensembles of pseudo-experiments of true and measured data while holding the response matrix fixed. Each ensemble is obtained by smearing the initial observed yield vector with a random Gaussian distribution (taking the width of the Gaussian equal to 1% of the yield value in a given bin, which provides sufficient variation within the detector resolution). These ensembles of pseudo-experiments are unfolded and the pull of each ensemble is taken. The mean of the pulls over the set of ensembles is calculated, and the corresponding systematic uncertainty is assigned as

$$\frac{\delta N^{\mathrm{obs}}|_{\mathrm{syst}}}{N_{\mathrm{u}}} = \mu_{\mathrm{pulls}} \cdot \frac{\delta N^{\mathrm{obs}}|_{\mathrm{stat}}}{N_{\mathrm{u}}}. \tag{12}$$

The systematic effect of the unfolding is generally small (less than 1%), except in the Z-peak region where it reaches 1–3%.

The uncertainties in the backgrounds are evaluated using different methods for the estimates coming from data and simulation. The QCD multijet, $\mathrm{t\bar{t}}$, and tW background estimates are based on data, whereas all the other backgrounds are evaluated from simulation. For backgrounds derived from data, the uncertainty is based on two sources: (1) the Poissonian statistical uncertainty of predicted backgrounds (which is treated as systematic); and (2) the difference between the prediction from the data and simulation. In the case of an estimate based on simulation, the uncertainty is estimated in a similar way: (1) the Poissonian statistical uncertainty from the size of the MC sample (which is treated as systematic); and (2) the systematic uncertainty due to the knowledge of the theoretical cross section. The two components are combined in quadrature in both cases.

The systematic uncertainty due to the model-dependent FSR simulation in the dimuon channel is estimated using two reweighting techniques. One is the electroweak radiative correction [43]. This correction is applied to the electromagnetic coupling constant and the difference in total event counts between the reweighted and original events is assigned as a systematic uncertainty. The second uses photons reconstructed near a muon. In this case, the additional scale

factors are determined by comparing data and simulation using three distributions: the number of photons, photon energy, and $\Delta R(\mu, \gamma)$. These factors are applied to the signal MC events. The effect from the photons is nonnegligible in the low-mass region ($m < 45\,\text{GeV}$) where a large contribution from falsely identified photons yields an additional systematic uncertainty.

The acceptance times efficiency uncertainty dominates at low mass. It contains a component related to the statistics of the MC sample that limits our knowledge of the product $A \times \epsilon$, which we treat as systematic. There are two main theoretical uncertainties: the first one arises from our imperfect knowledge of the nonperturbative PDFs that participate in the hard scattering, and the second is the modeling of the hard-interaction process, that is, the effects of higher-order QCD corrections. These contributions are largest at low mass (10%) and decrease to less than 1% for masses above the Z-boson peak. Higher-order EW corrections are small in comparison to FSR corrections. They increase for invariant masses in the TeV region, but are insignificant compared to the experimental precision for the whole mass range under study.

The PDF uncertainties for the differential and double-differential cross section measurements are calculated using the LHAGLUE interface to the PDF library LHAPDF 5.8.7 [44, 45], by applying a reweighting technique with asymmetric uncertainties as described in Ref. [46]. The PDF uncertainty in the acceptance and the modeling is not considered as a part of the resulting uncertainty in the measurement, but rather is used to facilitate comparison with theoretical models. The modeling uncertainty is discussed in Section 3.

The systematic uncertainties in the dimuon channel are summarized in Table 1 for the $\mathrm{d}\sigma/\mathrm{d}m$ differential cross section and in Tables 3–5 for the $\mathrm{d}^2\sigma/\mathrm{d}m\,\mathrm{d}|y|$ double-differential cross section.

4.7.2 Dielectron systematic uncertainties

In the dielectron channel, the leading systematic uncertainty is associated with the energy scale corrections for individual electrons. The corrections affect both the placement of a given candidate in a particular invariant mass bin and the likelihood of surviving the kinematic selection. The energy scale correction itself is calibrated to 1–2% precision. Several sources of systematic uncertainties due to the energy scale correction are considered: (1) the uncertainty in the energy scale corrections; (2) the residual differences in simulated and measured distributions; (3) the choice of line shape modeling; and (4) the choice of η binning. The associated uncertainty in the signal yield is calculated by varying the energy scale correction value within its uncertainty and remeasuring the yield. The electron energy scale uncertainty takes its largest values for the bins near the central Z-peak bin because of sizable event migration. This uncertainty for the electron channel is roughly 20 times larger than the momentum scale uncertainty for muons, for which the associated systematic uncertainties in the cross section are rather small.

Another significant uncertainty for electrons results from the uncertainty in the efficiency scale factors. The systematic uncertainty in the scale factors as well as the resulting uncertainty in the normalized cross section are found with the same procedure as for the muon channel.

The uncertainty associated with the unfolding procedure in the electron channel comes primarily from the uncertainty in the unfolding matrix elements due to imperfect simulation of detector resolution. This simulation uncertainty for electrons is significantly larger than for muons, leading to a larger systematic uncertainty in the normalized cross section. The dielectron background uncertainties are evaluated by comparing the background yields calculated as described in Section 4.2 with predictions from simulation. These uncertainties become dominant at the higher invariant masses above the Z-boson peak.

The systematic effects due to the FSR simulation uncertainty for the electron channel primar-

Table 1: Summary of the systematic uncertainties for the dimuon channel $d\sigma/dm$ measurement. The "Total" is a quadratic sum of all sources except for the Acc.+PDF and Modeling.

m (GeV)	Eff. ρ (%)	Det. resol. (%)	Bkgr. est. (%)	FSR (%)	Total (%)	Acc.+PDF (%)	Modeling (%)
15–20	1.90	0.03	0.28	0.54	2.09	2.29	9.70
20–25	2.31	0.24	0.63	0.47	2.47	3.15	3.10
25–30	2.26	0.27	2.95	0.40	3.76	2.73	1.90
30–35	1.48	0.17	1.94	0.46	2.50	2.59	0.70
35–40	1.19	0.09	1.26	0.66	1.88	2.61	0.50
40–45	1.12	0.07	0.97	0.30	1.54	2.49	0.30
45–50	1.10	0.07	0.86	0.44	1.50	2.51	0.10
50–55	1.07	0.10	0.67	0.58	1.42	2.44	0.10
55–60	1.07	0.15	0.69	0.77	1.52	2.36	0.20
60–64	1.06	0.19	0.35	0.94	1.50	2.27	0.20
64–68	1.06	0.22	0.24	1.06	1.55	2.22	0.30
68–72	1.06	0.30	0.20	1.13	1.60	2.20	0.20
72–76	1.05	0.51	0.15	1.13	1.65	2.18	0.20
76–81	1.06	0.94	0.25	1.01	1.77	2.15	0.20
81–86	1.11	1.56	0.10	0.69	2.06	2.18	0.10
86–91	1.07	2.21	0.01	0.23	2.48	2.12	0.20
91–96	1.08	2.55	0.01	0.12	2.78	2.14	0.20
96–101	1.29	2.32	0.08	0.15	2.68	2.12	0.30
101–106	1.31	1.69	0.14	0.19	2.17	2.07	0.30
106–110	1.32	1.05	0.28	0.22	1.76	2.01	0.50
110–115	1.34	0.65	0.34	0.25	1.59	1.97	0.60
115–120	1.33	0.47	0.43	0.27	1.55	1.95	0.60
120–126	1.36	0.37	0.56	0.29	1.60	1.91	0.50
126–133	1.35	0.33	0.70	0.30	1.65	1.88	0.60
133–141	1.31	0.42	0.90	0.32	1.75	1.85	0.70
141–150	1.29	0.64	1.08	0.35	1.91	1.81	1.00
150–160	1.36	0.87	1.20	0.39	2.13	1.82	1.10
160–171	1.42	0.99	1.48	0.39	2.39	1.82	1.10
171–185	1.53	0.96	1.72	0.41	2.61	1.75	1.10
185–200	1.60	0.77	1.80	0.51	2.67	1.75	1.10
200–220	1.71	0.52	1.82	0.42	2.64	1.53	1.00
220–243	1.75	0.39	2.28	0.44	3.01	1.48	1.50
243–273	1.86	0.49	2.46	0.46	3.23	1.40	1.40
273–320	1.90	0.72	2.37	0.50	3.24	1.31	1.30
320–380	1.90	0.96	2.88	0.57	3.73	1.28	1.50
380–440	1.93	1.31	3.54	0.57	4.44	1.45	1.20
440–510	1.97	1.74	4.64	0.57	5.50	1.60	1.30
510–600	2.02	1.79	4.48	0.57	5.28	0.50	2.10
600–1000	2.01	1.13	5.07	0.57	5.61	0.41	2.40
1000–1500	2.14	0.48	15.34	0.57	15.51	0.24	3.10

Table 2: Summary of the systematic uncertainties for the dielectron channel $d\sigma/dm$ measurement. E-scale indicates the energy scale uncertainty. The "Total" is a quadratic sum of all sources except for the Acc.+PDF and Modeling.

m (GeV)	E-scale (%)	Eff. ρ (%)	Det. resol. (%)	Bkgr. est. (%)	Total (%)	Acc.+PDF (%)	Modeling (%)
15–20	1.4	3.0	1.9	0.3	3.8	3.0	9.7
20–25	2.5	2.3	3.3	0.7	4.8	2.2	3.1
25–30	1.5	2.7	1.9	1.1	3.8	2.2	1.9
30–35	1.4	3.2	1.4	4.4	5.8	2.2	0.7
35–40	0.6	2.3	1.1	5.5	6.1	2.1	0.5
40–45	0.7	1.8	1.1	7.1	7.4	2.0	0.3
45–50	0.7	1.5	1.3	8.9	9.1	2.0	0.1
50–55	3.3	1.2	1.7	3.4	5.2	2.0	0.1
55–60	2.8	1.0	2.4	2.5	4.5	2.0	0.2
60–64	6.4	0.9	3.8	2.7	8.0	1.9	0.2
64–68	2.4	0.9	4.9	2.4	6.0	1.9	0.3
68–72	2.1	0.9	5.2	1.8	5.9	1.9	0.2
72–76	1.5	0.8	5.3	1.2	5.7	1.8	0.2
76–81	2.0	0.8	3.7	0.5	4.4	1.8	0.2
81–86	5.9	0.8	2.3	0.2	6.4	1.7	0.1
86–91	8.8	0.7	0.7	0.1	8.8	1.7	0.2
91–96	8.4	0.7	0.7	0.0	8.4	1.7	0.2
96–101	15.6	0.7	3.7	0.2	16.1	1.7	0.3
101–106	17.6	0.8	5.8	0.4	18.6	1.7	0.3
106–110	10.4	0.9	13.1	1.0	16.7	1.7	0.5
110–115	5.5	0.9	10.2	1.2	11.6	1.6	0.6
115–120	2.5	1.0	10.2	1.6	10.7	1.6	0.6
120–126	2.0	1.1	8.1	1.9	8.6	1.6	0.5
126–133	2.9	1.2	6.0	2.1	7.1	1.6	0.6
133–141	4.9	1.2	4.7	2.1	7.2	1.6	0.7
141–150	3.3	1.3	4.7	2.7	6.5	1.6	1.0
150–160	3.5	1.4	4.9	3.1	6.9	1.6	1.1
160–171	6.7	1.5	3.9	2.6	8.3	1.7	1.1
171–185	5.6	1.6	4.1	3.6	8.0	1.6	1.1
185–200	4.1	1.6	3.8	3.4	6.7	1.7	1.1
200–220	2.6	1.7	2.9	3.1	5.3	1.6	1.0
220–243	1.8	1.9	3.3	3.9	5.7	1.7	1.5
243–273	1.6	2.0	3.4	4.0	5.9	1.7	1.4
273–320	1.1	2.1	3.0	4.4	5.9	1.7	1.3
320–380	1.8	2.5	3.7	4.2	6.4	1.9	1.5
380–440	3.3	3.2	5.8	5.8	9.4	2.3	1.2
440–510	3.2	3.8	5.3	5.0	8.8	2.8	1.3
510–600	3.4	1.3	1.2	3.8	5.4	0.6	2.1
600–1000	1.5	1.3	2.2	7.1	7.7	0.5	2.4
1000–1500	7.8	0.9	1.3	33.3	34.2	0.4	3.1

Table 3: Summary of systematic uncertainties in the dimuon channel for $20 < m < 30\,\text{GeV}$ and $30 < m < 45\,\text{GeV}$ bins as a function of $|y|$. The "Total" is a quadratic sum of all sources.

$\|y\|$	Eff. ρ (%)	Det. resol. (%)	Bkgr. est. (%)	FSR (%)	Total (%)
	$20 < m < 30\,\text{GeV}$				
0.0–0.1	6.21	0.29	0.57	0.76	6.29
0.1–0.2	6.01	0.37	0.56	0.58	6.07
0.2–0.3	6.01	0.33	0.55	1.15	6.15
0.3–0.4	5.57	0.41	0.48	0.57	5.63
0.4–0.5	5.21	0.45	0.56	0.70	5.31
0.5–0.6	4.87	0.32	0.57	0.54	4.94
0.6–0.7	4.51	0.33	0.52	0.64	4.60
0.7–0.8	3.89	0.38	0.55	0.42	3.97
0.8–0.9	3.42	0.31	0.54	0.57	3.52
0.9–1.0	3.14	0.26	0.53	0.77	3.29
1.0–1.1	2.92	0.49	0.53	0.61	3.07
1.1–1.2	2.87	0.50	0.58	0.47	3.01
1.2–1.3	3.09	0.44	0.51	0.46	3.20
1.3–1.4	3.62	0.37	0.62	0.47	3.72
1.4–1.5	3.87	0.50	0.60	0.92	4.05
1.5–1.6	4.12	0.55	0.59	0.44	4.22
1.6–1.7	4.40	0.62	0.66	0.48	4.52
1.7–1.8	4.76	0.51	0.65	0.45	4.85
1.8–1.9	4.82	0.76	0.71	0.69	4.98
1.9–2.0	4.88	0.60	0.69	0.56	4.99
2.0–2.1	4.84	0.46	0.72	1.26	5.07
2.1–2.2	5.22	0.67	0.89	1.68	5.59
2.2–2.3	6.84	1.16	1.02	3.37	7.78
2.3–2.4	8.40	1.14	1.56	4.96	9.94
	$30 < m < 45\,\text{GeV}$				
0.0–0.1	3.03	0.08	0.36	0.88	3.18
0.1–0.2	2.72	0.03	0.38	0.82	2.87
0.2–0.3	2.50	0.07	0.42	0.98	2.71
0.3–0.4	2.30	0.03	0.38	1.13	2.59
0.4–0.5	2.21	0.11	0.38	1.03	2.47
0.5–0.6	2.25	0.10	0.34	0.74	2.39
0.6–0.7	2.39	0.05	0.37	0.69	2.51
0.7–0.8	2.46	0.05	0.40	0.89	2.65
0.8–0.9	2.48	0.05	0.37	0.63	2.58
0.9–1.0	2.39	0.05	0.38	0.74	2.53
1.0–1.1	2.32	0.11	0.39	0.80	2.48
1.1–1.2	2.18	0.03	0.40	0.58	2.29
1.2–1.3	2.12	0.06	0.44	0.71	2.28
1.3–1.4	2.04	0.04	0.34	0.53	2.13
1.4–1.5	2.03	0.04	0.37	0.63	2.16
1.5–1.6	2.02	0.07	0.39	0.66	2.16
1.6–1.7	2.02	0.12	0.36	0.87	2.24
1.7–1.8	2.14	0.06	0.33	0.80	2.31
1.8–1.9	2.47	0.10	0.45	1.13	2.75
1.9–2.0	2.74	0.20	0.45	1.08	2.99
2.0–2.1	3.21	0.20	0.53	1.67	3.66
2.1–2.2	3.86	0.19	0.71	2.52	4.67
2.2–2.3	5.36	0.21	2.30	2.88	6.51
2.3–2.4	6.71	0.09	2.38	6.30	9.51

Table 4: Summary of systematic uncertainties in the dimuon channel for $45 < m < 60\,\text{GeV}$ and $60 < m < 120\,\text{GeV}$ bins as a function of $|y|$. The "Total" is a quadratic sum of all sources.

$\|y\|$	Eff. ρ (%)	Det. resol. (%)	Bkgr. est. (%)	FSR (%)	Total (%)
	$45 < m < 60\,\text{GeV}$				
0.0–0.1	1.75	0.02	0.48	0.93	2.04
0.1–0.2	1.70	0.15	0.49	1.19	2.14
0.2–0.3	1.64	0.05	0.54	1.74	2.45
0.3–0.4	1.52	0.07	0.50	1.60	2.26
0.4–0.5	1.45	0.04	0.54	3.12	3.48
0.5–0.6	1.37	0.08	0.47	0.71	1.61
0.6–0.7	1.38	0.04	0.50	1.09	1.83
0.7–0.8	1.38	0.05	0.56	1.71	2.27
0.8–0.9	1.39	0.02	0.49	0.62	1.60
0.9–1.0	1.44	0.07	0.54	0.70	1.69
1.0–1.1	1.44	0.02	0.48	1.07	1.86
1.1–1.2	1.53	0.08	0.42	1.92	2.50
1.2–1.3	1.63	0.10	0.47	1.25	2.11
1.3–1.4	1.55	0.03	0.38	0.72	1.75
1.4–1.5	1.40	0.23	0.38	0.77	1.65
1.5–1.6	1.31	0.03	0.33	2.29	2.66
1.6–1.7	1.34	0.11	0.39	1.37	1.96
1.7–1.8	1.41	0.04	0.70	1.17	1.96
1.8–1.9	1.52	0.07	0.30	3.04	3.42
1.9–2.0	1.69	0.02	0.31	4.16	4.50
2.0–2.1	1.78	0.06	0.55	5.31	5.63
2.1–2.2	2.21	0.31	1.27	4.42	5.11
2.2–2.3	2.96	0.11	0.62	9.98	10.4
2.3–2.4	4.76	0.11	0.26	15.1	15.8
	$60 < m < 120\,\text{GeV}$				
0.0–0.1	0.83	0.004	0.04	0.29	0.88
0.1–0.2	0.83	0.01	0.04	0.29	0.88
0.2–0.3	0.84	0.01	0.04	0.29	0.89
0.3–0.4	0.87	0.01	0.04	0.29	0.92
0.4–0.5	0.89	0.01	0.04	0.29	0.94
0.5–0.6	0.90	0.01	0.04	0.29	0.94
0.6–0.7	0.89	0.01	0.04	0.29	0.94
0.7–0.8	0.89	0.02	0.04	0.29	0.94
0.8–0.9	0.92	0.01	0.03	0.29	0.97
0.9–1.0	0.97	0.02	0.03	0.34	1.03
1.0–1.1	1.03	0.03	0.04	0.30	1.08
1.1–1.2	1.10	0.02	0.03	0.29	1.13
1.2–1.3	1.16	0.02	0.03	0.31	1.20
1.3–1.4	1.20	0.04	0.03	0.32	1.24
1.4–1.5	1.23	0.03	0.05	0.32	1.27
1.5–1.6	1.29	0.01	0.05	0.33	1.33
1.6–1.7	1.40	0.02	0.08	0.43	1.47
1.7–1.8	1.53	0.02	0.08	0.43	1.59
1.8–1.9	1.67	0.03	0.05	0.46	1.73
1.9–2.0	2.06	0.04	0.05	0.36	2.09
2.0–2.1	2.78	0.01	0.14	0.62	2.86
2.1–2.2	3.87	0.04	0.07	0.70	3.94
2.2–2.3	5.34	0.02	0.02	0.91	5.41
2.3–2.4	6.41	0.06	0.04	2.08	6.74

Table 5: Summary of systematic uncertainties in the dimuon channel for $120 < m < 200\,\text{GeV}$ and $200 < m < 1500\,\text{GeV}$ bins as a function of $|y|$. The "Total" is a quadratic sum of all sources.

$\|y\|$	Eff. ρ (%)	Det. resol. (%)	Bkgr. est. (%)	FSR (%)	Total (%)
	$120 < m < 200\,\text{GeV}$				
0.0–0.1	1.68	0.28	2.17	0.56	2.81
0.1–0.2	1.60	0.16	2.03	0.72	2.68
0.2–0.3	1.56	0.26	2.09	1.05	2.82
0.3–0.4	1.57	0.53	1.89	0.78	2.63
0.4–0.5	1.49	0.27	1.67	0.67	2.35
0.5–0.6	1.47	0.25	1.69	0.38	2.29
0.6–0.7	1.57	0.33	1.97	0.54	2.60
0.7–0.8	1.43	0.39	1.62	0.37	2.22
0.8–0.9	1.42	0.07	1.92	0.52	2.44
0.9–1.0	1.35	0.48	1.53	0.37	2.13
1.0–1.1	1.31	0.16	1.37	0.41	1.94
1.1–1.2	1.34	0.36	1.39	0.45	2.02
1.2–1.3	1.51	0.45	1.35	0.57	2.15
1.3–1.4	1.82	0.06	1.26	0.40	2.25
1.4–1.5	2.17	0.85	1.04	0.44	2.59
1.5–1.6	2.76	0.14	1.08	0.43	3.00
1.6–1.7	3.44	0.30	0.83	0.39	3.57
1.7–1.8	4.09	0.41	0.94	1.02	4.34
1.8–1.9	5.37	0.17	1.03	1.09	5.57
1.9–2.0	6.62	0.10	0.84	1.20	6.78
2.0–2.1	8.52	0.16	0.89	0.60	8.58
2.1–2.2	12.3	0.85	0.70	0.51	12.3
2.2–2.3	16.8	0.41	0.95	1.91	16.9
2.3–2.4	20.2	0.51	1.91	1.26	20.4
	$200 < m < 1500\,\text{GeV}$				
0.0–0.2	2.18	0.30	7.51	0.56	7.85
0.2–0.4	1.84	0.04	5.31	0.47	5.64
0.4–0.6	1.68	0.32	4.33	0.53	4.69
0.6–0.8	1.70	0.07	4.57	0.58	4.91
0.8–1.0	1.83	0.12	3.47	0.66	3.99
1.0–1.2	2.28	0.44	3.10	0.66	3.93
1.2–1.4	3.50	0.08	1.92	0.59	4.03
1.4–1.6	5.28	0.65	2.15	0.56	5.77
1.6–1.8	7.14	0.19	2.11	0.98	7.51
1.8–2.0	10.4	0.86	2.17	0.61	10.6
2.0–2.2	17.8	0.15	0.99	0.98	17.8
2.2–2.4	28.8	0.42	1.99	1.36	28.9

ily affect the detector resolution unfolding procedure. The impact of these effects is higher for the electron channel than for the muon channel because of the partial recovery of FSR photons in the supercluster energy reconstruction as well as the overall stronger FSR effects for the electron channel. To evaluate the FSR uncertainty for electrons, we adopt a more conservative approach than the one used for the dimuons. The final results of the measurement are recomputed using a detector resolution unfolding matrix prepared by varying the fraction of events with significant FSR ($>$1 GeV) in simulation by $\pm$5%, and taking the spread as the systematic uncertainty. This component is absorbed into the total detector resolution unfolding systematic uncertainties. The effect of the FSR simulation on other analysis steps for the electron channel is negligible in comparison to other systematic effects associated with those steps.

The PDF uncertainties affecting the acceptance are computed in the same way as described for the muon channel.

The systematic uncertainties for the electron channel are summarized in Table 2.

4.7.3 Covariance matrix

A covariance matrix gives the uncertainties of the measurements together with the correlations between the analysis bins and different systematic sources. There are several distinctive steps in the covariance analysis.

For the muon data sample the measured spectrum is unfolded, which redistributes the signal and background events according to the unfolding matrix T^{-1}, described in Section 4.3.1.

The total uncertainty before the unfolding is given by a diagonal matrix V_I describing all the analysis bins. The mathematical description of the procedure to obtain the covariance matrix V_{UNF} associated with the unfolding is given in Ref. [40]:

$$V_{\mathrm{UNF}} = T^{-1} V_I {T^{-1}}^T. \tag{13}$$

The common normalization to the Z-boson peak does not change the results of the unfolding (matrix) procedure.

After the unfolding, the resulting yield is corrected for detector and reconstruction efficiencies. The largest effect in the uncertainty comes from the efficiency corrections for the single leptons, which are estimated with the tag-and-probe method. A large part of this uncertainty comes from systematic effects related to data/MC variations, together with statistical limitations. The single-lepton efficiency corrections and their uncertainties are propagated to the final results using MC pseudo-experiments, where the correction values are varied according to their measured uncertainties. Similar pseudo-experiments also give the correlations (or directly—the covariance) resulting from the particular choices of the tag-and-probe binning. The normalization to the Z-boson peak is applied by measuring the efficiency correlation effects on the normalized yields. The efficiency covariance and correlations are trivially related by the efficiency correction uncertainties (i.e., by the square roots of the diagonal elements of the efficiency covariance matrix). The efficiency covariance matrix is denoted by V_{EFF}.

The last step in the procedure is to apply FSR corrections to the measurement. As described earlier, it is based on the FSR unfolding matrix and additional bin-by-bin corrections. There are associated uncertainties in the FSR description. As in the first step, the correlations induced by this procedure are described by the FSR unfolding matrix alone and the covariance matrix V_{FSR} is given by Eq. (13), but with the FSR related inputs.

The total covariance matrix V_{tot} is simply by the sum of the three uncorrelated sources:

$$V_{\text{tot}} = V_{\text{UNF}} + V_{\text{EFF}} + V_{\text{FSR}}. \tag{14}$$

In the electron data sample, the covariance of the post-FSR cross section is calculated as a weighted covariance of three independent sources. First, the total uncertainty in the signal yield is propagated through the detector resolution unfolding matrix, as given by Eq. (13). Then the uncertainty is increased by contributions due to the statistical inaccuracy of the unfolding matrix elements as well as additional sources of systematic uncertainty associated with the resolution unfolding (e.g., the electron energy scale uncertainty and FSR). The latter contribution is taken as diagonal. Second, the covariance of the efficiency correction factors is evaluated using pseudo-experiments as described for the muon channel analysis. In this case, efficiency correction factors contribute significantly to correlations in the low-mass region. Third, the diagonal covariance of each MC efficiency factor is obtained from the statistical uncertainty. The covariance of the pre-FSR cross section is obtained from the covariance of the post-FSR cross section via error propagation. After the FSR unfolding some covariances with the Z-boson peak region become negative. The contribution from the statistical uncertainty of the FSR unfolding matrix is negligible. The covariance of the normalized cross section is derived from the covariance of the unnormalized cross section, taking the uncertainty of the Z-peak bin (Table 6) and assuming no correlation between the cross section value in a particular mass bin and the normalization factor.

The covariance matrices are included in the HEPDATA record for this paper.

5 Results and discussion

This section provides a summary of the results for the $\mathrm{d}\sigma/\mathrm{d}m$ cross section measurements in the dielectron and dimuon channels and the $\mathrm{d}^2\sigma/\mathrm{d}m\,\mathrm{d}|y|$ cross section measurement in the dimuon channel.

5.1 Differential cross section $\mathrm{d}\sigma/\mathrm{d}m$ measurement

The result of the measurement is calculated as the ratio

$$R^i_{\text{pre-FSR}} = \frac{N^i_{\text{u}}}{A^i \epsilon^i \rho^i} \Big/ \frac{N^{\text{norm}}_{\text{u}}}{A^{\text{norm}} \epsilon^{\text{norm}} \rho^{\text{norm}}}\,, \tag{15}$$

where N^i_{u} is the number of events after background subtraction and the unfolding procedure for the detector resolution and FSR correction, A^i is the acceptance, ϵ^i is the efficiency, and ρ^i is the correction estimated from data in a given invariant mass bin i as defined earlier. N^{norm}_u, A^{norm}, ϵ^{norm}, and ρ^{norm} refer to the Z-peak region. The DY $\mathrm{d}\sigma/\mathrm{d}m$ differential cross section is normalized to the cross section in the Z-peak region ($60 < m < 120\,\text{GeV}$). The results are also normalized to the invariant mass bin widths, Δm^i, defining the shape $r^i = R^i/\Delta m^i$.

The results of the DY cross section measurement are presented in Fig. 4 for both the muon and the electron channels. The Z-boson production cross sections used as normalization factors in the dimuon and dielectron channels are measured from data. Their values are shown in Table 6. The muon and electron cross sections in the Z-peak region are in good agreement with NNLO predictions for the full phase space (e.g., a typical NNLO prediction is $970 \pm 30\,\text{pb}$) and also with the previous CMS measurements [37, 47].

Table 6: Normalization factors for the cross section measurements from the Z-peak region ($60 < m < 120\,\text{GeV}$) with associated uncertainties.

Muon channel	Cross section in the Z-peak region
pre-FSR full acc.	$989.5 \pm 0.8\,\text{(stat.)} \pm 9.8\,\text{(exp. syst.)} \pm 21.9\,\text{(th. syst.)} \pm 21.8\,\text{(lum.)}\,\text{pb}$
post-FSR full acc.	$974.8 \pm 0.7\,\text{(stat.)} \pm 9.2\,\text{(exp. syst.)} \pm 21.6\,\text{(th. syst.)} \pm 21.4\,\text{(lum.)}\,\text{pb}$
pre-FSR detector acc.	$524.7 \pm 0.4\,\text{(stat.)} \pm 5.1\,\text{(exp. syst.)} \pm 1.2\,\text{(th. syst.)} \pm 11.5\,\text{(lum.)}\,\text{pb}$
post-FSR detector acc.	$516.5 \pm 0.4\,\text{(stat.)} \pm 4.9\,\text{(exp. syst.)} \pm 1.1\,\text{(th. syst.)} \pm 11.4\,\text{(lum.)}\,\text{pb}$
Electron channel	Cross section in the Z-peak region
pre-FSR full acc.	$984.6 \pm 0.9\,\text{(stat.)} \pm 7.3\,\text{(exp. syst.)} \pm 21.4\,\text{(th. syst.)} \pm 21.7\,\text{(lum.)}\,\text{pb}$
post-FSR full acc.	$950.0 \pm 0.9\,\text{(stat.)} \pm 7.0\,\text{(exp. syst.)} \pm 20.6\,\text{(th. syst.)} \pm 20.9\,\text{(lum.)}\,\text{pb}$
pre-FSR detector acc.	$480.5 \pm 0.4\,\text{(stat.)} \pm 3.5\,\text{(exp. syst.)} \pm 1.0\,\text{(th. syst.)} \pm 10.6\,\text{(lum.)}\,\text{pb}$
post-FSR detector acc.	$462.3 \pm 0.4\,\text{(stat.)} \pm 3.4\,\text{(exp. syst.)} \pm 0.9\,\text{(th. syst.)} \pm 10.2\,\text{(lum.)}\,\text{pb}$
Combined channel	Cross section in the Z-peak region
pre-FSR full acc.	$986.4 \pm 0.6\,\text{(stat.)} \pm 5.9\,\text{(exp. syst.)} \pm 21.7\,\text{(th. syst.)} \pm 21.7\,\text{(lum.)}\,\text{pb}$

The theoretical predictions include leptonic decays of Z bosons with full spin correlations as well as the γ^*/Z interference effects. The effects of lepton pair production in $\gamma\gamma$-initiated processes, where both initial-state protons radiate a photon, are calculated with FEWZ 3.1.b2 [49]. They are particularly important for the high-mass region and are included as additional mass-dependent factors to the main calculation, which takes into account the difference between NLO and LO in the EW correction. The effect rises to approximately 10% in the highest-mass bins. The uncertainties in the theoretical predictions due to the imprecise knowledge of the PDFs are calculated with the LHAGLUE interface to the PDF library LHAPDF, using a reweighting technique with asymmetric uncertainties. The normalization of the spectrum is defined by the number of events in the Z-boson mass peak, so the uncertainty is calculated for the ratio of events in each bin to the number in the Z-boson mass peak.

The result of the measurement is in good agreement with the NNLO theoretical predictions as computed with FEWZ 2.1.1 using CT10. The uncertainty band in Fig. 4 for the theoretical calculation includes the statistical uncertainty from the FEWZ calculation and the 68% confidence level (CL) uncertainty from PDFs combined in quadrature. The effect of the higher-order EW correction computed with FEWZ 3.1.b2 (described above) is included as an additional correction factor and the ratio between data and theoretical prediction is shown in the middle plot. Differences between NLO and NNLO values in theoretical expectations are significant in the low-mass region, as reported in [15]. Although this measurement is sensitive to NNLO effects, it does not provide sufficient sensitivity to distinguish between different PDFs.

In addition to the fully corrected $\text{d}\sigma/\text{d}m$ measurement, we report the cross sections within the detector acceptance ($r^i_{\text{pre-FSR, det}}$) and the post-FSR cross sections ($r^i_{\text{post-FSR}}$, $r^i_{\text{post-FSR, det}}$). The corresponding definitions are

$$r^i_{\text{post-FSR}} = \frac{1}{\Delta m^i} \cdot \left(\frac{N'^i_{\text{u}}}{A^i \epsilon^i \rho'^i} \middle/ \frac{N'^{\text{norm}}_{\text{u}}}{A^{\text{norm}} \epsilon^{\text{norm}} \rho'^{\text{norm}}} \right), \tag{16}$$

$$r^i_{\text{pre-FSR, det}} = \frac{1}{\Delta m^i} \cdot \left(\frac{N^i_{\text{u}}}{\epsilon^i \rho^i} \middle/ \frac{N^{\text{norm}}_{\text{u}}}{\epsilon^{\text{norm}} \rho^{\text{norm}}} \right), \tag{17}$$

$$r^i_{\text{post-FSR, det}} = \frac{1}{\Delta m^i} \cdot \left(\frac{N'^i_{\text{u}}}{\epsilon^i \rho'^i} \middle/ \frac{N'^{\text{norm}}_{\text{u}}}{\epsilon^{\text{norm}} \rho'^{\text{norm}}} \right), \tag{18}$$

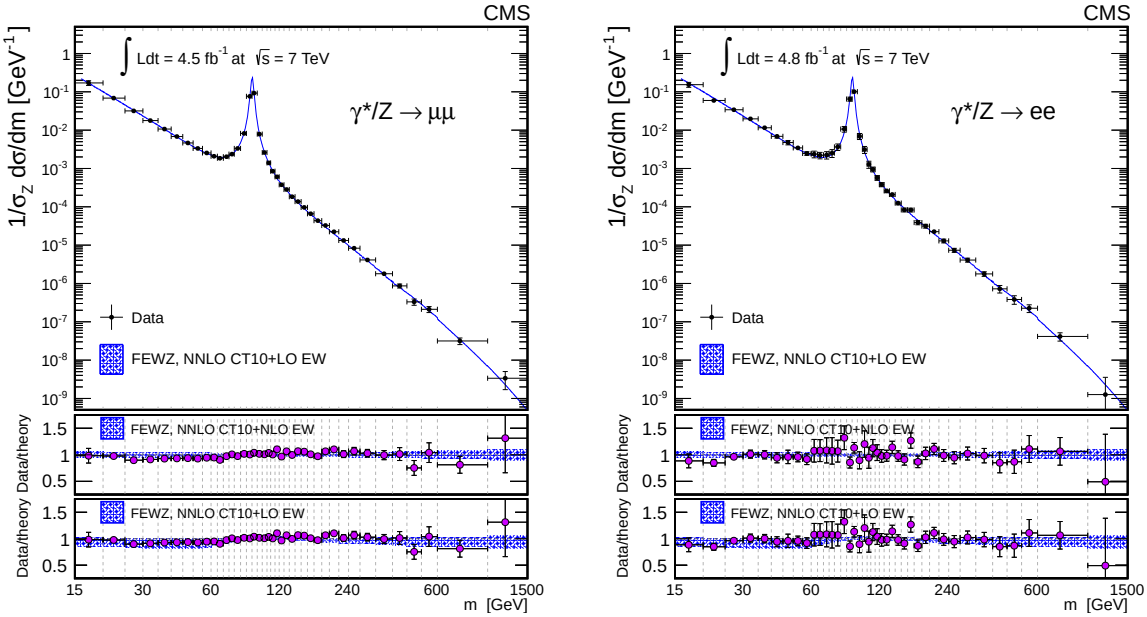

Figure 4: The DY dimuon and dielectron invariant-mass spectra normalized to the Z-boson production cross section $(1/\sigma_Z\,\mathrm{d}\sigma/\mathrm{d}m)$, as measured and as predicted by FEWZ+CT10 NNLO calculations, for the full phase space. The vertical error bars for the measurement indicate the experimental (statistical and systematic) uncertainties summed in quadrature with the theoretical uncertainty resulting from the model-dependent kinematic distributions inside each bin. The shaded uncertainty band for the theoretical calculation includes the statistical uncertainty from the FEWZ calculation and the 68% confidence level uncertainty from PDFs combined in quadrature. The effect of NLO EW correction including $\gamma\gamma$-initiated processes (LO EW correction only) is shown in the middle (bottom) plot for each channel. The data point abscissas are computed according to Eq. (6) in Ref. [48].

where the quantities labeled with primes do not contain the FSR correction. All the r shape measurements for dimuons are summarized in Table 7. The corresponding results for the dielectron channel can be found in Table 8.

The measurements in the two channels are combined using the procedure defined in Ref. [50], which provides a full covariance matrix for the uncertainties. Given the cross section measurements in the dimuon and dielectron channels, and their symmetric and positive-definite covariance matrices, the estimates of the true cross section values are found as unbiased linear combinations of the input measurements having a minimum variance.

The uncertainties are considered to be uncorrelated between the two analyses. Exceptions are the modeling uncertainty, which is 100% correlated between channels, and the uncertainty in the acceptance, which originates mainly from the PDFs. The acceptance is almost identical between the two channels and the differences in uncertainties between them are negligible. Thus, when combining the measurements we add the uncertainty in the acceptance (in quadrature) to the total uncertainty after the combination is done. The acceptance uncertainty does not include correlations between analysis bins.

Figure 5 shows the DY cross section measurement in the combined dimuon and dielectron channels normalized to the Z-boson mass peak region with the FSR effect taken into account. The corresponding results are summarized in Table 9.

Table 7: The DY cross section measurements for the muon channel normalized to the Z-peak region, pre- and post-FSR, as measured in the full acceptance and for the CMS detector acceptance. The uncertainty indicates the experimental (statistical and systematic) uncertainties summed in quadrature with the theoretical uncertainty resulting from the model-dependent kinematic distributions inside each bin. The results presented are in GeV^{-1} units.

m (GeV)	$r^i_{\text{pre-FSR}}$	$r^i_{\text{post-FSR}}$	$r^i_{\text{pre-FSR, det}}$	$r^i_{\text{post-FSR, det}}$
15–20	$(17.1\pm1.7)\times10^{-2}$	$(15.9\pm1.6)\times10^{-2}$	$(325.2\pm7.7)\times10^{-5}$	$(303.2\pm7.0)\times10^{-5}$
20–25	$(68.5\pm3.5)\times10^{-3}$	$(66.6\pm3.4)\times10^{-3}$	$(44.8\pm1.1)\times10^{-4}$	$(44.0\pm1.1)\times10^{-4}$
25–30	$(31.8\pm1.6)\times10^{-3}$	$(31.5\pm1.6)\times10^{-3}$	$(92.2\pm3.5)\times10^{-4}$	$(91.3\pm3.4)\times10^{-4}$
30–35	$(177.7\pm6.5)\times10^{-4}$	$(177.0\pm6.5)\times10^{-4}$	$(87.0\pm2.2)\times10^{-4}$	$(86.2\pm2.1)\times10^{-4}$
35–40	$(106.8\pm3.5)\times10^{-4}$	$(108.1\pm3.5)\times10^{-4}$	$(63.6\pm1.2)\times10^{-4}$	$(63.6\pm1.2)\times10^{-4}$
40–45	$(68.2\pm2.0)\times10^{-4}$	$(70.9\pm2.1)\times10^{-4}$	$(452.4\pm7.4)\times10^{-5}$	$(467.6\pm7.5)\times10^{-5}$
45–50	$(46.3\pm1.4)\times10^{-4}$	$(50.5\pm1.5)\times10^{-4}$	$(330.3\pm5.4)\times10^{-5}$	$(364.3\pm5.8)\times10^{-5}$
50–55	$(333.5\pm9.8)\times10^{-5}$	$(39.6\pm1.1)\times10^{-4}$	$(246.0\pm4.1)\times10^{-5}$	$(301.8\pm4.7)\times10^{-5}$
55–60	$(254.1\pm7.5)\times10^{-5}$	$(328.0\pm9.4)\times10^{-5}$	$(205.5\pm3.7)\times10^{-5}$	$(275.5\pm4.5)\times10^{-5}$
60–64	$(208.4\pm6.3)\times10^{-5}$	$(309.0\pm8.8)\times10^{-5}$	$(173.9\pm3.5)\times10^{-5}$	$(270.6\pm4.8)\times10^{-5}$
64–68	$(184.9\pm5.7)\times10^{-5}$	$(316.0\pm9.2)\times10^{-5}$	$(159.8\pm3.5)\times10^{-5}$	$(287.7\pm5.5)\times10^{-5}$
68–72	$(202.6\pm6.2)\times10^{-5}$	$(36.0\pm1.0)\times10^{-4}$	$(180.5\pm3.9)\times10^{-5}$	$(335.7\pm6.3)\times10^{-5}$
72–76	$(236.5\pm7.2)\times10^{-5}$	$(44.7\pm1.3)\times10^{-4}$	$(217.3\pm4.7)\times10^{-5}$	$(426.2\pm7.8)\times10^{-5}$
76–81	$(333.1\pm9.8)\times10^{-5}$	$(64.1\pm1.8)\times10^{-4}$	$(315.3\pm6.4)\times10^{-5}$	$(62.2\pm1.1)\times10^{-4}$
81–86	$(82.2\pm2.5)\times10^{-4}$	$(134.4\pm4.0)\times10^{-4}$	$(80.4\pm1.7)\times10^{-4}$	$(132.7\pm2.7)\times10^{-4}$
86–91	$(76.2\pm2.5)\times10^{-3}$	$(78.4\pm2.6)\times10^{-3}$	$(76.2\pm1.9)\times10^{-3}$	$(78.5\pm1.9)\times10^{-3}$
91–96	$(92.5\pm3.2)\times10^{-3}$	$(78.6\pm2.8)\times10^{-3}$	$(93.3\pm2.6)\times10^{-3}$	$(79.3\pm2.2)\times10^{-3}$
96–101	$(78.8\pm2.7)\times10^{-4}$	$(70.0\pm2.4)\times10^{-4}$	$(80.5\pm2.2)\times10^{-4}$	$(71.6\pm1.9)\times10^{-4}$
101–106	$(260.8\pm8.2)\times10^{-5}$	$(237.5\pm7.4)\times10^{-5}$	$(269.4\pm6.4)\times10^{-5}$	$(245.7\pm5.8)\times10^{-5}$
106–110	$(139.9\pm4.4)\times10^{-5}$	$(129.2\pm4.0)\times10^{-5}$	$(145.2\pm3.5)\times10^{-5}$	$(134.3\pm3.2)\times10^{-5}$
110–115	$(84.9\pm2.6)\times10^{-5}$	$(79.8\pm2.5)\times10^{-5}$	$(89.5\pm2.2)\times10^{-5}$	$(84.4\pm2.0)\times10^{-5}$
115–120	$(60.5\pm2.0)\times10^{-5}$	$(56.5\pm1.8)\times10^{-5}$	$(64.0\pm1.7)\times10^{-5}$	$(59.8\pm1.6)\times10^{-5}$
120–126	$(37.5\pm1.3)\times10^{-5}$	$(35.7\pm1.2)\times10^{-5}$	$(40.3\pm1.2)\times10^{-5}$	$(38.4\pm1.1)\times10^{-5}$
126–133	$(282.8\pm9.6)\times10^{-6}$	$(265.4\pm9.0)\times10^{-6}$	$(305.9\pm9.1)\times10^{-6}$	$(287.4\pm8.5)\times10^{-6}$
133–141	$(183.4\pm6.8)\times10^{-6}$	$(174.2\pm6.4)\times10^{-6}$	$(200.6\pm6.7)\times10^{-6}$	$(191.7\pm6.4)\times10^{-6}$
141–150	$(136.8\pm5.4)\times10^{-6}$	$(130.5\pm5.1)\times10^{-6}$	$(153.0\pm5.5)\times10^{-6}$	$(146.2\pm5.3)\times10^{-6}$
150–160	$(96.5\pm4.2)\times10^{-6}$	$(91.7\pm4.0)\times10^{-6}$	$(107.4\pm4.4)\times10^{-6}$	$(102.8\pm4.2)\times10^{-6}$
160–171	$(65.8\pm3.2)\times10^{-6}$	$(63.2\pm3.1)\times10^{-6}$	$(75.6\pm3.5)\times10^{-6}$	$(72.7\pm3.4)\times10^{-6}$
171–185	$(43.5\pm2.2)\times10^{-6}$	$(41.3\pm2.1)\times10^{-6}$	$(50.9\pm2.6)\times10^{-6}$	$(48.6\pm2.4)\times10^{-6}$
185–200	$(32.6\pm1.8)\times10^{-6}$	$(31.2\pm1.7)\times10^{-6}$	$(39.2\pm2.1)\times10^{-6}$	$(37.6\pm2.0)\times10^{-6}$
200–220	$(22.3\pm1.2)\times10^{-6}$	$(20.6\pm1.1)\times10^{-6}$	$(27.0\pm1.4)\times10^{-6}$	$(25.0\pm1.2)\times10^{-6}$
220–243	$(132.4\pm8.3)\times10^{-7}$	$(129.5\pm8.1)\times10^{-7}$	$(164.2\pm9.7)\times10^{-7}$	$(161.0\pm9.5)\times10^{-7}$
243–273	$(83.1\pm5.4)\times10^{-7}$	$(78.8\pm5.1)\times10^{-7}$	$(108.0\pm6.7)\times10^{-7}$	$(102.5\pm6.4)\times10^{-7}$
273–320	$(41.1\pm2.8)\times10^{-7}$	$(38.5\pm2.6)\times10^{-7}$	$(55.3\pm3.6)\times10^{-7}$	$(52.0\pm3.4)\times10^{-7}$
320–380	$(17.9\pm1.5)\times10^{-7}$	$(17.0\pm1.4)\times10^{-7}$	$(25.5\pm2.1)\times10^{-7}$	$(24.2\pm2.0)\times10^{-7}$
380–440	$(8.6\pm1.0)\times10^{-7}$	$(77.5\pm9.2)\times10^{-8}$	$(12.8\pm1.5)\times10^{-7}$	$(11.5\pm1.3)\times10^{-7}$
440–510	$(33.1\pm6.1)\times10^{-8}$	$(33.3\pm6.2)\times10^{-8}$	$(49.3\pm9.1)\times10^{-8}$	$(49.9\pm9.2)\times10^{-8}$
510–600	$(21.2\pm3.8)\times10^{-8}$	$(20.0\pm3.5)\times10^{-8}$	$(33.0\pm5.8)\times10^{-8}$	$(31.2\pm5.5)\times10^{-8}$
600–1000	$(31.6\pm6.1)\times10^{-9}$	$(32.8\pm6.4)\times10^{-9}$	$(51.4\pm9.9)\times10^{-9}$	$(5.3\pm1.0)\times10^{-8}$
1000–1500	$(3.4\pm1.7)\times10^{-9}$	$(2.9\pm1.4)\times10^{-9}$	$(5.8\pm2.9)\times10^{-9}$	$(5.0\pm2.4)\times10^{-9}$

Table 8: The DY cross section measurements for the electron channel normalized to the Z-peak region, pre- and post-FSR, as measured in the full acceptance and for the CMS detector acceptance. The uncertainty indicates the experimental (statistical and systematic) uncertainties summed in quadrature with the theoretical uncertainty resulting from the model-dependent kinematic distributions inside each bin. The results presented are in GeV^{-1} units.

m (GeV)	$r^i_{\text{pre-FSR}}$	$r^i_{\text{post-FSR}}$	$r^i_{\text{pre-FSR, det}}$	$r^i_{\text{post-FSR, det}}$
15–20	$(15.4\pm1.7)\times10^{-2}$	$(14.9\pm1.6)\times10^{-2}$	$(145.4\pm6.5)\times10^{-5}$	$(140.3\pm5.9)\times10^{-5}$
20–25	$(59.5\pm4.2)\times10^{-3}$	$(58.5\pm3.9)\times10^{-3}$	$(105.2\pm6.2)\times10^{-5}$	$(103.3\pm5.6)\times10^{-5}$
25–30	$(34.0\pm2.0)\times10^{-3}$	$(33.4\pm1.8)\times10^{-3}$	$(131.5\pm6.7)\times10^{-5}$	$(128.5\pm5.8)\times10^{-5}$
30–35	$(19.7\pm1.5)\times10^{-3}$	$(19.4\pm1.3)\times10^{-3}$	$(23.9\pm1.7)\times10^{-4}$	$(23.7\pm1.5)\times10^{-4}$
35–40	$(115.3\pm9.1)\times10^{-4}$	$(116.6\pm7.8)\times10^{-4}$	$(33.2\pm2.5)\times10^{-4}$	$(33.3\pm2.1)\times10^{-4}$
40–45	$(68.9\pm6.9)\times10^{-4}$	$(74.1\pm5.8)\times10^{-4}$	$(33.6\pm3.2)\times10^{-4}$	$(35.6\pm2.7)\times10^{-4}$
45–50	$(47.5\pm6.3)\times10^{-4}$	$(55.1\pm5.3)\times10^{-4}$	$(28.6\pm3.7)\times10^{-4}$	$(34.1\pm3.2)\times10^{-4}$
50–55	$(34.4\pm3.3)\times10^{-4}$	$(44.8\pm2.7)\times10^{-4}$	$(23.3\pm2.2)\times10^{-4}$	$(32.5\pm1.8)\times10^{-4}$
55–60	$(24.7\pm2.7)\times10^{-4}$	$(39.4\pm2.2)\times10^{-4}$	$(18.2\pm2.0)\times10^{-4}$	$(31.7\pm1.6)\times10^{-4}$
60–64	$(23.6\pm4.7)\times10^{-4}$	$(41.9\pm3.7)\times10^{-4}$	$(18.7\pm3.9)\times10^{-4}$	$(36.1\pm3.1)\times10^{-4}$
64–68	$(22.1\pm4.2)\times10^{-4}$	$(45.5\pm3.3)\times10^{-4}$	$(18.0\pm3.6)\times10^{-4}$	$(40.7\pm2.8)\times10^{-4}$
68–72	$(22.5\pm4.9)\times10^{-4}$	$(52.8\pm3.7)\times10^{-4}$	$(19.7\pm4.4)\times10^{-4}$	$(49.3\pm3.3)\times10^{-4}$
72–76	$(25.2\pm5.9)\times10^{-4}$	$(65.3\pm4.3)\times10^{-4}$	$(22.7\pm5.3)\times10^{-4}$	$(62.3\pm4.0)\times10^{-4}$
76–81	$(36.5\pm7.0)\times10^{-4}$	$(95.3\pm4.9)\times10^{-4}$	$(34.4\pm6.5)\times10^{-4}$	$(92.8\pm4.4)\times10^{-4}$
81–86	$(10.7\pm1.8)\times10^{-3}$	$(19.2\pm1.3)\times10^{-3}$	$(10.4\pm1.7)\times10^{-3}$	$(19.0\pm1.2)\times10^{-3}$
86–91	$(64.8\pm7.8)\times10^{-3}$	$(70.3\pm6.4)\times10^{-3}$	$(64.8\pm7.7)\times10^{-3}$	$(70.6\pm6.3)\times10^{-3}$
91–96	$(100.8\pm8.8)\times10^{-3}$	$(74.0\pm6.4)\times10^{-3}$	$(101.9\pm8.8)\times10^{-3}$	$(75.1\pm6.4)\times10^{-3}$
96–101	$(6.9\pm1.2)\times10^{-3}$	$(56.8\pm9.3)\times10^{-4}$	$(7.1\pm1.3)\times10^{-3}$	$(58.8\pm9.5)\times10^{-4}$
101–106	$(31.1\pm6.4)\times10^{-4}$	$(25.7\pm4.8)\times10^{-4}$	$(32.5\pm6.7)\times10^{-4}$	$(26.9\pm5.0)\times10^{-4}$
106–110	$(12.8\pm2.7)\times10^{-4}$	$(11.3\pm2.0)\times10^{-4}$	$(13.5\pm2.8)\times10^{-4}$	$(12.1\pm2.1)\times10^{-4}$
110–115	$(9.5\pm1.4)\times10^{-4}$	$(8.2\pm1.0)\times10^{-4}$	$(10.1\pm1.5)\times10^{-4}$	$(8.8\pm1.1)\times10^{-4}$
115–120	$(57.1\pm8.2)\times10^{-5}$	$(50.9\pm6.1)\times10^{-5}$	$(61.7\pm8.7)\times10^{-5}$	$(55.2\pm6.5)\times10^{-5}$
120–126	$(38.0\pm4.6)\times10^{-5}$	$(34.1\pm3.5)\times10^{-5}$	$(41.2\pm4.9)\times10^{-5}$	$(37.3\pm3.7)\times10^{-5}$
126–133	$(26.1\pm2.7)\times10^{-5}$	$(23.9\pm2.1)\times10^{-5}$	$(29.1\pm3.0)\times10^{-5}$	$(26.7\pm2.3)\times10^{-5}$
133–141	$(21.0\pm2.1)\times10^{-5}$	$(18.7\pm1.6)\times10^{-5}$	$(23.4\pm2.3)\times10^{-5}$	$(20.8\pm1.8)\times10^{-5}$
141–150	$(12.5\pm1.3)\times10^{-5}$	$(115.3\pm9.9)\times10^{-6}$	$(14.3\pm1.4)\times10^{-5}$	$(13.3\pm1.1)\times10^{-5}$
150–160	$(83.1\pm9.6)\times10^{-6}$	$(80.2\pm7.4)\times10^{-6}$	$(9.6\pm1.1)\times10^{-5}$	$(93.2\pm8.4)\times10^{-6}$
160–171	$(82.7\pm9.4)\times10^{-6}$	$(71.9\pm7.2)\times10^{-6}$	$(9.6\pm1.1)\times10^{-5}$	$(84.0\pm8.3)\times10^{-6}$
171–185	$(38.8\pm4.9)\times10^{-6}$	$(37.1\pm3.8)\times10^{-6}$	$(46.6\pm5.8)\times10^{-6}$	$(45.1\pm4.6)\times10^{-6}$
185–200	$(31.4\pm3.5)\times10^{-6}$	$(29.4\pm2.8)\times10^{-6}$	$(38.4\pm4.3)\times10^{-6}$	$(36.8\pm3.4)\times10^{-6}$
200–220	$(22.5\pm2.1)\times10^{-6}$	$(20.3\pm1.7)\times10^{-6}$	$(28.8\pm2.6)\times10^{-6}$	$(25.7\pm2.1)\times10^{-6}$
220–243	$(12.9\pm1.4)\times10^{-6}$	$(12.2\pm1.2)\times10^{-6}$	$(16.5\pm1.8)\times10^{-6}$	$(15.8\pm1.5)\times10^{-6}$
243–273	$(73.6\pm8.8)\times10^{-7}$	$(67.2\pm7.1)\times10^{-7}$	$(9.6\pm1.2)\times10^{-6}$	$(90.1\pm9.3)\times10^{-7}$
273–320	$(40.8\pm4.8)\times10^{-7}$	$(37.3\pm4.0)\times10^{-7}$	$(56.2\pm6.6)\times10^{-7}$	$(51.0\pm5.3)\times10^{-7}$
320–380	$(17.7\pm2.4)\times10^{-7}$	$(15.7\pm2.0)\times10^{-7}$	$(26.4\pm3.6)\times10^{-7}$	$(23.3\pm2.9)\times10^{-7}$
380–440	$(7.2\pm1.6)\times10^{-7}$	$(6.7\pm1.3)\times10^{-7}$	$(11.3\pm2.5)\times10^{-7}$	$(10.5\pm2.0)\times10^{-7}$
440–510	$(38.2\pm9.6)\times10^{-8}$	$(36.0\pm8.0)\times10^{-8}$	$(6.0\pm1.5)\times10^{-7}$	$(5.7\pm1.2)\times10^{-7}$
510–600	$(22.6\pm5.1)\times10^{-8}$	$(20.2\pm4.2)\times10^{-8}$	$(35.9\pm8.1)\times10^{-8}$	$(32.2\pm6.7)\times10^{-8}$
600–1000	$(4.1\pm1.0)\times10^{-8}$	$(36.8\pm8.9)\times10^{-9}$	$(6.8\pm1.7)\times10^{-8}$	$(6.1\pm1.5)\times10^{-8}$
1000–1500	$(1.3\pm2.3)\times10^{-9}$	$(1.1\pm2.0)\times10^{-9}$	$(2.2\pm4.0)\times10^{-9}$	$(1.9\pm3.5)\times10^{-9}$

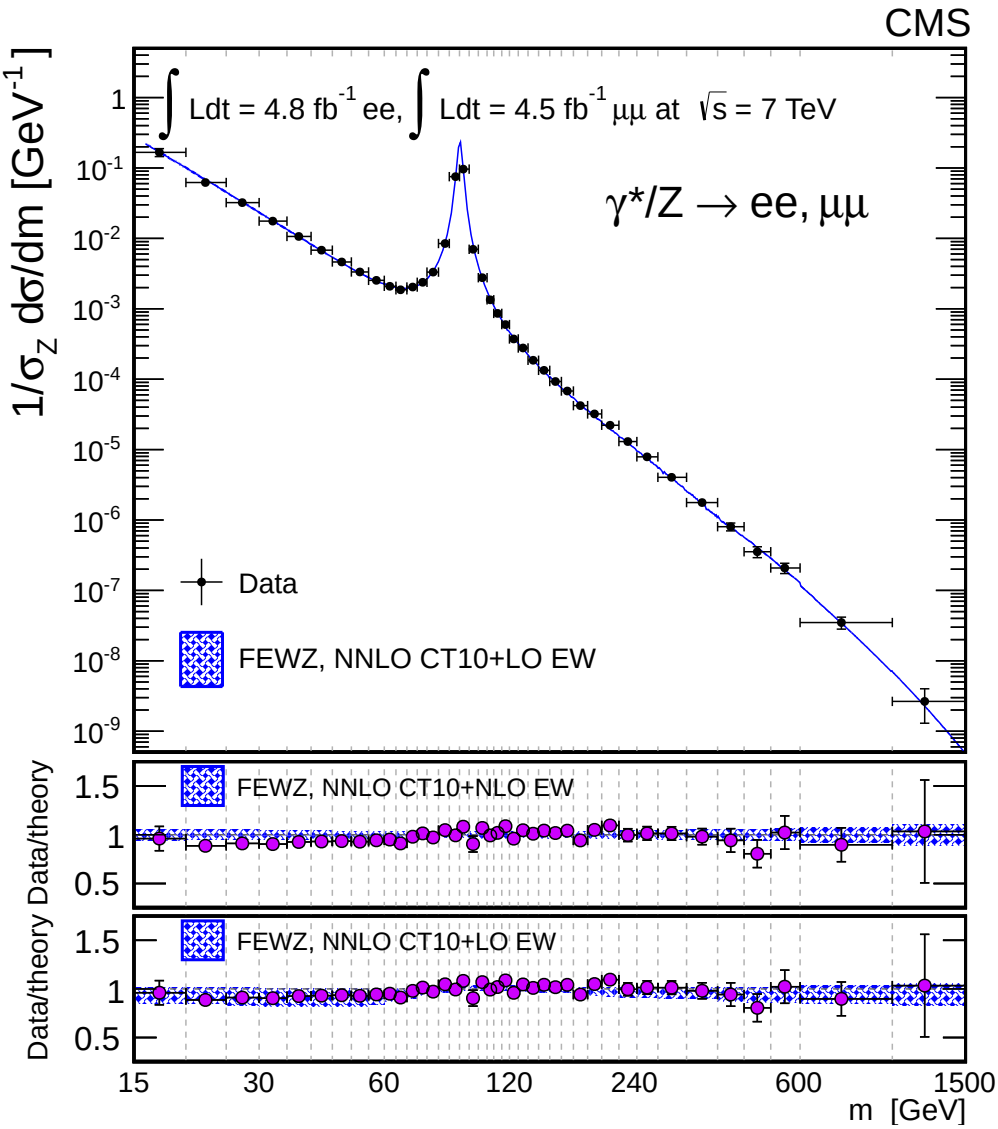

Figure 5: Combined DY differential cross section measurement in the dimuon and dielectron channels normalized to the Z-peak region with the FSR effect taken into account. The data point abscissas are computed according to Eq. (6) in Ref. [48]. Including the correlations between the two channels, the normalized χ^2 calculated with total uncertainties on the combined results is 1.1 between data and the theoretical expectation, with 40 degrees of freedom. The corresponding χ^2 probability is 36.8%.

5.2 Double-differential cross section $\mathrm{d}^2\sigma/\mathrm{d}m\,\mathrm{d}|y|$ measurement

The result of the double-differential cross section measurement for the dimuon channel is presented as the following ratio:

$$R^{ij}_{\text{pre-FSR, det}} = \frac{N^{ij}_{\mathrm{u}}}{\epsilon^{ij}\rho^{ij}} \Bigg/ \frac{N^{\text{norm}}_{\mathrm{u}}}{\epsilon^{\text{norm}}\rho^{\text{norm}}} \,. \tag{19}$$

The quantities N^{ij}_{u}, ϵ^{ij}, ρ^{ij} are defined in a given bin $(i,\ j)$, with i corresponding to the binning in invariant mass, and j corresponding to the binning in absolute rapidity; $N^{\text{norm}}_{\mathrm{u}}$, ϵ^{norm}, and

Table 9: The DY pre-FSR cross section measurements for the combined dimuon and dielectron channels normalized to the Z-peak region in the full acceptance. The results presented are in GeV^{-1} units.

m (GeV)	$r^i_{\text{pre-FSR}}$	m (GeV)	$r^i_{\text{pre-FSR}}$	m (GeV)	$r^i_{\text{pre-FSR}}$
15–20	$(16.7\pm1.4)\times10^{-2}$	81–86	$(84.5\pm4.5)\times10^{-4}$	171–185	$(42.1\pm2.4)\times10^{-6}$
20–25	$(62.2\pm2.9)\times10^{-3}$	86–91	$(75.3\pm2.7)\times10^{-3}$	185–200	$(32.1\pm1.9)\times10^{-6}$
25–30	$(32.2\pm1.2)\times10^{-3}$	91–96	$(96.4\pm3.3)\times10^{-3}$	200–220	$(22.2\pm1.2)\times10^{-6}$
30–35	$(175.9\pm4.7)\times10^{-4}$	96–101	$(70.0\pm6.3)\times10^{-4}$	220–243	$(130.1\pm8.4)\times10^{-7}$
35–40	$(106.5\pm2.8)\times10^{-4}$	101–106	$(27.6\pm1.5)\times10^{-4}$	243–273	$(78.9\pm5.3)\times10^{-7}$
40–45	$(68.0\pm1.9)\times10^{-4}$	106–110	$(134.1\pm5.9)\times10^{-5}$	273–320	$(40.4\pm2.7)\times10^{-7}$
45–50	$(46.2\pm1.2)\times10^{-4}$	110–115	$(86.0\pm3.2)\times10^{-5}$	320–380	$(17.7\pm1.5)\times10^{-7}$
50–55	$(33.3\pm1.1)\times10^{-4}$	115–120	$(59.7\pm2.1)\times10^{-5}$	380–440	$(8.0\pm1.0)\times10^{-7}$
55–60	$(253.5\pm7.7)\times10^{-5}$	120–126	$(37.3\pm1.4)\times10^{-5}$	440–510	$(35.4\pm6.2)\times10^{-8}$
60–64	$(208.7\pm6.2)\times10^{-5}$	126–133	$(27.8\pm1.0)\times10^{-5}$	510–600	$(20.8\pm3.3)\times10^{-8}$
64–68	$(186.2\pm6.2)\times10^{-5}$	133–141	$(185.7\pm7.7)\times10^{-6}$	600–1000	$(34.9\pm6.7)\times10^{-9}$
68–72	$(203.7\pm6.7)\times10^{-5}$	141–150	$(133.6\pm5.8)\times10^{-6}$	1000–1500	$(2.7\pm1.4)\times10^{-9}$
72–76	$(237.9\pm8.2)\times10^{-5}$	150–160	$(92.7\pm4.6)\times10^{-6}$		
76–81	$(33.2\pm1.1)\times10^{-4}$	160–171	$(67.9\pm3.7)\times10^{-6}$		

ρ^{norm} refer to the Z-peak region within $|y| < 2.4$ in the muon acceptance. The normalization factors from our measurement and each theoretical prediction from various PDF sets are available in Table 10. As shown in this table, the normalization factors between data and theoretical predictions are in good agreement within the uncertainty, except for JR09. These results are normalized to the dimuon absolute rapidity bin widths, Δy^j, defining the shape $r^{ij} = R^{ij}/(\Delta y^j)$. An acceptance correction to the full phase space would not increase the sensitivity to PDFs. Therefore, this measurement is performed within the detector acceptance in order to reduce model dependence. We use the NNLO reweighted POWHEG sample in this measurement, which is discussed in Section 3. This sample is used to derive the selection efficiency and to produce response matrices for detector resolution and FSR corrections.

Table 10: Normalization factors for the measurement in the Z-peak region ($60 < m < 120\,\mathrm{GeV}$ and $|y| < 2.4$) and the detector acceptance for the dimuon channel. The row for the data corresponds to the pre-FSR, detector acceptance result in Table 6 for the muon channel. The uncertainty in the theoretical cross sections indicates the statistical calculation uncertainty and PDF uncertainty in FEWZ.

	Cross section in the Z-peak region in the detector acceptance ($60 < m < 120\,\mathrm{GeV}$, $\lvert y\rvert < 2.4$)
Data	$524.7 \pm 0.4\,(\text{stat.}) \pm 5.1\,(\text{exp. syst.}) \pm 1.2\,(\text{th. syst.}) \pm 11.5\,(\text{lum.})\,\text{pb}$
CT10 NNLO	$534.29 \pm 0.36\,(\text{stat}) \pm 16.60\,(\text{PDF})\,\text{pb}$
NNPDF2.1 NNLO	$524.76 \pm 0.68\,(\text{stat}) \pm 6.38\,(\text{PDF})\,\text{pb}$
MSTW2008 NNLO	$524.02 \pm 0.38\,(\text{stat.}) \pm 17.46\,(\text{PDF})\,\text{pb}$
JR09 NNLO	$485.97 \pm 0.36\,(\text{stat.}) \pm 11.78\,(\text{PDF})\,\text{pb}$
ABKM09 NNLO	$534.69 \pm 0.43\,(\text{stat.}) \pm 9.30\,(\text{PDF})\,\text{pb}$
HERAPDF15 NNLO	$531.92 \pm 0.23\,(\text{stat.}) \pm 6.25\,(\text{PDF})\,\text{pb}$

Figure 6 shows the results for the double-differential cross section. The results are compared to the FEWZ+CT10 NLO PDF and FEWZ+CT10 NNLO PDF theoretical calculations. The results of

the measurement are in a better agreement with CT10 NNLO predictions than with CT10 NLO ones. The CT10 PDF set is a general-purpose NLO PDF set with 52 eigenvectors that uses a variable strong coupling $\alpha_s(M_Z)$ in the range 0.116–0.120 and 0.112–0.127. The CT10 (NNLO) is also a general purpose PDF set. It includes a part of the data sample for the D0 W-charge asymmetry measurement [10] that is not included in the CT10 NLO fit. The W-charge asymmetry data primarily modifies the slope of the ratio $d(x, Q^2)/u(x, Q^2)$ at large x. The CT10 (NNLO) PDF set uses a variable strong coupling $\alpha_s(M_Z)$ in the range of 0.116–0.120 and 0.110–0.130. We have chosen CT10 (NLO) and CT10 (NNLO) to compare with our measurement in Fig. 6 because we have used the CT10 (NLO) for the POWHEG MC signal sample. The uncertainty bands in the theoretical expectations include the statistical and the PDF uncertainties from the FEWZ calculations summed in quadrature (shaded band). The statistical uncertainty (solid band) is smaller than the PDF uncertainty and the latter is the dominant uncertainty in the FEWZ calculations. In general, the PDF uncertainty assignment is different for each PDF set. For instance, CT10 (NLO) and CT10 (NNLO) PDF uncertainties correspond to a 90% CL, so, to get a consistent comparison to other PDF sets the uncertainties are scaled to the 68% CL.

In the low-mass region and the Z-peak region, we observe good agreement between data and theory. The NNLO effects are more significant in the low-mass region. The corrections for the $\gamma\gamma$-initiated processes calculated with FEWZ 3.1.b2 are negligible in the double-differential cross section measurement, because the effects are approximately constant over the investigated rapidity range and statistical fluctuations or other systematic uncertainties are much larger across the invariant-mass range of the measurement.

In order to assess the sensitivity of the double-differential cross section measurement to the PDF uncertainties, we perform a comparison with the theoretical expectations calculated with various PDF sets. Figure 7 shows the comparison with currently available NNLO PDFs, most of which are from the pre-LHC era: CT10, CT10W, NNPDF2.1, HERAPDF15, MSTW2008, JR09, and ABKM09.

As seen in Fig. 7, the predictions of various existing PDF sets are rather different, especially in the low- and high-mass regions. Given the uncertainties, the measurements provide sufficient sensitivity to different PDFs and can be used to calculate a new generation of PDFs. The uncertainty bands in the theoretical expectations in the figure indicate the statistical uncertainty from the FEWZ calculation. Table 10 shows the statistical and the PDF uncertainties separately.

In the low-mass region (20–45 GeV), we observe that the values of the double-differential cross section calculated with the NNPDF2.1 are higher than the values calculated with other PDF sets. The NNPDF2.1 calculation shows good agreement with the measurement result in the 20–30 GeV region, but it deviates from the measurement in the 30–45 GeV region by about 10%. In the peak region, all predictions are relatively close to each other and agree well with the measurements. At high mass the JR09 PDF calculation predicts significantly larger values than other PDF sets. The statistical uncertainties in the measurements for $m > 200$ GeV are of the order of the spread in the theoretical predictions.

In addition to the $r^{ij}_{\text{pre-FSR, det}}$ measurement we report the cross section without FSR correction, $r^{ij}_{\text{post-FSR, det}}$. The corresponding definition is

$$r^{ij}_{\text{post-FSR, det}} = \frac{1}{\Delta y^j} \cdot \left(\frac{N_{\text{u}}^{\prime ij}}{\epsilon^{ij}\rho^{\prime ij}} \middle/ \frac{N_{\text{u}}^{\prime \text{norm}}}{\epsilon^{\text{norm}}\rho^{\prime \text{norm}}} \right), \tag{20}$$

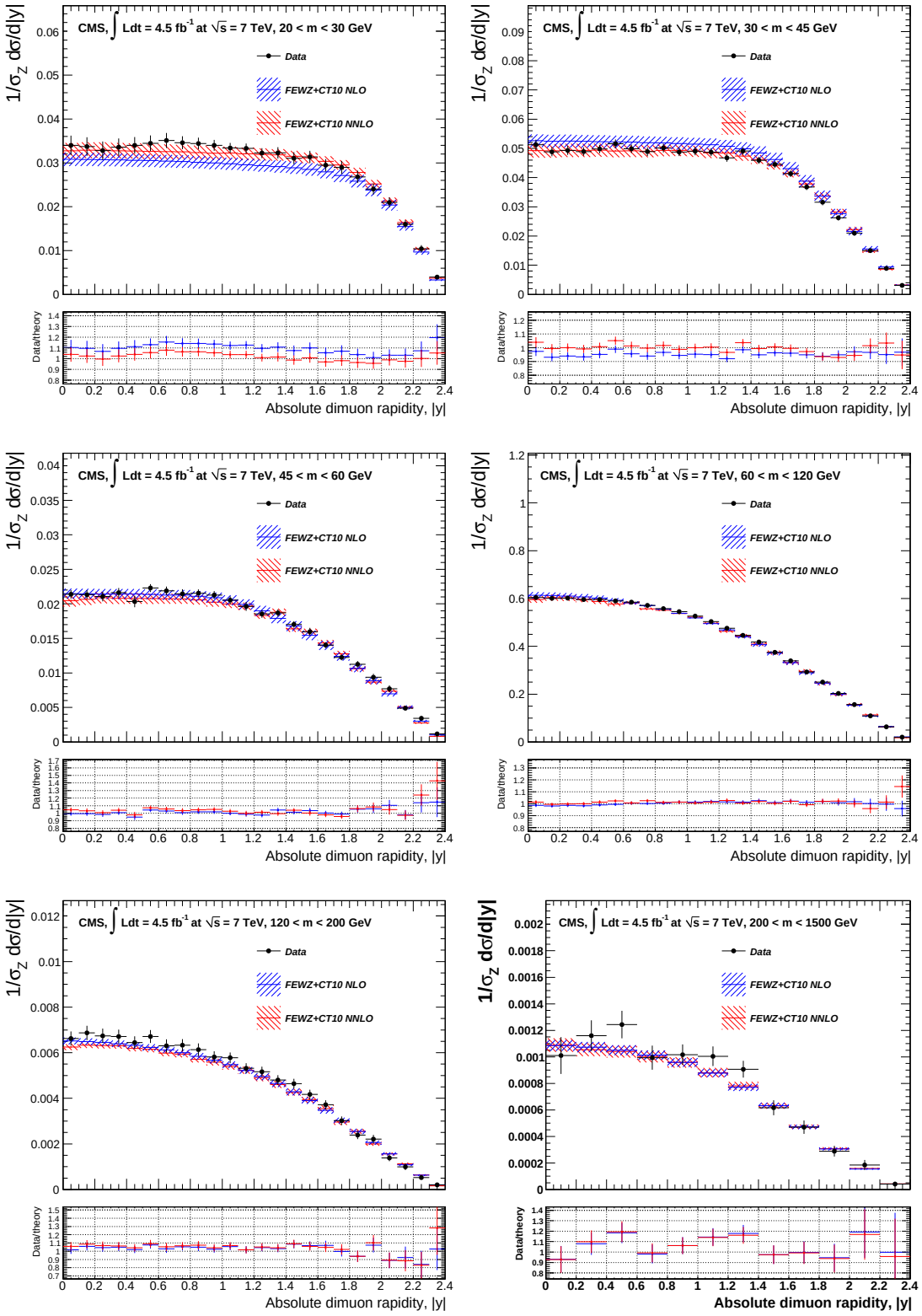

Figure 6: The DY rapidity spectrum normalized to the Z-peak region $(1/\sigma_Z\,\mathrm{d}^2\sigma/d|y|)$, plotted for different mass regions within the detector acceptance, as measured and as predicted by NLO FEWZ+CT10 PDF and NNLO FEWZ+CT10 PDF calculations. There are six mass bins between 20 and 1500 GeV, from left to right and from top to bottom. The uncertainty bands in the theoretical predictions combine the statistical and the PDF uncertainties (shaded bands). The statistical component is negligible. The smaller plots show the ratio of data to theoretical expectation.

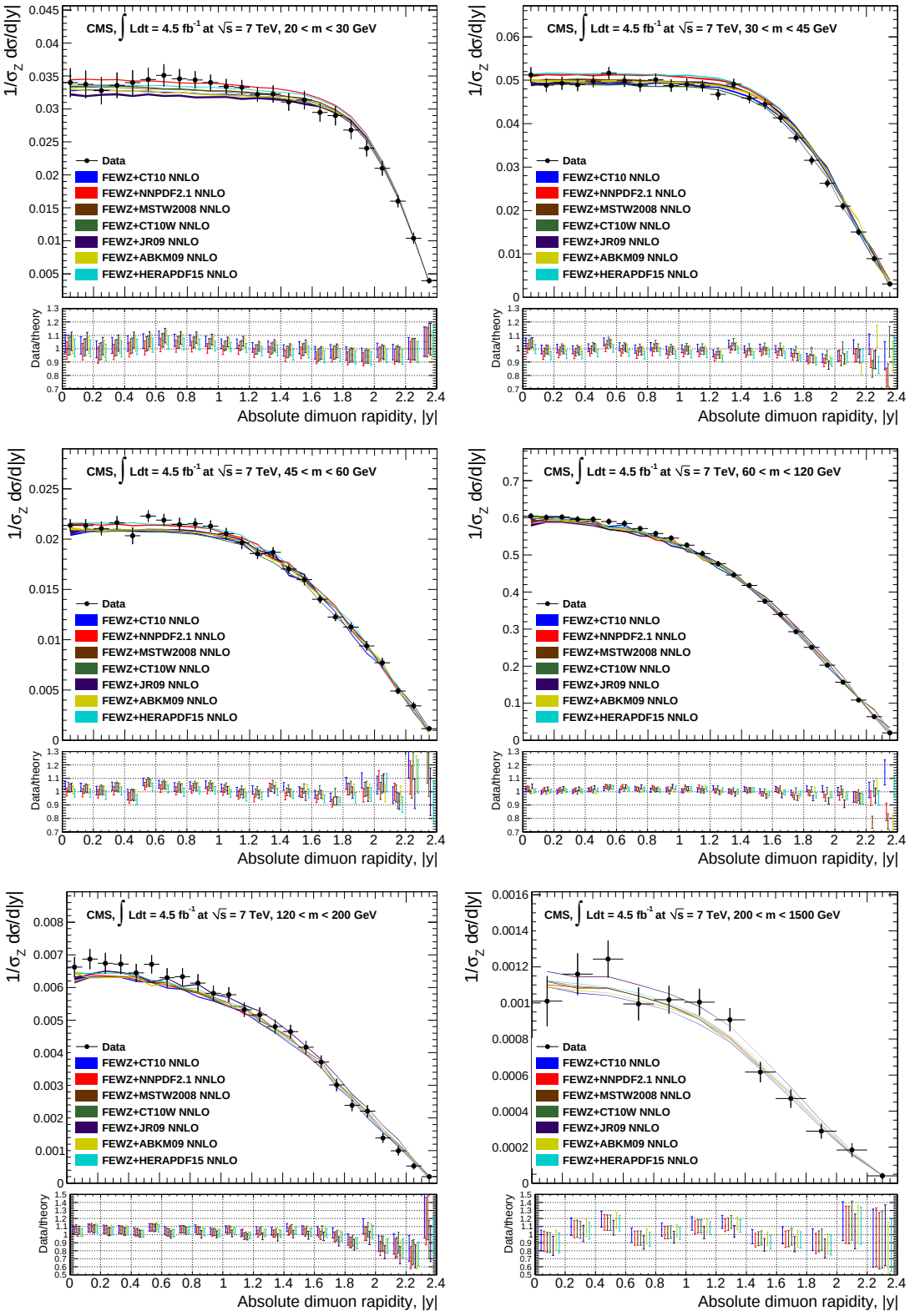

Figure 7: The DY rapidity spectrum normalized to the Z-peak region $(1/\sigma_Z\, d^2\sigma/d|y|)$, compared to theoretical expectations using various PDF sets. The uncertainty bands in the theoretical predictions indicate the statistical uncertainty only. The smaller plots show the ratio of data to theoretical expectation. The error bars include the experimental uncertainty in the data and statistical uncertainty in the theoretical expectation, combined quadratically.

Table 11: The DY dimuon rapidity spectrum within the detector acceptance, normalized to the Z-peak region, $r_{\text{pre-FSR, det}} = (1/\sigma_Z \, \mathrm{d}\sigma/\mathrm{d}|y|)$, tabulated for different mass regions. The rows are the dimuon rapidity bins and the columns are mass bins (in GeV). The uncertainties are the total experimental uncertainties.

$\lvert y\rvert$	20–30 (10^{-2})	30–45 (10^{-2})	45–60 (10^{-2})	60–120 (10^{-1})	120–200 (10^{-3})	200–1500 (10^{-4})
0.0–0.1	3.40 ± 0.22	5.12 ± 0.18	2.14 ± 0.06	6.05 ± 0.08	6.62 ± 0.31	10.1 ± 1.4
0.1–0.2	3.37 ± 0.21	4.89 ± 0.16	2.13 ± 0.06	6.01 ± 0.08	6.87 ± 0.31	
0.2–0.3	3.28 ± 0.21	4.93 ± 0.15	2.11 ± 0.07	6.02 ± 0.08	6.74 ± 0.32	11.6 ± 1.2
0.3–0.4	3.36 ± 0.20	4.89 ± 0.15	2.16 ± 0.07	5.96 ± 0.08	6.71 ± 0.30	
0.4–0.5	3.40 ± 0.19	4.98 ± 0.14	2.03 ± 0.08	5.96 ± 0.08	6.45 ± 0.27	12.4 ± 1.0
0.5–0.6	3.45 ± 0.18	5.16 ± 0.14	2.23 ± 0.06	5.90 ± 0.08	6.71 ± 0.28	
0.6–0.7	3.51 ± 0.17	4.99 ± 0.14	2.19 ± 0.06	5.85 ± 0.08	6.30 ± 0.29	9.94 ± 0.91
0.7–0.8	3.46 ± 0.15	4.89 ± 0.15	2.15 ± 0.07	5.71 ± 0.08	6.33 ± 0.26	
0.8–0.9	3.44 ± 0.13	5.01 ± 0.15	2.15 ± 0.06	5.57 ± 0.08	6.13 ± 0.28	10.17 ± 0.78
0.9–1.0	3.40 ± 0.12	4.88 ± 0.14	2.13 ± 0.06	5.45 ± 0.08	5.82 ± 0.24	
1.0–1.1	3.34 ± 0.11	4.90 ± 0.14	2.05 ± 0.06	5.26 ± 0.08	5.78 ± 0.23	10.04 ± 0.74
1.1–1.2	3.33 ± 0.11	4.87 ± 0.13	1.96 ± 0.06	5.04 ± 0.08	5.32 ± 0.22	
1.2–1.3	3.22 ± 0.11	4.67 ± 0.13	1.86 ± 0.06	4.76 ± 0.08	5.17 ± 0.22	9.07 ± 0.63
1.3–1.4	3.23 ± 0.13	4.91 ± 0.13	1.87 ± 0.05	4.46 ± 0.07	4.80 ± 0.21	
1.4–1.5	3.11 ± 0.14	4.59 ± 0.12	1.70 ± 0.05	4.18 ± 0.07	4.65 ± 0.21	6.16 ± 0.56
1.5–1.6	3.14 ± 0.14	4.45 ± 0.12	1.60 ± 0.06	3.75 ± 0.06	4.17 ± 0.21	
1.6–1.7	2.95 ± 0.14	4.13 ± 0.11	1.40 ± 0.04	3.39 ± 0.06	3.72 ± 0.20	4.70 ± 0.50
1.7–1.8	2.90 ± 0.15	3.67 ± 0.10	1.22 ± 0.04	2.93 ± 0.06	3.01 ± 0.19	
1.8–1.9	2.68 ± 0.14	3.16 ± 0.10	1.13 ± 0.05	2.51 ± 0.05	2.39 ± 0.18	2.89 ± 0.41
1.9–2.0	2.40 ± 0.13	2.63 ± 0.09	0.94 ± 0.05	2.03 ± 0.05	2.21 ± 0.19	
2.0–2.1	2.10 ± 0.11	2.10 ± 0.09	0.77 ± 0.05	1.57 ± 0.05	1.39 ± 0.15	1.84 ± 0.38
2.1–2.2	1.60 ± 0.09	1.50 ± 0.08	0.49 ± 0.03	1.09 ± 0.04	1.00 ± 0.14	
2.2–2.3	1.04 ± 0.08	0.89 ± 0.06	0.34 ± 0.04	0.64 ± 0.04	0.53 ± 0.10	0.41 ± 0.16
2.3–2.4	0.39 ± 0.04	0.31 ± 0.03	0.12 ± 0.02	0.20 ± 0.01	0.20 ± 0.05	

where $N_{\mathrm{u}}^{'ij}$, $N_{\mathrm{u}}^{'\mathrm{norm}}$, $\rho^{'ij}$, and $\rho^{'\mathrm{norm}}$ do not contain the FSR correction. All the r shape measurements are summarized in Tables 11–12.

These double-differential DY measurements will impose constraints on the quark and antiquark PDFs in a wide range of x, and in particular, should allow the replacement of fixed-target DY data with modern collider data in PDF analyses. Such replacement would be advantageous because fixed-target data were taken at low energies (thus being affected by larger theoretical uncertainties), mostly on nuclear targets (requiring nuclear corrections), and the full experimental covariance matrices are not provided. Fixed-target DY data has been instrumental to constrain quark flavor separation in global PDF analyses in the last 20 years, thus present measurements should become a crucial source of information on quark and antiquark PDFs in future global fits.

6 Summary

This paper presents measurements of the Drell–Yan differential cross section $\mathrm{d}\sigma/\mathrm{d}m$ in the dimuon and dielectron channels for the mass range $15 < m < 1500\,\mathrm{GeV}$ and the double-

Table 12: The DY dimuon rapidity spectrum within the detector acceptance, normalized to the Z-peak region, $r_{\text{post-FSR, det}} = (1/\sigma_Z \, d\sigma/d|y|)$, tabulated for different mass regions. The rows are the dimuon rapidity bins and the columns are mass bins (in GeV). The uncertainties are the total experimental uncertainties.

$\|y\|$	20–30 (10^{-2})	30–45 (10^{-2})	45–60 (10^{-2})	60–120 (10^{-1})	120–200 (10^{-3})	200–1500 (10^{-4})
0.0–0.1	3.37 ± 0.22	5.16 ± 0.18	2.57 ± 0.07	6.03 ± 0.08	6.32 ± 0.35	9.6 ± 1.5
0.1–0.2	3.33 ± 0.21	4.91 ± 0.16	2.57 ± 0.07	5.99 ± 0.08	6.51 ± 0.35	
0.2–0.3	3.26 ± 0.21	4.98 ± 0.15	2.53 ± 0.07	6.00 ± 0.08	6.42 ± 0.35	11.1 ± 1.3
0.3–0.4	3.33 ± 0.20	4.94 ± 0.14	2.60 ± 0.07	5.94 ± 0.08	6.36 ± 0.33	
0.4–0.5	3.38 ± 0.19	5.01 ± 0.14	2.49 ± 0.07	5.94 ± 0.08	6.15 ± 0.31	11.9 ± 1.2
0.5–0.6	3.42 ± 0.18	5.20 ± 0.15	2.66 ± 0.07	5.89 ± 0.08	6.34 ± 0.32	
0.6–0.7	3.48 ± 0.17	5.02 ± 0.15	2.62 ± 0.07	5.84 ± 0.08	5.97 ± 0.32	9.5 ± 1.0
0.7–0.8	3.42 ± 0.15	4.93 ± 0.15	2.57 ± 0.07	5.70 ± 0.08	6.01 ± 0.30	
0.8–0.9	3.41 ± 0.14	5.04 ± 0.15	2.57 ± 0.07	5.56 ± 0.08	5.86 ± 0.32	9.71 ± 0.91
0.9–1.0	3.37 ± 0.13	4.91 ± 0.15	2.53 ± 0.07	5.44 ± 0.08	5.57 ± 0.28	
1.0–1.1	3.30 ± 0.12	4.94 ± 0.15	2.46 ± 0.07	5.25 ± 0.08	5.50 ± 0.28	9.64 ± 0.88
1.1–1.2	3.30 ± 0.12	4.89 ± 0.14	2.37 ± 0.07	5.03 ± 0.08	5.08 ± 0.26	
1.2–1.3	3.19 ± 0.12	4.70 ± 0.13	2.22 ± 0.07	4.75 ± 0.07	4.90 ± 0.26	8.62 ± 0.77
1.3–1.4	3.19 ± 0.14	4.92 ± 0.13	2.20 ± 0.06	4.45 ± 0.07	4.53 ± 0.25	
1.4–1.5	3.09 ± 0.14	4.60 ± 0.13	2.02 ± 0.06	4.17 ± 0.07	4.40 ± 0.25	5.86 ± 0.65
1.5–1.6	3.09 ± 0.15	4.45 ± 0.12	1.88 ± 0.05	3.75 ± 0.06	3.97 ± 0.24	
1.6–1.7	2.91 ± 0.15	4.12 ± 0.12	1.65 ± 0.05	3.39 ± 0.06	3.53 ± 0.23	4.49 ± 0.59
1.7–1.8	2.86 ± 0.15	3.66 ± 0.11	1.45 ± 0.05	2.93 ± 0.06	2.86 ± 0.22	
1.8–1.9	2.64 ± 0.15	3.14 ± 0.10	1.31 ± 0.04	2.50 ± 0.05	2.28 ± 0.20	2.77 ± 0.50
1.9–2.0	2.36 ± 0.13	2.61 ± 0.09	1.09 ± 0.04	2.02 ± 0.05	2.09 ± 0.21	
2.0–2.1	2.05 ± 0.11	2.08 ± 0.09	0.89 ± 0.04	1.56 ± 0.05	1.32 ± 0.17	1.77 ± 0.46
2.1–2.2	1.56 ± 0.10	1.48 ± 0.07	0.58 ± 0.03	1.09 ± 0.04	0.94 ± 0.15	
2.2–2.3	1.00 ± 0.08	0.88 ± 0.07	0.39 ± 0.02	0.64 ± 0.04	0.50 ± 0.11	0.39 ± 0.20
2.3–2.4	0.37 ± 0.04	0.30 ± 0.03	0.13 ± 0.01	0.20 ± 0.01	0.19 ± 0.06	

differential cross section $d^2\sigma/dm\,d|y|$ in the dimuon channel for the mass range $20 < m < 1500\,\text{GeV}$ in proton-proton collisions at $\sqrt{s} = 7\,\text{TeV}$. The inclusive Z cross section measurements in the mass range $60 < m < 120\,\text{GeV}$ are also presented and these are the most precise measurements of the Z cross section at a hadron collider.

The differential cross section measurements are normalized to the Z-peak region (60–120 GeV), canceling the uncertainty in the integrated luminosity and reducing the PDF uncertainty in the acceptance, the pileup effect in the reconstruction efficiency, and the uncertainty of the efficiency. The measurements are corrected for the effects of resolution, which cause event migration between bins in mass and rapidity. The observed dilepton mass is also corrected for final-state photon radiation. The $d\sigma/dm$ differential cross section results are given separately for both lepton flavors in the fiducial region and are extrapolated to the full phase space. Since the electron and muon results are consistent, they are combined. The results are in good agreement with the standard model predictions, calculated at NNLO with the program FEWZ using the CT10 PDF set.

The $d^2\sigma/dm\,d|y|$ measurement is compared to the NLO prediction calculated with FEWZ using the CT10 PDFs and the NNLO theoretical predictions as computed with FEWZ using the

CT10, NNPDF2.1, MSTW2008, HERAPDF15, JR09, ABKM09, and CT10W PDFs. This is the first double-differential Drell–Yan cross section measurement with a hadron collider and will provide precise inputs to update the PDF sets.

Acknowledgments

We would like to thank the authors of FEWZ for the fruitful discussions, cooperation, and cross-checks in performing the theoretical calculations for our analysis.

We congratulate our colleagues in the CERN accelerator departments for the excellent performance of the LHC and thank the technical and administrative staffs at CERN and at other CMS institutes for their contributions to the success of the CMS effort. In addition, we gratefully acknowledge the computing centres and personnel of the Worldwide LHC Computing Grid for delivering so effectively the computing infrastructure essential to our analyses. Finally, we acknowledge the enduring support for the construction and operation of the LHC and the CMS detector provided by the following funding agencies: the Austrian Federal Ministry of Science and Research and the Austrian Science Fund; the Belgian Fonds de la Recherche Scientifique, and Fonds voor Wetenschappelijk Onderzoek; the Brazilian Funding Agencies (CNPq, CAPES, FAPERJ, and FAPESP); the Bulgarian Ministry of Education and Science; CERN; the Chinese Academy of Sciences, Ministry of Science and Technology, and National Natural Science Foundation of China; the Colombian Funding Agency (COLCIENCIAS); the Croatian Ministry of Science, Education and Sport; the Research Promotion Foundation, Cyprus; the Ministry of Education and Research, Recurrent financing contract SF0690030s09 and European Regional Development Fund, Estonia; the Academy of Finland, Finnish Ministry of Education and Culture, and Helsinki Institute of Physics; the Institut National de Physique Nucléaire et de Physique des Particules / CNRS, and Commissariat à l'Énergie Atomique et aux Énergies Alternatives / CEA, France; the Bundesministerium für Bildung und Forschung, Deutsche Forschungsgemeinschaft, and Helmholtz-Gemeinschaft Deutscher Forschungszentren, Germany; the General Secretariat for Research and Technology, Greece; the National Scientific Research Foundation, and National Innovation Office, Hungary; the Department of Atomic Energy and the Department of Science and Technology, India; the Institute for Studies in Theoretical Physics and Mathematics, Iran; the Science Foundation, Ireland; the Istituto Nazionale di Fisica Nucleare, Italy; the Korean Ministry of Education, Science and Technology and the World Class University program of NRF, Republic of Korea; the Lithuanian Academy of Sciences; the Mexican Funding Agencies (CINVESTAV, CONACYT, SEP, and UASLP-FAI); the Ministry of Business, Innovation and Employment, New Zealand; the Pakistan Atomic Energy Commission; the Ministry of Science and Higher Education and the National Science Centre, Poland; the Fundação para a Ciência e a Tecnologia, Portugal; JINR, Dubna; the Ministry of Education and Science of the Russian Federation, the Federal Agency of Atomic Energy of the Russian Federation, Russian Academy of Sciences, and the Russian Foundation for Basic Research; the Ministry of Education, Science and Technological Development of Serbia; the Secretaría de Estado de Investigación, Desarrollo e Innovación and Programa Consolider-Ingenio 2010, Spain; the Swiss Funding Agencies (ETH Board, ETH Zurich, PSI, SNF, UniZH, Canton Zurich, and SER); the National Science Council, Taipei; the Thailand Center of Excellence in Physics, the Institute for the Promotion of Teaching Science and Technology of Thailand, Special Task Force for Activating Research and the National Science and Technology Development Agency of Thailand; the Scientific and Technical Research Council of Turkey, and Turkish Atomic Energy Authority; the Science and Technology Facilities Council, UK; the US Department of Energy, and the US National Science Foundation.

Individuals have received support from the Marie-Curie programme and the European Research Council and EPLANET (European Union); the Leventis Foundation; the A. P. Sloan Foundation; the Alexander von Humboldt Foundation; the Belgian Federal Science Policy Office; the Fonds pour la Formation à la Recherche dans l'Industrie et dans l'Agriculture (FRIA-Belgium); the Agentschap voor Innovatie door Wetenschap en Technologie (IWT-Belgium); the Ministry of Education, Youth and Sports (MEYS) of Czech Republic; the Council of Science and Industrial Research, India; the Compagnia di San Paolo (Torino); the HOMING PLUS programme of Foundation for Polish Science, cofinanced by EU, Regional Development Fund; and the Thalis and Aristeia programmes cofinanced by EU-ESF and the Greek NSRF.

References

[1] R. Hamberg, W. L. van Neerven, and T. Matsuura, "A complete calculation of the order α_s^2 correction to the Drell–Yan K-factor", *Nucl. Phys. B* **359** (1991) 343, doi:10.1016/0550-3213(91)90064-5.

[2] S. Catani et al., "Vector Boson Production at Hadron Colliders: A Fully Exclusive QCD Calculation at Next-to-Next-to-Leading Order ", *Phys. Rev. Lett.* **103** (2009) 082001, doi:10.1103/PhysRevLett.103.082001, arXiv:0903.2120.

[3] S. Catani and M. Grazzini, "Next-to-Next-to-Leading-Order Subtraction Formalism in Hadron Collisions and its Application to Higgs-Boson Production at the Large Hadron Collider ", *Phys. Rev. Lett.* **98** (2007) 222002, doi:10.1103/PhysRevLett.98.222002, arXiv:hep-ph/0703012.

[4] K. Melnikov and F. Petriello, "Electroweak gauge boson production at hadron colliders through $O(\alpha_s^2)$", *Phys. Rev. D* **74** (2006) 114017, doi:10.1103/PhysRevD.74.114017, arXiv:hep-ph/0609070.

[5] M. Klein and R. Yoshida, "Collider physics at HERA", *Progress in Particle and Nuclear Physics* **61** (2008) 343, doi:10.1016/j.ppnp.2008.05.002, arXiv:0805.3334.

[6] L. Whitlow et al., "Precise measurements of the proton and deuteron structure functions from a global analysis of the SLAC deep inelastic electron scattering cross sections", *Phys. Lett. B* **282** (1992) 475, doi:10.1016/0370-2693(92)90672-Q.

[7] G. Moreno et al., "Dimuon production in proton-copper collisions at $\sqrt{s} = 38.8$ GeV", *Phys. Rev. D* **43** (1991) 2815, doi:10.1103/PhysRevD.43.2815.

[8] FNAL E866/NuSea Collaboration, "Improved measurement of the $\bar{d}/\bar{u}$ asymmetry in the nucleon sea", *Phys. Rev. D* **64** (2001) 052002, doi:10.1103/PhysRevD.64.052002, arXiv:hep-ex/0103030.

[9] CDF Collaboration, "Direct Measurement of the W Production Charge Asymmetry in $p\bar{p}$ Collisions at $\sqrt{s} = 1.96$ TeV", *Phys. Rev. Lett.* **102** (2009) 181801, doi:10.1103/PhysRevLett.102.181801, arXiv:0901.2169.

[10] D0 Collaboration, "Measurement of the muon charge asymmetry from W boson decays", *Phys. Rev. D* **77** (2008) 011106, doi:10.1103/PhysRevD.77.011106, arXiv:0709.4254.

[11] R. D. Ball et al., "A first unbiased global NLO determination of parton distributions and their uncertainties", *Nucl. Phys. B* **838** (2010) 136, doi:10.1016/j.nuclphysb.2010.05.008, arXiv:1002.4407.

[12] G. Bozzi, J. Rojo, and A. Vicini, "Impact of the parton distribution function uncertainties on the measurement of the W boson mass at the Tevatron and the LHC ", *Phys. Rev. D* **83** (2011) 113008, doi:10.1103/PhysRevD.83.113008, arXiv:1104.2056.

[13] S. Forte and G. Watt, "Progress in the Determination of the Partonic Structure of the Proton", (2013), arXiv:1301.6754. To appear in *Annual Review of Nuclear and Particle Science*, vol.63.

[14] R. D. Ball et al., "Parton distribution benchmarking with LHC data", *JHEP* **04** (2013) 125, doi:10.1007/JHEP04(2013)125, arXiv:1211.5142.

[15] CMS Collaboration, "Measurement of the Drell–Yan cross section in pp collisions at $\sqrt{s} = 7$ TeV", *JHEP* **10** (2011) 007, doi:10.1007/JHEP10(2011)007, arXiv:1108.0566.

[16] LHCb Collaboration, "Inclusive low mass Drell–Yan production in the forward region at $\sqrt{s} = 7$ TeV", (2012). LHCb-CONF-2012-013.

[17] ATLAS Collaboration, "Measurement of the high-mass Drell–Yan differential cross-section in pp collisions at $\sqrt{s} = 7$ TeV with the ATLAS detector", *Phys. Lett. B* **725** (2013) 223, doi:10.1016/j.physletb.2013.07.049, arXiv:1305.4192.

[18] R. Gavin, Y. Li, F. Petriello, and S. Quackenbush, "FEWZ 2.0: A code for hadronic Z production at next-to-next-to-leading order", *Comput. Phys. Commun.* **182** (2011) 2388, doi:10.1016/j.cpc.2011.06.008, arXiv:1011.3540.

[19] H.-L. Lai et al., "New parton distributions for collider physics", *Phys. Rev. D* **82** (2010) 074024, doi:10.1103/PhysRevD.82.074024, arXiv:1007.2241.

[20] NNPDF Collaboration, "Impact of heavy quark masses on parton distributions and LHC phenomenology", *Nucl. Phys. B* **849** (2011) 296, doi:10.1016/j.nuclphysb.2011.03.021, arXiv:1101.1300.

[21] A. D. Martin, W. J. Stirling, R. S. Thorne, and G. Watt, "Parton distributions for the LHC", *Eur. Phys. J. C* **63** (2009) 189, doi:10.1140/epjc/s10052-009-1072-5, arXiv:0901.0002.

[22] H1 and ZEUS Collaboration, "Combined measurement and QCD analysis of the inclusive $e^{\pm}p$ scattering cross sections at HERA", *JHEP* **01** (2010) 109, doi:10.1007/JHEP01(2010)109, arXiv:0911.0884.

[23] P. Jimenez-Delgado and E. Reya, "Dynamical next-to-next-to-leading order parton distributions", *Phys. Rev. D* **79** (2009) 074023, doi:10.1103/PhysRevD.79.074023, arXiv:0810.4274.

[24] S. Alekhin, J. Blumlein, S. Klein, and S. Moch, "3-, 4-, and 5-flavor next-to-next-to-leading order parton distribution functions from deep-inelastic-scattering data and at hadron colliders ", *Phys. Rev. D* **81** (2010) 014032, doi:10.1103/PhysRevD.81.014032, arXiv:0908.2766.

[25] S. Alekhin et al., "The PDF4LHC Working Group Interim Report", (2011). arXiv:1101.0536.

[26] CMS Collaboration, "The CMS experiment at the CERN LHC", *JINST* **3** (2008) S08004, doi:10.1088/1748-0221/3/08/S08004.

[27] CMS Collaboration, "CMS TriDAS Project: Technical Design Report, Volume 1: The Trigger System", CMS TDR CERN/LHCC 2000-038, (2000).

[28] CMS Collaboration, "The TriDAS Project Technical Design Report, volume II: Data acquisition and high-level trigger", CMS TDR CERN/LHCC 2002-026, (2002).

[29] GEANT4 Collaboration, "GEANT4—a simulation toolkit", *Nucl. Instrum. Meth. A* **506** (2003) 250, doi:10.1016/S0168-9002(03)01368-8.

[30] S. Alioli, P. Nason, C. Oleari, and E. Re, "NLO vector-boson production matched with shower in POWHEG", *JHEP* **07** (2008) 060, doi:10.1088/1126-6708/2008/07/060, arXiv:0805.4802.

[31] T. Sjöstrand, S. Mrenna, and P. Z. Skands, "PYTHIA 6.4 physics and manual", *JHEP* **05** (2006) 026, doi:10.1088/1126-6708/2006/05/026, arXiv:hep-ph/0603175.

[32] Z. Wąs, "TAUOLA the library for tau lepton decay, and KKMC/KORALB/KORALZ/... status report", *Nucl. Phys. Proc. Suppl.* **98** (2001) 96, doi:10.1016/S0920-5632(01)01200-2, arXiv:hep-ph/0011305.

[33] R. Field, "Min-Bias and the Underlying Event at the LHC", *Acta Phys. Polon. B* **42** (2011) 2631, doi:10.5506/APhysPolB.42.2631, arXiv:1202.0901.

[34] CMS Collaboration, "Performance of CMS muon reconstruction in pp collision events at $\sqrt{s} = 7$ TeV", *JINST* **7** (2012) P10002, doi:10.1088/1748-0221/7/10/P10002, arXiv:1206.4071.

[35] CMS Collaboration, "Commissioning of the particle-flow event reconstruction with leptons from J/ψ and W decays at 7 TeV", CMS Physics Analysis Summary CMS-PAS-PFT-10-003, (2010).

[36] CMS Collaboration, "Energy calibration and resolution of the CMS electromagnetic calorimeter in pp collisions at $\sqrt{s} = 7$ TeV", *JINST* **8** (2013) P09009, doi:10.1088/1748-0221/8/09/P09009, arXiv:1306.2016.

[37] CMS Collaboration, "Measurement of the inclusive W and Z production cross sections in pp collisions at $\sqrt{s} = 7$ TeV with the CMS experiment", *JHEP* **10** (2011) 132, doi:10.1007/JHEP10(2011)132, arXiv:1107.4789.

[38] Particle Data Group, "Review of Particle Physics", *Phys. Rev. D* **86** (2012) 010001, doi:10.1103/PhysRevD.86.010001.

[39] A. Bodek et al., "Extracting muon momentum scale corrections for hadron collider experiments", *Eur. Phys. J. C* **72** (2012) 2194, doi:10.1140/epjc/s10052-012-2194-8, arXiv:1208.3710.

[40] V. Blobel, "An unfolding method for high-energy physics experiments", (2002). arXiv:hep-ex/0208022. Unpublished.

[41] CMS Collaboration, "Electron Reconstruction and Identification at $\sqrt{s} = 7$ TeV", Technical Report CMS Physics Analysis Summary CMS-PAS-EGM-10-004, (2010).

[42] J. Wenninger, "Energy Calibration of the LHC Beams at 4 TeV", (2013). CERN-ATS-2013-040.

[43] H. Burkhardt and B. Pietrzyk, "Update of the hadronic contribution to the QED vacuum polarization", *Phys. Lett. B* **513** (2001) 46, doi:10.1016/S0370-2693(01)00393-8.

[44] D. Bourilkov, "Study of parton density function uncertainties with LHAPDF and PYTHIA at LHC", (2003). arXiv:hep-ph/0305126.

[45] M. R. Whalley, D. Bourilkov, and R. C. Group, "The Les Houches accord PDFs (LHAPDF) and LHAGLUE", (2005). arXiv:hep-ph/0508110.

[46] D. Bourilkov, R. C. Group, and M. R. Whalley, "LHAPDF: PDF use from the Tevatron to the LHC", (2006). arXiv:hep-ph/0605240.

[47] CMS Collaboration, "Measurement of the W and Z inclusive production cross sections at $\sqrt{s} = 7$ TeV with the CMS experiment at the LHC", *JHEP* **01** (2011) 080, doi:10.1007/JHEP01(2011)080, arXiv:1012.2466.

[48] G. Lafferty and T. Wyatt, "Where to stick your data points: The treatment of measurements within wide bins", *Nucl. Instr. Meth. A* **355** (1995) 541, doi:10.1016/0168-9002(94)01112-5.

[49] Y. Li and F. Petriello, "Combining QCD and electroweak corrections to dilepton production in the framework of the FEWZ simulation code", *Phys. Rev. D* **86** (2012) 094034, doi:10.1103/PhysRevD.86.094034, arXiv:1208.5967.

[50] A. Valassi, "Combining correlated measurements of several different physical quantities", *Nucl. Instrum. Meth. A* **500** (2003) 391, doi:10.1016/S0168-9002(03)00329-2.

A The CMS Collaboration

Yerevan Physics Institute, Yerevan, Armenia
S. Chatrchyan, V. Khachatryan, A.M. Sirunyan, A. Tumasyan

Institut für Hochenergiephysik der OeAW, Wien, Austria
W. Adam, T. Bergauer, M. Dragicevic, J. Erö, C. Fabjan[1], M. Friedl, R. Frühwirth[1], V.M. Ghete, N. Hörmann, J. Hrubec, M. Jeitler[1], W. Kiesenhofer, V. Knünz, M. Krammer[1], I. Krätschmer, D. Liko, I. Mikulec, D. Rabady[2], B. Rahbaran, C. Rohringer, H. Rohringer, R. Schöfbeck, J. Strauss, A. Taurok, W. Treberer-Treberspurg, W. Waltenberger, C.-E. Wulz[1]

National Centre for Particle and High Energy Physics, Minsk, Belarus
V. Mossolov, N. Shumeiko, J. Suarez Gonzalez

Universiteit Antwerpen, Antwerpen, Belgium
S. Alderweireldt, M. Bansal, S. Bansal, T. Cornelis, E.A. De Wolf, X. Janssen, A. Knutsson, S. Luyckx, L. Mucibello, S. Ochesanu, B. Roland, R. Rougny, Z. Staykova, H. Van Haevermaet, P. Van Mechelen, N. Van Remortel, A. Van Spilbeeck

Vrije Universiteit Brussel, Brussel, Belgium
F. Blekman, S. Blyweert, J. D'Hondt, A. Kalogeropoulos, J. Keaveney, M. Maes, A. Olbrechts, S. Tavernier, W. Van Doninck, P. Van Mulders, G.P. Van Onsem, I. Villella

Université Libre de Bruxelles, Bruxelles, Belgium
C. Caillol, B. Clerbaux, G. De Lentdecker, L. Favart, A.P.R. Gay, T. Hreus, A. Léonard, P.E. Marage, A. Mohammadi, L. Perniè, T. Reis, T. Seva, L. Thomas, C. Vander Velde, P. Vanlaer, J. Wang

Ghent University, Ghent, Belgium
V. Adler, K. Beernaert, L. Benucci, A. Cimmino, S. Costantini, S. Dildick, G. Garcia, B. Klein, J. Lellouch, A. Marinov, J. Mccartin, A.A. Ocampo Rios, D. Ryckbosch, M. Sigamani, N. Strobbe, F. Thyssen, M. Tytgat, S. Walsh, E. Yazgan, N. Zaganidis

Université Catholique de Louvain, Louvain-la-Neuve, Belgium
S. Basegmez, C. Beluffi[3], G. Bruno, R. Castello, A. Caudron, L. Ceard, G.G. Da Silveira, C. Delaere, T. du Pree, D. Favart, L. Forthomme, A. Giammanco[4], J. Hollar, P. Jez, V. Lemaitre, J. Liao, O. Militaru, C. Nuttens, D. Pagano, A. Pin, K. Piotrzkowski, A. Popov[5], M. Selvaggi, M. Vidal Marono, J.M. Vizan Garcia

Université de Mons, Mons, Belgium
N. Beliy, T. Caebergs, E. Daubie, G.H. Hammad

Centro Brasileiro de Pesquisas Fisicas, Rio de Janeiro, Brazil
G.A. Alves, M. Correa Martins Junior, T. Martins, M.E. Pol, M.H.G. Souza

Universidade do Estado do Rio de Janeiro, Rio de Janeiro, Brazil
W.L. Aldá Júnior, W. Carvalho, J. Chinellato[6], A. Custódio, E.M. Da Costa, D. De Jesus Damiao, C. De Oliveira Martins, S. Fonseca De Souza, H. Malbouisson, M. Malek, D. Matos Figueiredo, L. Mundim, H. Nogima, W.L. Prado Da Silva, A. Santoro, A. Sznajder, E.J. Tonelli Manganote[6], A. Vilela Pereira

Universidade Estadual Paulista [a], Universidade Federal do ABC [b], São Paulo, Brazil
C.A. Bernardes[b], F.A. Dias[a,7], T.R. Fernandez Perez Tomei[a], E.M. Gregores[b], C. Lagana[a], P.G. Mercadante[b], S.F. Novaes[a], Sandra S. Padula[a]

Institute for Nuclear Research and Nuclear Energy, Sofia, Bulgaria
V. Genchev[2], P. Iaydjiev[2], S. Piperov, M. Rodozov, S. Stoykova, G. Sultanov, V. Tcholakov, M. Vutova

University of Sofia, Sofia, Bulgaria
A. Dimitrov, R. Hadjiiska, V. Kozhuharov, L. Litov, B. Pavlov, P. Petkov

Institute of High Energy Physics, Beijing, China
J.G. Bian, G.M. Chen, H.S. Chen, C.H. Jiang, D. Liang, S. Liang, X. Meng, J. Tao, X. Wang, Z. Wang, H. Xiao

State Key Laboratory of Nuclear Physics and Technology, Peking University, Beijing, China
C. Asawatangtrakuldee, Y. Ban, Y. Guo, Q. Li, W. Li, S. Liu, Y. Mao, S.J. Qian, D. Wang, L. Zhang, W. Zou

Universidad de Los Andes, Bogota, Colombia
C. Avila, C.A. Carrillo Montoya, L.F. Chaparro Sierra, J.P. Gomez, B. Gomez Moreno, J.C. Sanabria

Technical University of Split, Split, Croatia
N. Godinovic, D. Lelas, R. Plestina[8], D. Polic, I. Puljak

University of Split, Split, Croatia
Z. Antunovic, M. Kovac

Institute Rudjer Boskovic, Zagreb, Croatia
V. Brigljevic, K. Kadija, J. Luetic, D. Mekterovic, S. Morovic, L. Tikvica

University of Cyprus, Nicosia, Cyprus
A. Attikis, G. Mavromanolakis, J. Mousa, C. Nicolaou, F. Ptochos, P.A. Razis

Charles University, Prague, Czech Republic
M. Finger, M. Finger Jr.

Academy of Scientific Research and Technology of the Arab Republic of Egypt, Egyptian Network of High Energy Physics, Cairo, Egypt
A.A. Abdelalim[9], Y. Assran[10], S. Elgammal[9], A. Ellithi Kamel[11], M.A. Mahmoud[12], A. Radi[13,14]

National Institute of Chemical Physics and Biophysics, Tallinn, Estonia
M. Kadastik, M. Müntel, M. Murumaa, M. Raidal, L. Rebane, A. Tiko

Department of Physics, University of Helsinki, Helsinki, Finland
P. Eerola, G. Fedi, M. Voutilainen

Helsinki Institute of Physics, Helsinki, Finland
J. Härkönen, V. Karimäki, R. Kinnunen, M.J. Kortelainen, T. Lampén, K. Lassila-Perini, S. Lehti, T. Lindén, P. Luukka, T. Mäenpää, T. Peltola, E. Tuominen, J. Tuominiemi, E. Tuovinen, L. Wendland

Lappeenranta University of Technology, Lappeenranta, Finland
T. Tuuva

DSM/IRFU, CEA/Saclay, Gif-sur-Yvette, France
M. Besancon, F. Couderc, M. Dejardin, D. Denegri, B. Fabbro, J.L. Faure, F. Ferri, S. Ganjour, A. Givernaud, P. Gras, G. Hamel de Monchenault, P. Jarry, E. Locci, J. Malcles, L. Millischer, A. Nayak, J. Rander, A. Rosowsky, M. Titov

Laboratoire Leprince-Ringuet, Ecole Polytechnique, IN2P3-CNRS, Palaiseau, France
S. Baffioni, F. Beaudette, L. Benhabib, M. Bluj[15], P. Busson, C. Charlot, N. Daci, T. Dahms, M. Dalchenko, L. Dobrzynski, A. Florent, R. Granier de Cassagnac, M. Haguenauer, P. Miné, C. Mironov, I.N. Naranjo, M. Nguyen, C. Ochando, P. Paganini, D. Sabes, R. Salerno, Y. Sirois, C. Veelken, A. Zabi

Institut Pluridisciplinaire Hubert Curien, Université de Strasbourg, Université de Haute Alsace Mulhouse, CNRS/IN2P3, Strasbourg, France
J.-L. Agram[16], J. Andrea, D. Bloch, J.-M. Brom, E.C. Chabert, C. Collard, E. Conte[16], F. Drouhin[16], J.-C. Fontaine[16], D. Gelé, U. Goerlach, C. Goetzmann, P. Juillot, A.-C. Le Bihan, P. Van Hove

Centre de Calcul de l'Institut National de Physique Nucleaire et de Physique des Particules, CNRS/IN2P3, Villeurbanne, France
S. Gadrat

Université de Lyon, Université Claude Bernard Lyon 1, CNRS-IN2P3, Institut de Physique Nucléaire de Lyon, Villeurbanne, France
S. Beauceron, N. Beaupere, G. Boudoul, S. Brochet, J. Chasserat, R. Chierici, D. Contardo, P. Depasse, H. El Mamouni, J. Fan, J. Fay, S. Gascon, M. Gouzevitch, B. Ille, T. Kurca, M. Lethuillier, L. Mirabito, S. Perries, L. Sgandurra, V. Sordini, M. Vander Donckt, P. Verdier, S. Viret

Institute of High Energy Physics and Informatization, Tbilisi State University, Tbilisi, Georgia
Z. Tsamalaidze[17]

RWTH Aachen University, I. Physikalisches Institut, Aachen, Germany
C. Autermann, S. Beranek, M. Bontenackels, B. Calpas, M. Edelhoff, L. Feld, N. Heracleous, O. Hindrichs, K. Klein, A. Ostapchuk, A. Perieanu, F. Raupach, J. Sammet, S. Schael, D. Sprenger, H. Weber, B. Wittmer, V. Zhukov[5]

RWTH Aachen University, III. Physikalisches Institut A, Aachen, Germany
M. Ata, J. Caudron, E. Dietz-Laursonn, D. Duchardt, M. Erdmann, R. Fischer, A. Güth, T. Hebbeker, C. Heidemann, K. Hoepfner, D. Klingebiel, S. Knutzen, P. Kreuzer, M. Merschmeyer, A. Meyer, M. Olschewski, K. Padeken, P. Papacz, H. Pieta, H. Reithler, S.A. Schmitz, L. Sonnenschein, J. Steggemann, D. Teyssier, S. Thüer, M. Weber

RWTH Aachen University, III. Physikalisches Institut B, Aachen, Germany
V. Cherepanov, Y. Erdogan, G. Flügge, H. Geenen, M. Geisler, W. Haj Ahmad, F. Hoehle, B. Kargoll, T. Kress, Y. Kuessel, J. Lingemann[2], A. Nowack, I.M. Nugent, L. Perchalla, O. Pooth, A. Stahl

Deutsches Elektronen-Synchrotron, Hamburg, Germany
I. Asin, N. Bartosik, J. Behr, W. Behrenhoff, U. Behrens, A.J. Bell, M. Bergholz[18], A. Bethani, K. Borras, A. Burgmeier, A. Cakir, L. Calligaris, A. Campbell, S. Choudhury, F. Costanza, C. Diez Pardos, S. Dooling, T. Dorland, G. Eckerlin, D. Eckstein, G. Flucke, A. Geiser, I. Glushkov, A. Grebenyuk, P. Gunnellini, S. Habib, J. Hauk, G. Hellwig, D. Horton, H. Jung, M. Kasemann, P. Katsas, C. Kleinwort, H. Kluge, M. Krämer, D. Krücker, E. Kuznetsova, W. Lange, J. Leonard, K. Lipka, W. Lohmann[18], B. Lutz, R. Mankel, I. Marfin, I.-A. Melzer-Pellmann, A.B. Meyer, J. Mnich, A. Mussgiller, S. Naumann-Emme, O. Novgorodova, F. Nowak, J. Olzem, H. Perrey, A. Petrukhin, D. Pitzl, R. Placakyte, A. Raspereza, P.M. Ribeiro

Cipriano, C. Riedl, E. Ron, M.Ö. Sahin, J. Salfeld-Nebgen, R. Schmidt[18], T. Schoerner-Sadenius, N. Sen, M. Stein, R. Walsh, C. Wissing

University of Hamburg, Hamburg, Germany
M. Aldaya Martin, V. Blobel, H. Enderle, J. Erfle, E. Garutti, U. Gebbert, M. Görner, M. Gosselink, J. Haller, K. Heine, R.S. Höing, G. Kaussen, H. Kirschenmann, R. Klanner, R. Kogler, J. Lange, I. Marchesini, T. Peiffer, N. Pietsch, D. Rathjens, C. Sander, H. Schettler, P. Schleper, E. Schlieckau, A. Schmidt, M. Schröder, T. Schum, M. Seidel, J. Sibille[19], V. Sola, H. Stadie, G. Steinbrück, J. Thomsen, D. Troendle, E. Usai, L. Vanelderen

Institut für Experimentelle Kernphysik, Karlsruhe, Germany
C. Barth, C. Baus, J. Berger, C. Böser, E. Butz, T. Chwalek, W. De Boer, A. Descroix, A. Dierlamm, M. Feindt, M. Guthoff[2], F. Hartmann[2], T. Hauth[2], H. Held, K.H. Hoffmann, U. Husemann, I. Katkov[5], J.R. Komaragiri, A. Kornmayer[2], P. Lobelle Pardo, D. Martschei, Th. Müller, M. Niegel, A. Nürnberg, O. Oberst, J. Ott, G. Quast, K. Rabbertz, F. Ratnikov, S. Röcker, F.-P. Schilling, G. Schott, H.J. Simonis, F.M. Stober, R. Ulrich, J. Wagner-Kuhr, S. Wayand, T. Weiler, M. Zeise

Institute of Nuclear and Particle Physics (INPP), NCSR Demokritos, Aghia Paraskevi, Greece
G. Anagnostou, G. Daskalakis, T. Geralis, S. Kesisoglou, A. Kyriakis, D. Loukas, A. Markou, C. Markou, E. Ntomari, I. Topsis-giotis

University of Athens, Athens, Greece
L. Gouskos, A. Panagiotou, N. Saoulidou, E. Stiliaris

University of Ioánnina, Ioánnina, Greece
X. Aslanoglou, I. Evangelou, G. Flouris, C. Foudas, P. Kokkas, N. Manthos, I. Papadopoulos, E. Paradas

KFKI Research Institute for Particle and Nuclear Physics, Budapest, Hungary
G. Bencze, C. Hajdu, P. Hidas, D. Horvath[20], F. Sikler, V. Veszpremi, G. Vesztergombi[21], A.J. Zsigmond

Institute of Nuclear Research ATOMKI, Debrecen, Hungary
N. Beni, S. Czellar, J. Molnar, J. Palinkas, Z. Szillasi

University of Debrecen, Debrecen, Hungary
J. Karancsi, P. Raics, Z.L. Trocsanyi, B. Ujvari

National Institute of Science Education and Research, Bhubaneswar, India
S.K. Swain[22]

Panjab University, Chandigarh, India
S.B. Beri, V. Bhatnagar, N. Dhingra, R. Gupta, M. Kaur, M.Z. Mehta, M. Mittal, N. Nishu, A. Sharma, J.B. Singh

University of Delhi, Delhi, India
Ashok Kumar, Arun Kumar, S. Ahuja, A. Bhardwaj, B.C. Choudhary, S. Malhotra, M. Naimuddin, K. Ranjan, P. Saxena, V. Sharma, R.K. Shivpuri

Saha Institute of Nuclear Physics, Kolkata, India
S. Banerjee, S. Bhattacharya, K. Chatterjee, S. Dutta, B. Gomber, Sa. Jain, Sh. Jain, R. Khurana, A. Modak, S. Mukherjee, D. Roy, S. Sarkar, M. Sharan, A.P. Singh

Bhabha Atomic Research Centre, Mumbai, India
A. Abdulsalam, D. Dutta, S. Kailas, V. Kumar, A.K. Mohanty[2], L.M. Pant, P. Shukla, A. Topkar

Tata Institute of Fundamental Research - EHEP, Mumbai, India
T. Aziz, R.M. Chatterjee, S. Ganguly, S. Ghosh, M. Guchait[23], A. Gurtu[24], G. Kole, S. Kumar, M. Maity[25], G. Majumder, K. Mazumdar, G.B. Mohanty, B. Parida, K. Sudhakar, N. Wickramage[26]

Tata Institute of Fundamental Research - HECR, Mumbai, India
S. Banerjee, S. Dugad

Institute for Research in Fundamental Sciences (IPM), Tehran, Iran
H. Arfaei, H. Bakhshiansohi, S.M. Etesami[27], A. Fahim[28], A. Jafari, M. Khakzad, M. Mohammadi Najafabadi, S. Paktinat Mehdiabadi, B. Safarzadeh[29], M. Zeinali

University College Dublin, Dublin, Ireland
M. Grunewald

INFN Sezione di Bari [a], Università di Bari [b], Politecnico di Bari [c], Bari, Italy
M. Abbrescia[a,b], L. Barbone[a,b], C. Calabria[a,b], S.S. Chhibra[a,b], A. Colaleo[a], D. Creanza[a,c], N. De Filippis[a,c], M. De Palma[a,b], L. Fiore[a], G. Iaselli[a,c], G. Maggi[a,c], M. Maggi[a], B. Marangelli[a,b], S. My[a,c], S. Nuzzo[a,b], N. Pacifico[a], A. Pompili[a,b], G. Pugliese[a,c], G. Selvaggi[a,b], L. Silvestris[a], G. Singh[a,b], R. Venditti[a,b], P. Verwilligen[a], G. Zito[a]

INFN Sezione di Bologna [a], Università di Bologna [b], Bologna, Italy
G. Abbiendi[a], A.C. Benvenuti[a], D. Bonacorsi[a,b], S. Braibant-Giacomelli[a,b], L. Brigliadori[a,b], R. Campanini[a,b], P. Capiluppi[a,b], A. Castro[a,b], F.R. Cavallo[a], G. Codispoti[a,b], M. Cuffiani[a,b], G.M. Dallavalle[a], F. Fabbri[a], A. Fanfani[a,b], D. Fasanella[a,b], P. Giacomelli[a], C. Grandi[a], L. Guiducci[a,b], S. Marcellini[a], G. Masetti[a], M. Meneghelli[a,b], A. Montanari[a], F.L. Navarria[a,b], F. Odorici[a], A. Perrotta[a], F. Primavera[a,b], A.M. Rossi[a,b], T. Rovelli[a,b], G.P. Siroli[a,b], N. Tosi[a,b], R. Travaglini[a,b]

INFN Sezione di Catania [a], Università di Catania [b], Catania, Italy
S. Albergo[a,b], M. Chiorboli[a,b], S. Costa[a,b], F. Giordano[a,2], R. Potenza[a,b], A. Tricomi[a,b], C. Tuve[a,b]

INFN Sezione di Firenze [a], Università di Firenze [b], Firenze, Italy
G. Barbagli[a], V. Ciulli[a,b], C. Civinini[a], R. D'Alessandro[a,b], E. Focardi[a,b], S. Frosali[a,b], E. Gallo[a], S. Gonzi[a,b], V. Gori[a,b], P. Lenzi[a,b], M. Meschini[a], S. Paoletti[a], G. Sguazzoni[a], A. Tropiano[a,b]

INFN Laboratori Nazionali di Frascati, Frascati, Italy
L. Benussi, S. Bianco, F. Fabbri, D. Piccolo

INFN Sezione di Genova [a], Università di Genova [b], Genova, Italy
P. Fabbricatore[a], R. Ferretti[a,b], F. Ferro[a], M. Lo Vetere[a,b], R. Musenich[a], E. Robutti[a], S. Tosi[a,b]

INFN Sezione di Milano-Bicocca [a], Università di Milano-Bicocca [b], Milano, Italy
A. Benaglia[a], M.E. Dinardo[a,b], S. Fiorendi[a,b], S. Gennai[a], A. Ghezzi[a,b], P. Govoni[a,b], M.T. Lucchini[a,b,2], S. Malvezzi[a], R.A. Manzoni[a,b,2], A. Martelli[a,b,2], D. Menasce[a], L. Moroni[a], M. Paganoni[a,b], D. Pedrini[a], S. Ragazzi[a,b], N. Redaelli[a], T. Tabarelli de Fatis[a,b]

INFN Sezione di Napoli [a], Università di Napoli 'Federico II' [b], Università della Basilicata (Potenza) [c], Università G. Marconi (Roma) [d], Napoli, Italy
S. Buontempo[a], N. Cavallo[a,c], A. De Cosa[a,b], F. Fabozzi[a,c], A.O.M. Iorio[a,b], L. Lista[a], S. Meola[a,d,2], M. Merola[a], P. Paolucci[a,2]

INFN Sezione di Padova [a], Università di Padova [b], Università di Trento (Trento) [c], Padova, Italy
P. Azzi[a], N. Bacchetta[a], D. Bisello[a,b], A. Branca[a,b], R. Carlin[a,b], P. Checchia[a], T. Dorigo[a], S. Fantinel[a], M. Galanti[a,b,2], F. Gasparini[a,b], U. Gasparini[a,b], P. Giubilato[a,b], A. Gozzelino[a], M. Gulmini[a,30], K. Kanishchev[a,c], S. Lacaprara[a], I. Lazzizzera[a,c], M. Margoni[a,b], G. Maron[a,30], A.T. Meneguzzo[a,b], M. Michelotto[a], J. Pazzini[a,b], N. Pozzobon[a,b], P. Ronchese[a,b], F. Simonetto[a,b], E. Torassa[a], M. Tosi[a,b], S. Vanini[a,b], P. Zotto[a,b], A. Zucchetta[a,b], G. Zumerle[a,b]

INFN Sezione di Pavia [a], Università di Pavia [b], Pavia, Italy
M. Gabusi[a,b], S.P. Ratti[a,b], C. Riccardi[a,b], P. Vitulo[a,b]

INFN Sezione di Perugia [a], Università di Perugia [b], Perugia, Italy
M. Biasini[a,b], G.M. Bilei[a], L. Fanò[a,b], P. Lariccia[a,b], G. Mantovani[a,b], M. Menichelli[a], A. Nappi[a,b†], F. Romeo[a,b], A. Saha[a], A. Santocchia[a,b], A. Spiezia[a,b]

INFN Sezione di Pisa [a], Università di Pisa [b], Scuola Normale Superiore di Pisa [c], Pisa, Italy
K. Androsov[a,31], P. Azzurri[a], G. Bagliesi[a], J. Bernardini[a], T. Boccali[a], G. Broccolo[a,c], R. Castaldi[a], M.A. Ciocci[a], R.T. D'Agnolo[a,c,2], R. Dell'Orso[a], F. Fiori[a,c], L. Foà[a,c], A. Giassi[a], M.T. Grippo[a,31], A. Kraan[a], F. Ligabue[a,c], T. Lomtadze[a], L. Martini[a,31], A. Messineo[a,b], C.S. Moon[a], F. Palla[a], A. Rizzi[a,b], A. Savoy-Navarro[a,32], A.T. Serban[a], P. Spagnolo[a], P. Squillacioti[a], R. Tenchini[a], G. Tonelli[a,b], A. Venturi[a], P.G. Verdini[a], C. Vernieri[a,c]

INFN Sezione di Roma [a], Università di Roma [b], Roma, Italy
L. Barone[a,b], F. Cavallari[a], D. Del Re[a,b], M. Diemoz[a], M. Grassi[a,b], E. Longo[a,b], F. Margaroli[a,b], P. Meridiani[a], F. Micheli[a,b], S. Nourbakhsh[a,b], G. Organtini[a,b], R. Paramatti[a], S. Rahatlou[a,b], C. Rovelli[a], L. Soffi[a,b]

INFN Sezione di Torino [a], Università di Torino [b], Università del Piemonte Orientale (Novara) [c], Torino, Italy
N. Amapane[a,b], R. Arcidiacono[a,c], S. Argiro[a,b], M. Arneodo[a,c], R. Bellan[a,b], C. Biino[a], N. Cartiglia[a], S. Casasso[a,b], M. Costa[a,b], A. Degano[a,b], N. Demaria[a], C. Mariotti[a], S. Maselli[a], E. Migliore[a,b], V. Monaco[a,b], M. Musich[a], M.M. Obertino[a,c], N. Pastrone[a], M. Pelliccioni[a,2], A. Potenza[a,b], A. Romero[a,b], M. Ruspa[a,c], R. Sacchi[a,b], A. Solano[a,b], A. Staiano[a], U. Tamponi[a]

INFN Sezione di Trieste [a], Università di Trieste [b], Trieste, Italy
S. Belforte[a], V. Candelise[a,b], M. Casarsa[a], F. Cossutti[a,2], G. Della Ricca[a,b], B. Gobbo[a], C. La Licata[a,b], M. Marone[a,b], D. Montanino[a,b], A. Penzo[a], A. Schizzi[a,b], A. Zanetti[a]

Kangwon National University, Chunchon, Korea
S. Chang, T.Y. Kim, S.K. Nam

Kyungpook National University, Daegu, Korea
D.H. Kim, G.N. Kim, J.E. Kim, D.J. Kong, S. Lee, Y.D. Oh, H. Park, D.C. Son

Chonnam National University, Institute for Universe and Elementary Particles, Kwangju, Korea
J.Y. Kim, Zero J. Kim, S. Song

Korea University, Seoul, Korea
S. Choi, D. Gyun, B. Hong, M. Jo, H. Kim, T.J. Kim, K.S. Lee, S.K. Park, Y. Roh

University of Seoul, Seoul, Korea
M. Choi, J.H. Kim, C. Park, I.C. Park, S. Park, G. Ryu

Sungkyunkwan University, Suwon, Korea
Y. Choi, Y.K. Choi, J. Goh, M.S. Kim, E. Kwon, B. Lee, J. Lee, S. Lee, H. Seo, I. Yu

Vilnius University, Vilnius, Lithuania
I. Grigelionis, A. Juodagalvis

Centro de Investigacion y de Estudios Avanzados del IPN, Mexico City, Mexico
H. Castilla-Valdez, E. De La Cruz-Burelo, I. Heredia-de La Cruz[33], R. Lopez-Fernandez, J. Martínez-Ortega, A. Sanchez-Hernandez, L.M. Villasenor-Cendejas

Universidad Iberoamericana, Mexico City, Mexico
S. Carrillo Moreno, F. Vazquez Valencia

Benemerita Universidad Autonoma de Puebla, Puebla, Mexico
H.A. Salazar Ibarguen

Universidad Autónoma de San Luis Potosí, San Luis Potosí, Mexico
E. Casimiro Linares, A. Morelos Pineda, M.A. Reyes-Santos

University of Auckland, Auckland, New Zealand
D. Krofcheck

University of Canterbury, Christchurch, New Zealand
P.H. Butler, R. Doesburg, S. Reucroft, H. Silverwood

National Centre for Physics, Quaid-I-Azam University, Islamabad, Pakistan
M. Ahmad, M.I. Asghar, J. Butt, H.R. Hoorani, S. Khalid, W.A. Khan, T. Khurshid, S. Qazi, M.A. Shah, M. Shoaib

National Centre for Nuclear Research, Swierk, Poland
H. Bialkowska, B. Boimska, T. Frueboes, M. Górski, M. Kazana, K. Nawrocki, K. Romanowska-Rybinska, M. Szleper, G. Wrochna, P. Zalewski

Institute of Experimental Physics, Faculty of Physics, University of Warsaw, Warsaw, Poland
G. Brona, K. Bunkowski, M. Cwiok, W. Dominik, K. Doroba, A. Kalinowski, M. Konecki, J. Krolikowski, M. Misiura, W. Wolszczak

Laboratório de Instrumentação e Física Experimental de Partículas, Lisboa, Portugal
N. Almeida, P. Bargassa, C. Beirão Da Cruz E Silva, P. Faccioli, P.G. Ferreira Parracho, M. Gallinaro, F. Nguyen, J. Rodrigues Antunes, J. Seixas[2], J. Varela, P. Vischia

Joint Institute for Nuclear Research, Dubna, Russia
S. Afanasiev, P. Bunin, M. Gavrilenko, I. Golutvin, I. Gorbunov, A. Kamenev, V. Karjavin, V. Konoplyanikov, A. Lanev, A. Malakhov, V. Matveev, P. Moisenz, V. Palichik, V. Perelygin, S. Shmatov, N. Skatchkov, V. Smirnov, A. Zarubin

Petersburg Nuclear Physics Institute, Gatchina (St. Petersburg), Russia
S. Evstyukhin, V. Golovtsov, Y. Ivanov, V. Kim, P. Levchenko, V. Murzin, V. Oreshkin, I. Smirnov, V. Sulimov, L. Uvarov, S. Vavilov, A. Vorobyev, An. Vorobyev

Institute for Nuclear Research, Moscow, Russia
Yu. Andreev, A. Dermenev, S. Gninenko, N. Golubev, M. Kirsanov, N. Krasnikov, A. Pashenkov, D. Tlisov, A. Toropin

Institute for Theoretical and Experimental Physics, Moscow, Russia
V. Epshteyn, M. Erofeeva, V. Gavrilov, N. Lychkovskaya, V. Popov, G. Safronov, S. Semenov, A. Spiridonov, V. Stolin, E. Vlasov, A. Zhokin

P.N. Lebedev Physical Institute, Moscow, Russia
V. Andreev, M. Azarkin, I. Dremin, M. Kirakosyan, A. Leonidov, G. Mesyats, S.V. Rusakov, A. Vinogradov

Skobeltsyn Institute of Nuclear Physics, Lomonosov Moscow State University, Moscow, Russia
A. Belyaev, E. Boos, M. Dubinin[7], L. Dudko, A. Ershov, A. Gribushin, V. Klyukhin, O. Kodolova, I. Lokhtin, A. Markina, S. Obraztsov, S. Petrushanko, V. Savrin, A. Snigirev

State Research Center of Russian Federation, Institute for High Energy Physics, Protvino, Russia
I. Azhgirey, I. Bayshev, S. Bitioukov, V. Kachanov, A. Kalinin, D. Konstantinov, V. Krychkine, V. Petrov, R. Ryutin, A. Sobol, L. Tourtchanovitch, S. Troshin, N. Tyurin, A. Uzunian, A. Volkov

University of Belgrade, Faculty of Physics and Vinca Institute of Nuclear Sciences, Belgrade, Serbia
P. Adzic[34], M. Djordjevic, M. Ekmedzic, D. Krpic[34], J. Milosevic

Centro de Investigaciones Energéticas Medioambientales y Tecnológicas (CIEMAT), Madrid, Spain
M. Aguilar-Benitez, J. Alcaraz Maestre, C. Battilana, E. Calvo, M. Cerrada, M. Chamizo Llatas[2], N. Colino, B. De La Cruz, A. Delgado Peris, D. Domínguez Vázquez, C. Fernandez Bedoya, J.P. Fernández Ramos, A. Ferrando, J. Flix, M.C. Fouz, P. Garcia-Abia, O. Gonzalez Lopez, S. Goy Lopez, J.M. Hernandez, M.I. Josa, G. Merino, E. Navarro De Martino, J. Puerta Pelayo, A. Quintario Olmeda, I. Redondo, L. Romero, J. Santaolalla, M.S. Soares, C. Willmott

Universidad Autónoma de Madrid, Madrid, Spain
C. Albajar, J.F. de Trocóniz

Universidad de Oviedo, Oviedo, Spain
H. Brun, J. Cuevas, J. Fernandez Menendez, S. Folgueras, I. Gonzalez Caballero, L. Lloret Iglesias, J. Piedra Gomez

Instituto de Física de Cantabria (IFCA), CSIC-Universidad de Cantabria, Santander, Spain
J.A. Brochero Cifuentes, I.J. Cabrillo, A. Calderon, S.H. Chuang, J. Duarte Campderros, M. Fernandez, G. Gomez, J. Gonzalez Sanchez, A. Graziano, C. Jorda, A. Lopez Virto, J. Marco, R. Marco, C. Martinez Rivero, F. Matorras, F.J. Munoz Sanchez, T. Rodrigo, A.Y. Rodríguez-Marrero, A. Ruiz-Jimeno, L. Scodellaro, I. Vila, R. Vilar Cortabitarte

CERN, European Organization for Nuclear Research, Geneva, Switzerland
D. Abbaneo, E. Auffray, G. Auzinger, M. Bachtis, P. Baillon, A.H. Ball, D. Barney, J. Bendavid, J.F. Benitez, C. Bernet[8], G. Bianchi, P. Bloch, A. Bocci, A. Bonato, O. Bondu, C. Botta, H. Breuker, T. Camporesi, G. Cerminara, T. Christiansen, J.A. Coarasa Perez, S. Colafranceschi[35], M. D'Alfonso, D. d'Enterria, A. Dabrowski, A. David, F. De Guio, A. De Roeck, S. De Visscher, S. Di Guida, M. Dobson, N. Dupont-Sagorin, A. Elliott-Peisert, J. Eugster, W. Funk, G. Georgiou, M. Giffels, D. Gigi, K. Gill, D. Giordano, M. Girone, M. Giunta, F. Glege, R. Gomez-Reino Garrido, S. Gowdy, R. Guida, J. Hammer, M. Hansen, P. Harris, C. Hartl, A. Hinzmann, V. Innocente, P. Janot, E. Karavakis, K. Kousouris, K. Krajczar, P. Lecoq, Y.-J. Lee, C. Lourenço, N. Magini, L. Malgeri, M. Mannelli, L. Masetti, F. Meijers, S. Mersi, E. Meschi, R. Moser, M. Mulders, P. Musella, E. Nesvold, L. Orsini, E. Palencia Cortezon, E. Perez, L. Perrozzi, A. Petrilli, A. Pfeiffer, M. Pierini, M. Pimiä, D. Piparo, M. Plagge, L. Quertenmont, A. Racz, W. Reece, J. Rojo, G. Rolandi[36], M. Rovere, H. Sakulin, F. Santanastasio, C. Schäfer, C. Schwick,

I. Segoni, S. Sekmen, A. Sharma, P. Siegrist, P. Silva, M. Simon, P. Sphicas[37], D. Spiga, M. Stoye, A. Tsirou, G.I. Veres[21], J.R. Vlimant, H.K. Wöhri, S.D. Worm[38], W.D. Zeuner

Paul Scherrer Institut, Villigen, Switzerland
W. Bertl, K. Deiters, W. Erdmann, K. Gabathuler, R. Horisberger, Q. Ingram, H.C. Kaestli, S. König, D. Kotlinski, U. Langenegger, D. Renker, T. Rohe

Institute for Particle Physics, ETH Zurich, Zurich, Switzerland
F. Bachmair, L. Bäni, L. Bianchini, P. Bortignon, M.A. Buchmann, B. Casal, N. Chanon, A. Deisher, G. Dissertori, M. Dittmar, M. Donegà, M. Dünser, P. Eller, K. Freudenreich, C. Grab, D. Hits, P. Lecomte, W. Lustermann, B. Mangano, A.C. Marini, P. Martinez Ruiz del Arbol, D. Meister, N. Mohr, F. Moortgat, C. Nägeli[39], P. Nef, F. Nessi-Tedaldi, F. Pandolfi, L. Pape, F. Pauss, M. Peruzzi, F.J. Ronga, M. Rossini, L. Sala, A.K. Sanchez, A. Starodumov[40], B. Stieger, M. Takahashi, L. Tauscher†, A. Thea, K. Theofilatos, D. Treille, C. Urscheler, R. Wallny, H.A. Weber

Universität Zürich, Zurich, Switzerland
C. Amsler[41], V. Chiochia, C. Favaro, M. Ivova Rikova, B. Kilminster, B. Millan Mejias, P. Robmann, H. Snoek, S. Taroni, M. Verzetti, Y. Yang

National Central University, Chung-Li, Taiwan
M. Cardaci, K.H. Chen, C. Ferro, C.M. Kuo, S.W. Li, W. Lin, Y.J. Lu, R. Volpe, S.S. Yu

National Taiwan University (NTU), Taipei, Taiwan
P. Bartalini, P. Chang, Y.H. Chang, Y.W. Chang, Y. Chao, K.F. Chen, C. Dietz, U. Grundler, W.-S. Hou, Y. Hsiung, K.Y. Kao, Y.J. Lei, R.-S. Lu, D. Majumder, E. Petrakou, X. Shi, J.G. Shiu, Y.M. Tzeng, M. Wang

Chulalongkorn University, Bangkok, Thailand
B. Asavapibhop, N. Suwonjandee

Cukurova University, Adana, Turkey
A. Adiguzel, M.N. Bakirci[42], S. Cerci[43], C. Dozen, I. Dumanoglu, E. Eskut, S. Girgis, G. Gokbulut, E. Gurpinar, I. Hos, E.E. Kangal, A. Kayis Topaksu, G. Onengut[44], K. Ozdemir, S. Ozturk[42], A. Polatoz, K. Sogut[45], D. Sunar Cerci[43], B. Tali[43], H. Topakli[42], M. Vergili

Middle East Technical University, Physics Department, Ankara, Turkey
I.V. Akin, T. Aliev, B. Bilin, S. Bilmis, M. Deniz, H. Gamsizkan, A.M. Guler, G. Karapinar[46], K. Ocalan, A. Ozpineci, M. Serin, R. Sever, U.E. Surat, M. Yalvac, M. Zeyrek

Bogazici University, Istanbul, Turkey
E. Gülmez, B. Isildak[47], M. Kaya[48], O. Kaya[48], S. Ozkorucuklu[49], N. Sonmez[50]

Istanbul Technical University, Istanbul, Turkey
H. Bahtiyar[51], E. Barlas, K. Cankocak, Y.O. Günaydin[52], F.I. Vardarlı, M. Yücel

National Scientific Center, Kharkov Institute of Physics and Technology, Kharkov, Ukraine
L. Levchuk, P. Sorokin

University of Bristol, Bristol, United Kingdom
J.J. Brooke, E. Clement, D. Cussans, H. Flacher, R. Frazier, J. Goldstein, M. Grimes, G.P. Heath, H.F. Heath, L. Kreczko, C. Lucas, Z. Meng, S. Metson, D.M. Newbold[38], K. Nirunpong, S. Paramesvaran, A. Poll, S. Senkin, V.J. Smith, T. Williams

Rutherford Appleton Laboratory, Didcot, United Kingdom
K.W. Bell, A. Belyaev[53], C. Brew, R.M. Brown, D.J.A. Cockerill, J.A. Coughlan, K. Harder,

S. Harper, J. Ilic, E. Olaiya, D. Petyt, B.C. Radburn-Smith, C.H. Shepherd-Themistocleous, I.R. Tomalin, W.J. Womersley

Imperial College, London, United Kingdom
R. Bainbridge, O. Buchmuller, D. Burton, D. Colling, N. Cripps, M. Cutajar, P. Dauncey, G. Davies, M. Della Negra, W. Ferguson, J. Fulcher, D. Futyan, A. Gilbert, A. Guneratne Bryer, G. Hall, Z. Hatherell, J. Hays, G. Iles, M. Jarvis, G. Karapostoli, M. Kenzie, R. Lane, R. Lucas[38], L. Lyons, A.-M. Magnan, J. Marrouche, B. Mathias, R. Nandi, J. Nash, A. Nikitenko[40], J. Pela, M. Pesaresi, K. Petridis, M. Pioppi[54], D.M. Raymond, S. Rogerson, A. Rose, C. Seez, P. Sharp†, A. Sparrow, A. Tapper, M. Vazquez Acosta, T. Virdee, S. Wakefield, N. Wardle

Brunel University, Uxbridge, United Kingdom
M. Chadwick, J.E. Cole, P.R. Hobson, A. Khan, P. Kyberd, D. Leggat, D. Leslie, W. Martin, I.D. Reid, P. Symonds, L. Teodorescu, M. Turner

Baylor University, Waco, USA
J. Dittmann, K. Hatakeyama, A. Kasmi, H. Liu, T. Scarborough

The University of Alabama, Tuscaloosa, USA
O. Charaf, S.I. Cooper, C. Henderson, P. Rumerio

Boston University, Boston, USA
A. Avetisyan, T. Bose, C. Fantasia, A. Heister, P. Lawson, D. Lazic, J. Rohlf, D. Sperka, J. St. John, L. Sulak

Brown University, Providence, USA
J. Alimena, S. Bhattacharya, G. Christopher, D. Cutts, Z. Demiragli, A. Ferapontov, A. Garabedian, U. Heintz, S. Jabeen, G. Kukartsev, E. Laird, G. Landsberg, M. Luk, M. Narain, M. Segala, T. Sinthuprasith, T. Speer

University of California, Davis, Davis, USA
R. Breedon, G. Breto, M. Calderon De La Barca Sanchez, S. Chauhan, M. Chertok, J. Conway, R. Conway, P.T. Cox, R. Erbacher, M. Gardner, R. Houtz, W. Ko, A. Kopecky, R. Lander, T. Miceli, D. Pellett, J. Pilot, F. Ricci-Tam, B. Rutherford, M. Searle, J. Smith, M. Squires, M. Tripathi, S. Wilbur, R. Yohay

University of California, Los Angeles, USA
V. Andreev, D. Cline, R. Cousins, S. Erhan, P. Everaerts, C. Farrell, M. Felcini, J. Hauser, M. Ignatenko, C. Jarvis, G. Rakness, P. Schlein†, E. Takasugi, P. Traczyk, V. Valuev, M. Weber

University of California, Riverside, Riverside, USA
J. Babb, R. Clare, J. Ellison, J.W. Gary, G. Hanson, J. Heilman, P. Jandir, H. Liu, O.R. Long, A. Luthra, M. Malberti, H. Nguyen, A. Shrinivas, J. Sturdy, S. Sumowidagdo, R. Wilken, S. Wimpenny

University of California, San Diego, La Jolla, USA
W. Andrews, J.G. Branson, G.B. Cerati, S. Cittolin, D. Evans, A. Holzner, R. Kelley, M. Lebourgeois, J. Letts, I. Macneill, S. Padhi, C. Palmer, G. Petrucciani, M. Pieri, M. Sani, V. Sharma, S. Simon, E. Sudano, M. Tadel, Y. Tu, A. Vartak, S. Wasserbaech[55], F. Würthwein, A. Yagil, J. Yoo

University of California, Santa Barbara, Santa Barbara, USA
D. Barge, C. Campagnari, T. Danielson, K. Flowers, P. Geffert, C. George, F. Golf, J. Incandela, C. Justus, D. Kovalskyi, V. Krutelyov, S. Lowette, R. Magaña Villalba, N. Mccoll, V. Pavlunin, J. Richman, R. Rossin, D. Stuart, W. To, C. West

California Institute of Technology, Pasadena, USA
A. Apresyan, A. Bornheim, J. Bunn, Y. Chen, E. Di Marco, J. Duarte, D. Kcira, Y. Ma, A. Mott, H.B. Newman, C. Pena, C. Rogan, M. Spiropulu, V. Timciuc, J. Veverka, R. Wilkinson, S. Xie, R.Y. Zhu

Carnegie Mellon University, Pittsburgh, USA
V. Azzolini, A. Calamba, R. Carroll, T. Ferguson, Y. Iiyama, D.W. Jang, Y.F. Liu, M. Paulini, J. Russ, H. Vogel, I. Vorobiev

University of Colorado at Boulder, Boulder, USA
J.P. Cumalat, B.R. Drell, W.T. Ford, A. Gaz, E. Luiggi Lopez, U. Nauenberg, J.G. Smith, K. Stenson, K.A. Ulmer, S.R. Wagner

Cornell University, Ithaca, USA
J. Alexander, A. Chatterjee, N. Eggert, L.K. Gibbons, W. Hopkins, A. Khukhunaishvili, B. Kreis, N. Mirman, G. Nicolas Kaufman, J.R. Patterson, A. Ryd, E. Salvati, W. Sun, W.D. Teo, J. Thom, J. Thompson, J. Tucker, Y. Weng, L. Winstrom, P. Wittich

Fairfield University, Fairfield, USA
D. Winn

Fermi National Accelerator Laboratory, Batavia, USA
S. Abdullin, M. Albrow, J. Anderson, G. Apollinari, L.A.T. Bauerdick, A. Beretvas, J. Berryhill, P.C. Bhat, K. Burkett, J.N. Butler, V. Chetluru, H.W.K. Cheung, F. Chlebana, S. Cihangir, V.D. Elvira, I. Fisk, J. Freeman, Y. Gao, E. Gottschalk, L. Gray, D. Green, O. Gutsche, D. Hare, R.M. Harris, J. Hirschauer, B. Hooberman, S. Jindariani, M. Johnson, U. Joshi, K. Kaadze, B. Klima, S. Kunori, S. Kwan, J. Linacre, D. Lincoln, R. Lipton, J. Lykken, K. Maeshima, J.M. Marraffino, V.I. Martinez Outschoorn, S. Maruyama, D. Mason, P. McBride, K. Mishra, S. Mrenna, Y. Musienko[56], C. Newman-Holmes, V. O'Dell, O. Prokofyev, N. Ratnikova, E. Sexton-Kennedy, S. Sharma, W.J. Spalding, L. Spiegel, L. Taylor, S. Tkaczyk, N.V. Tran, L. Uplegger, E.W. Vaandering, R. Vidal, J. Whitmore, W. Wu, F. Yang, J.C. Yun

University of Florida, Gainesville, USA
D. Acosta, P. Avery, D. Bourilkov, M. Chen, T. Cheng, S. Das, M. De Gruttola, G.P. Di Giovanni, D. Dobur, A. Drozdetskiy, R.D. Field, M. Fisher, Y. Fu, I.K. Furic, J. Hugon, B. Kim, J. Konigsberg, A. Korytov, A. Kropivnitskaya, T. Kypreos, J.F. Low, K. Matchev, P. Milenovic[57], G. Mitselmakher, L. Muniz, R. Remington, A. Rinkevicius, N. Skhirtladze, M. Snowball, J. Yelton, M. Zakaria

Florida International University, Miami, USA
V. Gaultney, S. Hewamanage, S. Linn, P. Markowitz, G. Martinez, J.L. Rodriguez

Florida State University, Tallahassee, USA
T. Adams, A. Askew, J. Bochenek, J. Chen, B. Diamond, J. Haas, S. Hagopian, V. Hagopian, K.F. Johnson, H. Prosper, V. Veeraraghavan, M. Weinberg

Florida Institute of Technology, Melbourne, USA
M.M. Baarmand, B. Dorney, M. Hohlmann, H. Kalakhety, F. Yumiceva

University of Illinois at Chicago (UIC), Chicago, USA
M.R. Adams, L. Apanasevich, V.E. Bazterra, R.R. Betts, I. Bucinskaite, J. Callner, R. Cavanaugh, O. Evdokimov, L. Gauthier, C.E. Gerber, D.J. Hofman, S. Khalatyan, P. Kurt, F. Lacroix, D.H. Moon, C. O'Brien, C. Silkworth, D. Strom, P. Turner, N. Varelas

The University of Iowa, Iowa City, USA
U. Akgun, E.A. Albayrak[51], B. Bilki[58], W. Clarida, K. Dilsiz, F. Duru, S. Griffiths, J.-P. Merlo, H. Mermerkaya[59], A. Mestvirishvili, A. Moeller, J. Nachtman, C.R. Newsom, H. Ogul, Y. Onel, F. Ozok[51], S. Sen, P. Tan, E. Tiras, J. Wetzel, T. Yetkin[60], K. Yi

Johns Hopkins University, Baltimore, USA
B.A. Barnett, B. Blumenfeld, S. Bolognesi, G. Giurgiu, A.V. Gritsan, G. Hu, P. Maksimovic, C. Martin, M. Swartz, A. Whitbeck

The University of Kansas, Lawrence, USA
P. Baringer, A. Bean, G. Benelli, R.P. Kenny III, M. Murray, D. Noonan, S. Sanders, R. Stringer, J.S. Wood

Kansas State University, Manhattan, USA
A.F. Barfuss, I. Chakaberia, A. Ivanov, S. Khalil, M. Makouski, Y. Maravin, L.K. Saini, S. Shrestha, I. Svintradze

Lawrence Livermore National Laboratory, Livermore, USA
J. Gronberg, D. Lange, F. Rebassoo, D. Wright

University of Maryland, College Park, USA
A. Baden, B. Calvert, S.C. Eno, J.A. Gomez, N.J. Hadley, R.G. Kellogg, T. Kolberg, Y. Lu, M. Marionneau, A.C. Mignerey, K. Pedro, A. Peterman, A. Skuja, J. Temple, M.B. Tonjes, S.C. Tonwar

Massachusetts Institute of Technology, Cambridge, USA
A. Apyan, G. Bauer, W. Busza, I.A. Cali, M. Chan, L. Di Matteo, V. Dutta, G. Gomez Ceballos, M. Goncharov, D. Gulhan, Y. Kim, M. Klute, Y.S. Lai, A. Levin, P.D. Luckey, T. Ma, S. Nahn, C. Paus, D. Ralph, C. Roland, G. Roland, G.S.F. Stephans, F. Stöckli, K. Sumorok, D. Velicanu, R. Wolf, B. Wyslouch, M. Yang, Y. Yilmaz, A.S. Yoon, M. Zanetti, V. Zhukova

University of Minnesota, Minneapolis, USA
B. Dahmes, A. De Benedetti, G. Franzoni, A. Gude, J. Haupt, S.C. Kao, K. Klapoetke, Y. Kubota, J. Mans, N. Pastika, R. Rusack, M. Sasseville, A. Singovsky, N. Tambe, J. Turkewitz

University of Mississippi, Oxford, USA
J.G. Acosta, L.M. Cremaldi, R. Kroeger, S. Oliveros, L. Perera, R. Rahmat, D.A. Sanders, D. Summers

University of Nebraska-Lincoln, Lincoln, USA
E. Avdeeva, K. Bloom, S. Bose, D.R. Claes, A. Dominguez, M. Eads, R. Gonzalez Suarez, J. Keller, I. Kravchenko, J. Lazo-Flores, S. Malik, F. Meier, G.R. Snow

State University of New York at Buffalo, Buffalo, USA
J. Dolen, A. Godshalk, I. Iashvili, S. Jain, A. Kharchilava, A. Kumar, S. Rappoccio, Z. Wan

Northeastern University, Boston, USA
G. Alverson, E. Barberis, D. Baumgartel, M. Chasco, J. Haley, A. Massironi, D. Nash, T. Orimoto, D. Trocino, D. Wood, J. Zhang

Northwestern University, Evanston, USA
A. Anastassov, K.A. Hahn, A. Kubik, L. Lusito, N. Mucia, N. Odell, B. Pollack, A. Pozdnyakov, M. Schmitt, S. Stoynev, K. Sung, M. Velasco, S. Won

University of Notre Dame, Notre Dame, USA
D. Berry, A. Brinkerhoff, K.M. Chan, M. Hildreth, C. Jessop, D.J. Karmgard, J. Kolb, K. Lannon,

W. Luo, S. Lynch, N. Marinelli, D.M. Morse, T. Pearson, M. Planer, R. Ruchti, J. Slaunwhite, N. Valls, M. Wayne, M. Wolf

The Ohio State University, Columbus, USA
L. Antonelli, B. Bylsma, L.S. Durkin, C. Hill, R. Hughes, K. Kotov, T.Y. Ling, D. Puigh, M. Rodenburg, G. Smith, C. Vuosalo, B.L. Winer, H. Wolfe

Princeton University, Princeton, USA
E. Berry, P. Elmer, V. Halyo, P. Hebda, J. Hegeman, A. Hunt, P. Jindal, S.A. Koay, P. Lujan, D. Marlow, T. Medvedeva, M. Mooney, J. Olsen, P. Piroué, X. Quan, A. Raval, H. Saka, D. Stickland, C. Tully, J.S. Werner, S.C. Zenz, A. Zuranski

University of Puerto Rico, Mayaguez, USA
E. Brownson, A. Lopez, H. Mendez, J.E. Ramirez Vargas

Purdue University, West Lafayette, USA
E. Alagoz, D. Benedetti, G. Bolla, D. Bortoletto, M. De Mattia, A. Everett, Z. Hu, M. Jones, K. Jung, O. Koybasi, M. Kress, N. Leonardo, D. Lopes Pegna, V. Maroussov, P. Merkel, D.H. Miller, N. Neumeister, I. Shipsey, D. Silvers, A. Svyatkovskiy, F. Wang, W. Xie, L. Xu, H.D. Yoo, J. Zablocki, Y. Zheng

Purdue University Calumet, Hammond, USA
N. Parashar

Rice University, Houston, USA
A. Adair, B. Akgun, K.M. Ecklund, F.J.M. Geurts, W. Li, B. Michlin, B.P. Padley, R. Redjimi, J. Roberts, J. Zabel

University of Rochester, Rochester, USA
B. Betchart, A. Bodek, R. Covarelli, P. de Barbaro, R. Demina, Y. Eshaq, T. Ferbel, A. Garcia-Bellido, P. Goldenzweig, J. Han, A. Harel, D.C. Miner, G. Petrillo, D. Vishnevskiy, M. Zielinski

The Rockefeller University, New York, USA
A. Bhatti, R. Ciesielski, L. Demortier, K. Goulianos, G. Lungu, S. Malik, C. Mesropian

Rutgers, The State University of New Jersey, Piscataway, USA
S. Arora, A. Barker, J.P. Chou, C. Contreras-Campana, E. Contreras-Campana, D. Duggan, D. Ferencek, Y. Gershtein, R. Gray, E. Halkiadakis, D. Hidas, A. Lath, S. Panwalkar, M. Park, R. Patel, V. Rekovic, J. Robles, S. Salur, S. Schnetzer, C. Seitz, S. Somalwar, R. Stone, S. Thomas, P. Thomassen, M. Walker

University of Tennessee, Knoxville, USA
G. Cerizza, M. Hollingsworth, K. Rose, S. Spanier, Z.C. Yang, A. York

Texas A&M University, College Station, USA
O. Bouhali[61], R. Eusebi, W. Flanagan, J. Gilmore, T. Kamon[62], V. Khotilovich, R. Montalvo, I. Osipenkov, Y. Pakhotin, A. Perloff, J. Roe, A. Safonov, T. Sakuma, I. Suarez, A. Tatarinov, D. Toback

Texas Tech University, Lubbock, USA
N. Akchurin, C. Cowden, J. Damgov, C. Dragoiu, P.R. Dudero, K. Kovitanggoon, S.W. Lee, T. Libeiro, I. Volobouev

Vanderbilt University, Nashville, USA
E. Appelt, A.G. Delannoy, S. Greene, A. Gurrola, W. Johns, C. Maguire, Y. Mao, A. Melo, M. Sharma, P. Sheldon, B. Snook, S. Tuo, J. Velkovska

University of Virginia, Charlottesville, USA
M.W. Arenton, S. Boutle, B. Cox, B. Francis, J. Goodell, R. Hirosky, A. Ledovskoy, C. Lin, C. Neu, J. Wood

Wayne State University, Detroit, USA
S. Gollapinni, R. Harr, P.E. Karchin, C. Kottachchi Kankanamge Don, P. Lamichhane, A. Sakharov

University of Wisconsin, Madison, USA
D.A. Belknap, L. Borrello, D. Carlsmith, M. Cepeda, S. Dasu, S. Duric, E. Friis, M. Grothe, R. Hall-Wilton, M. Herndon, A. Hervé, P. Klabbers, J. Klukas, A. Lanaro, R. Loveless, A. Mohapatra, M.U. Mozer, I. Ojalvo, T. Perry, G.A. Pierro, G. Polese, I. Ross, T. Sarangi, A. Savin, W.H. Smith, J. Swanson

†: Deceased
1: Also at Vienna University of Technology, Vienna, Austria
2: Also at CERN, European Organization for Nuclear Research, Geneva, Switzerland
3: Also at Institut Pluridisciplinaire Hubert Curien, Université de Strasbourg, Université de Haute Alsace Mulhouse, CNRS/IN2P3, Strasbourg, France
4: Also at National Institute of Chemical Physics and Biophysics, Tallinn, Estonia
5: Also at Skobeltsyn Institute of Nuclear Physics, Lomonosov Moscow State University, Moscow, Russia
6: Also at Universidade Estadual de Campinas, Campinas, Brazil
7: Also at California Institute of Technology, Pasadena, USA
8: Also at Laboratoire Leprince-Ringuet, Ecole Polytechnique, IN2P3-CNRS, Palaiseau, France
9: Also at Zewail City of Science and Technology, Zewail, Egypt
10: Also at Suez Canal University, Suez, Egypt
11: Also at Cairo University, Cairo, Egypt
12: Also at Fayoum University, El-Fayoum, Egypt
13: Also at British University in Egypt, Cairo, Egypt
14: Now at Ain Shams University, Cairo, Egypt
15: Also at National Centre for Nuclear Research, Swierk, Poland
16: Also at Université de Haute Alsace, Mulhouse, France
17: Also at Joint Institute for Nuclear Research, Dubna, Russia
18: Also at Brandenburg University of Technology, Cottbus, Germany
19: Also at The University of Kansas, Lawrence, USA
20: Also at Institute of Nuclear Research ATOMKI, Debrecen, Hungary
21: Also at Eötvös Loránd University, Budapest, Hungary
22: Also at Tata Institute of Fundamental Research - EHEP, Mumbai, India
23: Also at Tata Institute of Fundamental Research - HECR, Mumbai, India
24: Now at King Abdulaziz University, Jeddah, Saudi Arabia
25: Also at University of Visva-Bharati, Santiniketan, India
26: Also at University of Ruhuna, Matara, Sri Lanka
27: Also at Isfahan University of Technology, Isfahan, Iran
28: Also at Sharif University of Technology, Tehran, Iran
29: Also at Plasma Physics Research Center, Science and Research Branch, Islamic Azad University, Tehran, Iran
30: Also at Laboratori Nazionali di Legnaro dell'INFN, Legnaro, Italy
31: Also at Università degli Studi di Siena, Siena, Italy
32: Also at Purdue University, West Lafayette, USA
33: Also at Universidad Michoacana de San Nicolas de Hidalgo, Morelia, Mexico

34: Also at Faculty of Physics, University of Belgrade, Belgrade, Serbia
35: Also at Facoltà Ingegneria, Università di Roma, Roma, Italy
36: Also at Scuola Normale e Sezione dell'INFN, Pisa, Italy
37: Also at University of Athens, Athens, Greece
38: Also at Rutherford Appleton Laboratory, Didcot, United Kingdom
39: Also at Paul Scherrer Institut, Villigen, Switzerland
40: Also at Institute for Theoretical and Experimental Physics, Moscow, Russia
41: Also at Albert Einstein Center for Fundamental Physics, Bern, Switzerland
42: Also at Gaziosmanpasa University, Tokat, Turkey
43: Also at Adiyaman University, Adiyaman, Turkey
44: Also at Cag University, Mersin, Turkey
45: Also at Mersin University, Mersin, Turkey
46: Also at Izmir Institute of Technology, Izmir, Turkey
47: Also at Ozyegin University, Istanbul, Turkey
48: Also at Kafkas University, Kars, Turkey
49: Also at Suleyman Demirel University, Isparta, Turkey
50: Also at Ege University, Izmir, Turkey
51: Also at Mimar Sinan University, Istanbul, Istanbul, Turkey
52: Also at Kahramanmaras Sütcü Imam University, Kahramanmaras, Turkey
53: Also at School of Physics and Astronomy, University of Southampton, Southampton, United Kingdom
54: Also at INFN Sezione di Perugia; Università di Perugia, Perugia, Italy
55: Also at Utah Valley University, Orem, USA
56: Also at Institute for Nuclear Research, Moscow, Russia
57: Also at University of Belgrade, Faculty of Physics and Vinca Institute of Nuclear Sciences, Belgrade, Serbia
58: Also at Argonne National Laboratory, Argonne, USA
59: Also at Erzincan University, Erzincan, Turkey
60: Also at Yildiz Technical University, Istanbul, Turkey
61: Also at Texas A&M University at Qatar, Doha, Qatar
62: Also at Kyungpook National University, Daegu, Korea